Title
Large-eddy simulation of complex terrain effects on atmospheric boundary-layer turbulence and stable flow phenomena

Author
Connolly, Alexander Daniel

Publication Date
2020

Peer reviewed|Thesis/dissertation

Large-eddy simulation of complex terrain effects on atmospheric boundary-layer turbulence and stable flow phenomena

by

Alexander Daniel Connolly

A dissertation submitted in partial satisfaction of the

requirements for the degree of

Doctor of Philosophy

in

Engineering- Civil & Environmental Engineering

in the

Graduate Division

of the

University of California, Berkeley

Committee in charge:

Professor Fotini Katopodes Chow, Chair
Professor Mark Stacey
Professor David Romps

Fall 2020

Large-eddy simulation of complex terrain effects on atmospheric boundary-layer turbulence and stable flow phenomena

Abstract

Large-eddy simulation of complex terrain effects on atmospheric boundary-layer turbulence and stable flow phenomena

by

Alexander Daniel Connolly

Doctor of Philosophy in Engineering- Civil & Environmental Engineering

University of California, Berkeley

Professor Fotini Katopodes Chow, Chair

Traditional weather models struggle to resolve the details of complex terrain and the strongly stable stratification often observed in near surface temperature inversions. Conversely, traditional engineering computational fluid dynamics codes often use high resolution grid meshes, but do not include forcing from synoptic scale weather. As computational power grows, a new class of models is emerging. These are nested large-eddy simulations (LES), which are both highly resolved and include large scale weather forcing. In this case, high resolution implies grid meshes that are fine enough to resolve the most energetic eddies in the atmospheric boundary layer. These high resolution domains are nested, i.e. forced at the lateral boundaries, by coarser mesoscale models. The role of nested large-eddy simulation in the study of atmospheric boundary layer is twofold. First, trusted LES data allow the study of important dynamics with all the relevant forcing of real flow, but without dense observation networks. Though observations are still critical to the validation of these models, in some cases, as in fire weather, sufficiently detailed observations are very difficult to carry out due to practical concerns. In other cases, simulation is simply a less expensive means to achieve higher resolution data than even the densest sensor network can provide. In this sense, LES is a valuable tool for the research community. For the forecasting community, however, LES cannot be used in place of coarser models given current computational power. As prediction is an ultimate goal of weather modeling, we turn to the second role of LES, the generation of subgrid parameterizations for use in coarse models that can be run for real-time forecasting. The dual purpose of LES, the direct study of atmospheric boundary layer dynamics and the development of parameterizations for mesoscale models, motivate three investigations into the dynamics of the atmospheric boundary layer presented here. Each study conducts LES with the Weather Research and Forecasting (WRF) model, an advanced numerical weather prediction (NWP) code. Unlike traditional NWP or engineering codes, these simulations include both complex terrain as well as realistic weather forcing to advance our understanding of atmospheric boundary layer dynamics and the LES technique itself.

The first project is conducted as part of the Mountain Terrain Atmospheric Modeling and Observations (MATERHORN) program. During the field campaign of the MATERHORN, large temperature fluctuations were observed on the slope of Granite Peak, Utah, which partially encloses a cold-air pool in the east basin. These flow features are able to be resolved using LES within the WRF model with $\Delta x = 100$ m, allowing accurate representation of lee vortices with horizontal length scale of $\mathcal{O}(1$ km). At this resolution, terrain slopes become quite steep, and some model warm biases remain in the east basin due to limits on terrain-following coordinates that prevent the model from fully resolving drainage flows with this steep terrain. A new timestep limit for the WRF model related to these steep slopes is proposed. In addition, the initialization of soil moisture is adjusted by drying the shallowest layer to assist the formation of a cold pool in the LES. These real case simulations compare well to observations and also to previously published simulations using idealized configurations to study similar phenomena. For instance, the values of non-dimensional mountain height, which characterize flow regimes in idealized studies, are similar in the real case. With their predictive capabilities established, these non-dimensional numbers are likely to provide the future basis for parameterization of the lee vortices which cannot be resolved by NWP models.

The second study addresses a challenge to simulating turbulent flow in multiscale atmospheric applications, the efficient generation of resolved turbulence motions over an area of interest. One approach is to apply small perturbations to flow variables near the inflow planes of turbulence-resolving simulation domains nested within larger mesoscale domains. While this approach has been examined in numerous idealized and simple terrain cases, its efficacy in complex terrain environments has not yet been fully explored. Here, we examine the benefits of the stochastic cell perturbation method (CPM) over real complex terrain using data from the 2017 Perdigão field campaign, conducted in an approximately 2-km wide valley situated between two nearly parallel ridges. Following a typical configuration for multiscale simulation using nested domains within the WRF model to downscale from a mesoscale to an LES, we apply the CPM on a domain with a relatively coarse LES mesh spacing of 150 m. LES at this resolution often generates spurious coherent structures under unstable atmospheric conditions with moderate mean wind speeds. We examine the impacts of the CPM on the representation of turbulence within the nested LES domain under moderate mean flow conditions in three different stability regimes: weakly convective, strongly convective, and weakly stable. In addition, two different resolutions of the underlying terrain are used to explore the role of the complex topography itself in generating turbulent structures. We demonstrate that the CPM improves the representation of turbulence within the LES domains, relative to the use of high-resolution complex terrain alone. During the convective conditions, the CPM improves the rate at which smaller-scales of turbulence form, while also accelerating the attenuation of the spurious numerically-generated roll structures near the inflow boundary. During stable conditions, the coarse mesh spacing of the LES used herein was insufficient to maintain resolved turbulence using CPM as the flow develops downstream, highlighting the need for yet higher resolution under even weakly stable conditions. The CPM was particularly efficient during the evening transition period.

A final study investigates fundamental controls on drainage flow dynamics. Historically called katabatic flow, drainage flow is buoyancy driven and directed downslope in response to surface cooling typical of the nocturnal period. Analogous upslope flow due to surface heating during the day is often called anabatic flow. A fundamental question is at what time during the evening transition does the slope wind system switch from anabatic to drainage flow. A natural benchmark for this transition is sunset, but the presence of terrain results in shadows cast onto east-facing slopes which can complicate this analysis. To guide this analysis, functional forms for the time of the shadow front propagation are presented for an idealized terrain shape used for an LES in WRF. Even with idealized topography, the present LES are significantly more advanced than previous models used to investigate idealized drainage flow, which prescribed surface cooling rather than prognosticating the cooling in response to the diurnal cycle of insolation and the characteristics of the surface and soil types, as done here. This complexity allows for potentially counterintuitive results, such as the onset of drainage flow occurring on the shadow-cast eastern slopes later than on the sunnier western slopes due to convective structures which persist after sunset. Despite these complications during the development of drainage flow in the evening, there are periods during the night when analytical solutions compare well to the LES solution of drainage flow profiles. A novel analytical solution also explains a dependence on the angle of the slope found in observation data but missing in the original (Prandtl 1942) solution by replacing the traditional Dirichlet with a Neumann boundary condition. The favorable comparison between analytical solutions and results from the high resolution numerical model are a first step towards the ultimate parameterization of drainage flow in coarser NWP models.

To my father

Contents

List of Figures

List of Tables

Acknowledgments

I am grateful to my mentor, Tina Katopodes Chow, for all the guidance and for being an inspiring teacher, adviser, and human being.

To the members of the Environmental Fluid Mechanics & Hydrology research group, I am grateful for the friendship and scholarship we shared.

This work would not have been possible without the support of my wife, Valerie Connolly, who excels at making diagrams of sunlit mountains and copy editing.

The MATERHORN Program was funded by the Office of Naval Research MURI Award N00014-11-1-0709 (Program Officers: Drs. Ronald Ferek and Daniel Eleuterio), with additional funding from the Army Research Office (Program Officers: Gordon Videen and Walter Bach), Air Force Weather Agency, Research Offices of University of Notre Dame and University of Utah, and Wayne and Diana Murdy Family Endowment at Notre Dame. We thank the MATERHORN field team and Dugway Proving Ground staff. Simulations were performed on the UC Berkeley Savio computing cluster.

The work conducted as part of The Perdigão was supported from National Science Foundation Grant AGS-1565483. The Perdigão project was primarily funded by the U.S. National Science Foundation, European Commission's ERANET+, Danish Energy Agency, German Federal Ministry of Economy and Energy, Portugal Foundation for Science and Technology, U.S. Army Research Laboratory, and the Israel Binational Science Foundation. Perdigão would not have been possible without the alliance of many personnel and entities, which are listed in the supplemental material of Fernando et al. (2019). We would like to acknowledge high-performance computing support from Cheyenne (doi:10.5065/D6RX99HX) provided by NCAR's Computational and Information Systems Laboratory, sponsored by the National Science Foundation.

This research used the Savio computational cluster resource provided by the Berkeley Research Computing program at the University of California, Berkeley (supported by the UC Berkeley Chancellor, Vice Chancellor for Research, and Chief Information Officer)

Chapter 1

Introduction

1.1 Motivation

Accurate and detailed simulations of the atmospheric boundary layer are motivated by many problems affecting human lives. For example, poor air quality is exacerbated by cold-air pools that can fill topographic depressions in the surface of the earth. These cold-air pools are associated with strengthened stable stratification that traps pollutants emitted by human activity within basins such as the Salt Lake Valley in Utah (Lareau et al. 2013). Another example that illustrates the need for detailed atmospheric boundary-layer simulation is the effect of complex terrain on fire weather. Fire spreads more rapidly over slopes than on flat terrain, so inclusion of the details of the surface boundary in fire weather forecasting is paramount to the safety of firefighters (Holden and Jolly 2011). To better address these problems which affect humans, and all other denizens of the atmospheric boundary layer, this dissertation seeks to improve the understanding of the boundary-layer through the use of advanced simulation.

The technique of large-eddy simulation (LES) is increasingly used to study these problems involving the influence of topography and stratification on atmospheric boundary layer processes (Wood 2000; Chow et al. 2013; Fernando et al. 2015, 2019). Traditionally, numerical weather prediction (NWP) models resolve neither the details of complex terrain nor the three-dimensional turbulence that characterize the atmospheric boundary layer. Instead, subgrid parameterizations have been employed. Planetary boundary-layer (PBL) schemes, the turbulence closures employed in NWP models, and orographic drag schemes, parameterizations for unresolved complex terrain, both exemplify these subgrid parameterizations. Limits of computing power have so far constrained weather models to the coarse grid meshes in the mesoscale, $\mathcal{O}$(1–10 km), which necessitate the use of such schemes. More recently, LES is able to avoid the use of PBL schemes by using grid resolutions fine enough to resolve the most energetic eddies (Lilly 1962; Deardorff 1980). Finer meshes also allow atmospheric models to better represent the underlying topography and the local stratification of the atmosphere. As the power of computation grows, and the popularity of LES along with it, so too do opportunities to study the interaction of boundary-layer turbulence and processes with stratification and highly complex terrain.

The effects of topography are enhanced under stable stratification, further complicating modeling efforts (Baines 1998). Convective systems can also be affected by the presence of terrain (De Wekker and Kossmann 2015), but effects of topography are enhanced under stable stratification due to the decoupling of synoptic flows and low-level flows within a near-surface inversion (Garratt 1994). Such an inversion inhibits vertical mixing of momentum from aloft. Also important are flow blocking and channeling when air parcels are too dense to rise up and over obstacles (Leo et al. 2016), the draining of near-surface air parcels into basin cold-air pools (Zardi and Whiteman 2013; Burns and Chemel 2014), and the spurring of internal gravity waves (Scorer 1949; Schär and Smith 1993; Zhong and Chow 2013). Likely due to this multiplicity of phenomena requiring parameterization, stable conditions also pose special challenges to mesoscale NWP models. Such models are more successful during daytime when convection is the sole dominant process for vertical mixing within the

boundary layer (Xie et al. 2012). Typical night-time conditions, under stable stratification when convection does not play a role, are not as well reproduced with these PBL schemes (Holtslag et al. 2013).

The LES technique can help improve forecasting of the stable atmosphere, though not without addressing its own stability related challenges. As stability increases, turbulent fluctuations are diminished and finer meshes are required to resolve the largest turbulent motions (Pope 2000). For the stability often observed in the atmospheric boundary layer, it is prohibitively expensive to run forecasts with LES due to this grid spacing requirement. Despite the significant expense due to fine meshes, LES is still a valuable tool for improving current forecasting models; efforts at the microscale aid the development of improved parameterizations for the boundary layer over complex terrain in future mesoscale models.

1.2 Large-eddy simulation

The dynamical cores of NWP codes are based on discretized versions of the governing equations for relevant atmospheric variables: momentum, mass, energy, moisture, trace gases, and so on. In the case of mesoscale simulations using PBL schemes, discretizion is assumed equivalent to Reynolds averaging for the gridded quantities. In the case of microscale simulations using an LES turbulence closure, spatial filtering is applied by the grid. The formulation of the evolution equations is strikingly similar regardless of whether a Reynolds averaging or a grid filtering approach is considered. The overline notation, $\overline{\cdot}$, implies the filtering or Reynolds-averaging operation. Note, in this work the LES filter is treated as an implicit filter due to grid discretization, i.e. no explicit filter is applied. Taking filtered velocity, $\overline{u_i}$, as our variable of interest, we provide the spatially filtered momentum equation as

$$\frac{\partial \overline{u_i}}{\partial t} = -\overline{u_j}\frac{\partial \overline{u_i}}{\partial x_j} - \frac{1}{\overline{\rho}}\frac{\partial \overline{P}}{\partial x_i} - \frac{\partial \tau_{ij}}{\partial x_j} + \epsilon_{3ij} f \overline{u_j} + \cdots \tag{1.1}$$

In LES, the terms above, from left to right, are known as unsteadiness, resolved advection, resolved pressure forcing, subfilter stresses normalized by density, and Coriolis. For the Reynolds averaging approach, the variable of interest is mean velocity and the same terms are called unsteadiness, mean advection, mean pressure forcing, Reynolds stresses normalized by density, and Coriolis. The ellipses indicate that we could add more terms if other forces are present, e.g. electromagnetic forces in the ionosphere or stresses added by the blades of wind turbines (Marjanovic et al. 2017). Both Reynolds-averaged and LES equations specify the subgrid stress,

$$\tau_{ij} = \overline{u_i u_j} - \overline{u_i}\,\overline{u_j}. \tag{1.2}$$

For Reynolds-averaging, the velocities can be decomposed into mean and fluctuating parts, resulting in a familiar form for the Reynolds stress, $\tau_{ij} = \overline{u'_i u'_j}$, where turbulent fluctuations, deviations from the Reynolds-averaged quantity, are denoted as primed variables. For

the LES technique, no further mathematical manipulations are possible. Regardless, these terms introduce unknown unfiltered variables that lack additional equations, leading to the turbulence closure problem. When we express these unknown quantities in terms of known quanties, the system of equation is closed and can be approximately solved. To provide this closure, additional physics must be considered. At fine enough scales the effect of turbulence is similar to Fickian diffusion, so an analogy to molecular diffusion is often used

$$\tau_{ij} = -K_M \left(\frac{\partial \overline{u_i}}{\partial x_j} + \frac{\partial \overline{u_j}}{\partial x_i} \right). \tag{1.3}$$

To make clear the analogy, the term K_M is often called the eddy viscosity or turbulent viscosity; in this work we use eddy diffusivity for momentum, indicated by subscript M, and analogous coefficients in the internal energy equation are called thermal diffusivity, indicated by subscript H. In general, these diffusivities vary in space and there are numerous proposals for the specification of the eddy diffusivity. Here, we use the so-called TKE 1.5 closure (Moeng 1984). Key features of this model can be understood from a dimensional analysis that leads to the assumption that the diffusivity is the product of a length scale, l, and a velocity scale, $\sqrt{k}$, with constant of proportionality, $c_k = 0.15$,

$$K_M = c_k \, l \, \sqrt{k}. \tag{1.4}$$

Most simply, a scale-aware length scale can be obtained from the grid spacing itself,

$$l = \sqrt[3]{\Delta x \Delta y \Delta z}, \tag{1.5}$$

though corrections related to stratification are typically added for the case of strong atmospheric stability. A velocity scale can be obtained from the turbulent kinetic energy, k, which is prognosticated with its own equation,

$$\frac{\partial k}{\partial t} = -\overline{u_j} \frac{\partial k}{\partial x_j} + \delta_{ij} \frac{g_j}{\overline{\theta}_v} \overline{u_i' \theta_v'} - \overline{u_i' u_j'} \frac{\partial \overline{u_i}}{\partial x_j} - \frac{\partial \overline{u_j' k}}{\partial x_j} - \frac{1}{\bar{\rho}} \frac{\partial \overline{u_j' p'}}{\partial x_j} - \epsilon, \tag{1.6}$$

where the terms, from left to right, are known as unsteadiness, advection, buoyancy production/consumption, shear generation, turbulent transport, pressure correlation, and dissipation. Empirically fit closures for the latter terms can be found in Deardorff (1980) and subsequent form. Throughout the current work, the terms take the widely used forms due to Moeng (1984); Moeng et al. (2007) that are included in the NWP model described in the following section.

1.3 The Weather Research and Forecasting model

The Weather Research and Forecasting (WRF) model (Skamarock et al. 2008) is maintained by the National Center for Atmospheric Research (NCAR) with contributions provided by

an open-source community of users. The dynamic core of the model provides a numerical solution of the compressible flow equations with a third-order Runge–Kutta time advancement scheme, with split time stepping to handle acoustic modes, as well as fifth-order horizontal advection and third-order vertical advection. The grid used is an Arakawa C-staggered grid with uniform horizontal distance between grid points. The vertical coordinate is a nonuniform pressure-based, terrain-following coordinate system that generally allows for finer resolution nearer the surface boundary. These coordinates are defined as

$$\eta_i = \frac{P_{h,i} - P_{h,top}}{P_{h,surface} - P_{h,top}} \tag{1.7}$$

where P_h is the hydrostatic pressure at the i^{th} vertical level, top of the column, or the surface as denoted by the second subscript. Lateral boundary conditions are provided to nested simulations by one-way nesting within concurrently run mesoscale parent simulations, the coarsest of which is ultimately forced by analysis data, either from a global model, the Global Forecasting System, or from one of two regional models, the North American Mesoscale (NAM) model and the European Centre for Medium-range Forecasting (ECMWF) institution's High Resolution (HRES) model. Initial conditions for these simulations also come from these analysis data. Alternatively, the model can be set up in an idealized manner with periodic boundary conditions for stand-alone simulations.

Physical parameterizations employed in all simulations presented here include the Noah land-surface model (Chen and Dudhia 2001), the Rapid Radiative Transfer Model for longwave radiation (Mlawer et al. 1997), the Dudhia shortwave radiation model (Dudhia 1989). The radiation inputs are modulated by a topographic shading routine to account for the presence of neighboring terrain (Zängl 2005). Different simulations make use of different surface-layer parameterizations, but they are all based on Monin–Obukhov similarity theory (Monin and Obukhov 1954). Further details on the form of this class of surface-layer models is presented in the appendix. Parent mesoscale models make use of various PBL schemes. A turbulent kinetic energy (TKE) 1.5-order LES turbulence closure, discussed in the previous section, is used for the large-eddy simulations here (Deardorff 1980; Moeng 1984; Moeng et al. 2007). While there are perhaps more advanced dynamic cores available in engineering LES codes, none are coupled with as complete a physical suite as detailed above. Thus, the current models are some of the most advanced LES possible.

The WRF models benefit from a multiscale modeling framework that allows finer scale computational domains to be nested within coarser parent models. This allows micrometeorolgical simulations to be forced by realistic synoptic scale weather through dynamic downscaling. Parent mesoscale models, however, do not resolve three-dimensional turbulence to be passed onto their child simulations. Instead, the turbulence must develop on the nested LES domains. The distance from the nested boundary, called fetch, required for fine-scale turbulence to develop represents substantial computational expense (Mirocha et al. 2013, 2014). Before sufficient fetch is reached, the computed solution does not provide more detail than its parent domain, so it is in some sense wasted. Perturbations can be applied near the inflow boundary of the LES to reduce the region of poorly resolved turbulence.

With such a treatment, smaller LES domains can be used to develop the turbulent scales, reducing the overall computational cost of the simulations. One method for applying turbulence generating perturbations, the cell perturbation method (Muñoz-Esparza et al. 2014, 2017), is added to the WRF model used in certain multiscale simulations presented here.

1.4 Drainage flow modeling

A physical problem that relates, in different ways, to each chapter of the following work is modeling of drainage flow, a.k.a. katabatic flow. These flows are defined as buoyancy driven downslope flows. Steady state, analytical solutions to buoyancy driven, two-dimensional flow down an infinite, uniform slope (Prandtl 1942) are the simplest possible models of such flow. The direct descendants of this analytic work are approximate analytic solutions that account for eddy and thermal diffusivity coefficients varying in height (Grisogono and Oerlemans 2001). More commonly, through the use of computational fluid dynamic techniques, numerical solutions are obtained for an increasingly complicated model problem: considering fuller sets of equations (Defant 1949; Manins and Sawford 1979; Mahrt 1982; Horst and Doran 1986), adding three-dimensional effects such as slope and valley flow interactions (Egger 1990), and using more sophisticated turbulence closures (Axelsen and Dop 2009a,b; Grisogono and Axelsen 2012). Often the computations are performed by engineering LES codes, generally not coupled with any of the sophisticated physics parameterizations such as the surface layer and radiation schemes that were developed separately in the meteorology community. Until recently, numerical weather prediction codes could not hope to resolve drainage flows because of the coarse grid resolutions used. Now, with the aid of high-performance parallel computers, weather models are able to run at large-eddy permitting resolutions and the engineering field of complex terrain flows may at last benefit from these advanced physics schemes (Wood 2000; Chow et al. 2013). Now, semi-ideal simulations may use full meteorological physics while still enforcing ideal boundary conditions. Commonly, an idealized terrain shape is used (Smith and Skyllingstad 2005; Schmidli et al. 2011). Even when a real terrain shape is used, simplified initial, lateral boundary, and surface boundary conditions are used, as in the semi-ideal simulations by Arthur et al. (2018). A novel semi-ideal model is presented in this work, in which advanced surface flux boundary conditions are employed but an ideal terrain shape is used, after finding the real simulations presented here to not be not adept at resolving drainage flows.

1.5 Summary of chapters

Chapter 2 presents a case-study of stable flow phenomena, cold air pools and lee vortices, and serves as a cautionary tale regarding drainage flows. Simulations are performed for the site of the Mountain Terrain Atmospheric Modeling and Observations (MATERHORN) program (Fernando et al. 2015), an isolated desert mountain near a semi-open basin in the Dugway

proving Ground, Utah. Large fluctuations in temperature occurred on the mountain slopes during all observation periods of the program during the Fall. Simulations here show these fluctuations are due to the displacement of the cold-air pool in the basin by vortices that form in the lee of the mountain. Further, these real-weather LES show the non-dimensional mountain height parameter can determine the occurrence of baroclinically generated lee vortices just as in previous ideal studies of orographic wakes. Investigation of the basin cold air pool demonstrates the kind of errors that can arise from using a meteorological model that fails to resolve drainage flows. A simple heuristic is presented to argue that this inability is due to the use of a terrain-following coordinate system over 'very' steep slopes, some over 45 degrees. In lieu of novel techniques, great computational expense would be required to resolve both the fine scale drainage flow and the larger scale lee vortices.

The second study, Chapter 3, addresses the problem of computational expense for LES nested in mesoscale models. The work is conducted on behalf of the Perdigão field campaign (Fernando et al. 2019), which is primarily concerned with determining the fate of the wake of a wind turbine installed on a ridge of a valley, the Vale do Cabrão in Portugal, particularly under stable stratification. While drainage flow itself may be important in determining the transport of the turbine wake, the present work deals primarily with the preliminary concern of computational expense. Specifically, the present study considers the potential for reducing the extent of domains of nested LES, which include significant distance from the inflow boundary only to develop turbulent flow at scales that are not inherited from their parent mesoscale simulations. Here, a recent approach for synthetic turbulence generation, the cell perturbation method (CPM) (Muñoz-Esparza et al. 2017), is tested in a real weather case study for the first time over complex terrain. Especially for intermediate stability, as observed during the evening transition, the method accelerates the development of turbulence to mitigate computational expense. This result in part motivates the further investigation of the evening transition period presented in the following chapter. Additionally, the ability of the CPM to significantly mitigate the computational expense of nested LES is a promising development for micrometeorological modeling more generally.

Chapter 4 introduces a semi-ideal model to systematically analyze drainage flow with full atmospheric physics but an ideal terrain shape. The onset of drainage flow is related to preceding conditions of the wind systems on slopes over which both upslope and downslope flow occur. The results of the semi-ideal model are compared to various analytic solutions, which predict shallower slope flows to occur on steeper slopes. This result along with the appearance of drainage flows over the shallow slopes of the ideal terrain shape are further evidence that insufficient resolution may be the ultimate cause of nocturnal warm biases in the cold-air pool at the MATERHORN site, which includes significantly steeper slopes. Prospects for paramterizing or resolving drainage flows in such real weather models are discussed.

In the concluding chapter, we reflect on the application of large-eddy simulation to all manner of boundary-layer processes and turbulence, especially over complex terrain and for different stratification regimes. This final chapter also summarizes the advancements made by this dissertation, itemized in the following section.

1.6 Summary of contributions

Listed below are the major contributions of this dissertation work:

- Simulations of mountain lee vortices for the first time using high-resolution nested large-eddy simulations.
- Simulations of a cold-air pool and temperature oscillations which develop in the basin of Dugway Proving Ground in Utah for the first time using high-resolution nested large-eddy simulation
- Soil moisture sensitivity study to explain warm biases, frequently present in the aforementioned basin, as a result of missing drainage flow which cannot be resolved due to numerical stability limits
- Derivation of a novel time-step limit which relates the Courant-Friedrichs-Levy stability limit to Mahrer's limit on vertical resolution for terrain-following coordinate systems over steep slopes
- Simulations using the cell perturbation method applied for the first time, to the author's knowledge, to flow over complex terrain
- Determination of the efficacy of the cell perturbation method under various atmospheric stability regimes and with various model input topography
- Analytical solutions to the drainage flow problem with non-traditional Neumann boundary conditions to explain observed dependence on terrain slope
- Semi-ideal simulations for systematic investigation of transient solutions of drainage flow, and their dependence on terrain slope, for the first time with full atmospheric physics
- Derivation of analytical solution of shadow-front propagation for the model geometry used in aforementioned semi-ideal model
- Simulations of the steady state, fully developed velocity and temperature profiles of drainage flow using full atmospheric physics schemes in WRF, and comparison of model results to analytic solutions of similar profiles

Chapter 2

Nested Large-Eddy Simulations of the Displacement of a Cold-Air Pool by Lee Vortices

The following chapter is a reproduction, with slight modification, of Connolly, A., F. K. Chow, and S. W. Hoch, 2020: Nested large-eddy simulations of the displacement of a cold-air pool by lee vortices. *Boundary-Layer Meteorology*, 1–28.

Original Abstract: Mesoscale simulations are typically performed at coarse resolutions which do not adequately represent underlying topography; nesting large-eddy simulations (LES) within a mesoscale model can better resolve terrain and hence capture topographically-induced stable flow phenomena. In the case of the Mountain Terrain Atmospheric Modelling and Observations (MATERHORN) program, large temperature fluctuations were observed on the slope of Granite Peak, Utah, which partially encloses a cold-air pool in the east basin. These flow features are able to be resolved using large-eddy simulation within the Weather Research and Forecasting (WRF) model with $\Delta x = 100$ m, allowing accurate representation of lee vortices with horizontal length scale of $\mathcal{O}(1$ km). At this resolution, terrain slopes become quite steep, and some model warm biases remain in the east basin due to limits on terrain-following coordinates that prevent the model from fully resolving drainage flows with this steep terrain. A new timestep limit for the WRF model related to these steep slopes is proposed. In addition, the initialization of soil moisture is adjusted by drying the shallowest layer to assist the formation of a cold pool in the LES. These real case simulations compare well to observations and also to previously published simulations using idealized configurations to study similar phenomena. For instance, the values of non-dimensional mountain height, which characterize flow regimes in idealized studies, are similar in the real case.

2.1 Introduction

Stably stratified flows, typical of the nocturnal atmospheric boundary layer, are affected by the presence of complex terrain in ways not seen under neutral or unstable conditions (Baines 1998). In large part, this is due to the decoupling of synoptic flows and low-level flows within a near-surface inversion, which inhibits vertical mixing of momentum from aloft. Flow blocking and channeling also play major roles when air parcels are too dense to rise up and over obstacles (Chow et al. 2013). Likely due to this multiplicity of phenomena requiring parametrization, stable conditions also pose special challenges to numerical weather prediction (NWP) models. Planetary boundary-layer (PBL) schemes, the turbulence closures employed in NWP models, are more successful during daytime when convection is the sole dominant process for vertical mixing within the boundary layer (Xie et al. 2012). Typical night-time conditions, under stable stratification when convection does not play a role, are not as well reproduced with these PBL schemes (Holtslag et al. 2013).

Large-eddy simulations (LES) avoid the use of PBL schemes by using grid resolutions fine enough to resolve the most energetic eddies (Deardorff 1980), but this is also more challenging with a stable atmosphere. As stability increases, the scale and magnitude of turbulent fluctuations are diminished and finer meshes are required to resolve the dominant turbulent motions (Pope 2000). As computational power grows to meet this challenge, LES

is becoming more common in atmospheric studies over complex terrain.

Employing microscale LES to formulate mesoscale parametrizations is a stated goal of the Mountain Terrain Atmospheric Modelling and Observations (MATERHORN) program (Fernando et al. 2015). This Office of Naval Research Multidisciplinary University Research Initiative sponsored field campaigns near Granite Peak, at Dugway Proving Ground in Utah, USA (Figs. 2.1 and 2.2). Among the phenomena observed were significant oscillations in the time series of near-surface temperature (e.g. Fig. 2.3) on the slopes of Granite Peak during all quiescent nights of the MATERHORN's autumn campaign (Lehner et al. 2015; Jeglum et al. 2017). Due to the large magnitude of these oscillations (several °C), displacement of the cold-air pool in the neighbouring basin was hypothesized to be important to these oscillations. Jeglum et al. (2017) provided a more complete description of what they call large temperature fluctuations in the MATERHORN data (Jeglum et al. 2017). Their study also presents some evidence of lee vortices (Epifanio 2003) as the mechanism for the cold-air pool displacement, but observational data to support this are limited even with the project's extensive network of sensors. To bridge the gap in the observations, Jeglum et al. (2017) also simulate the lee vortices in the WRF model with a horizontal grid size, $\Delta x = 500$ m, that requires using a PBL turbulence closure. Because the scale of the lee vortices, $\mathcal{O}(1$ km), is near the Nyquist limit of these simulations, the features are arguably underresolved. Considering the challenges faced by both observations and previous modelling efforts, an opportunity is presented for LES, the focus of the present study.

Beyond addressing specific questions raised by the MATERHORN field campaign, further development of the LES technique is motivated by many active fields of research. These include those concerned with boundary-layer dynamics, air quality, and weather forecasting. A much discussed case study at the intersection of these fields is the cold-air pool that often persists around Salt Lake City, Utah. Though larger in scale than the cold-air pool investigated here, the Salt Lake Valley cold-air pool is subject to similar climatology and much of the fundamental dynamics are universal to cold-air pools of all scales. The Salt Lake Valley case brings to light issues brought by insufficient resolution that the mesoscale modelling community faces (Lareau et al. 2013). Particularly under stable conditions and in the presence of terrain, which require fine grids to resolve large gradients in temperature and in surface characteristics, respectively, LES can provide added benefits.

We begin with a brief background (Sect. 2.2) on the fundamental physical processes of interest: cold-air pools, large temperature fluctuations, and lee vortices. We then describe the utilized observational data and detail the configuration of the numerical model. Based on our experience configuring the LES model, we propose a new constraint on the timestep related to steep slopes for terrain-following coordinate systems (Sect. 2.3). We also discuss the model sensitivity to soil moisture initialization and the choice of meteorological forcing (Sect. 2.4). Simulation results demonstrate the relationship between lee vortices and large temperature fluctuations. The structure of the lee vortices, shown in the potential temperature and vorticity fields, and its comparison to similar idealized models of lee vortices, are also discussed (Sect. 2.5).

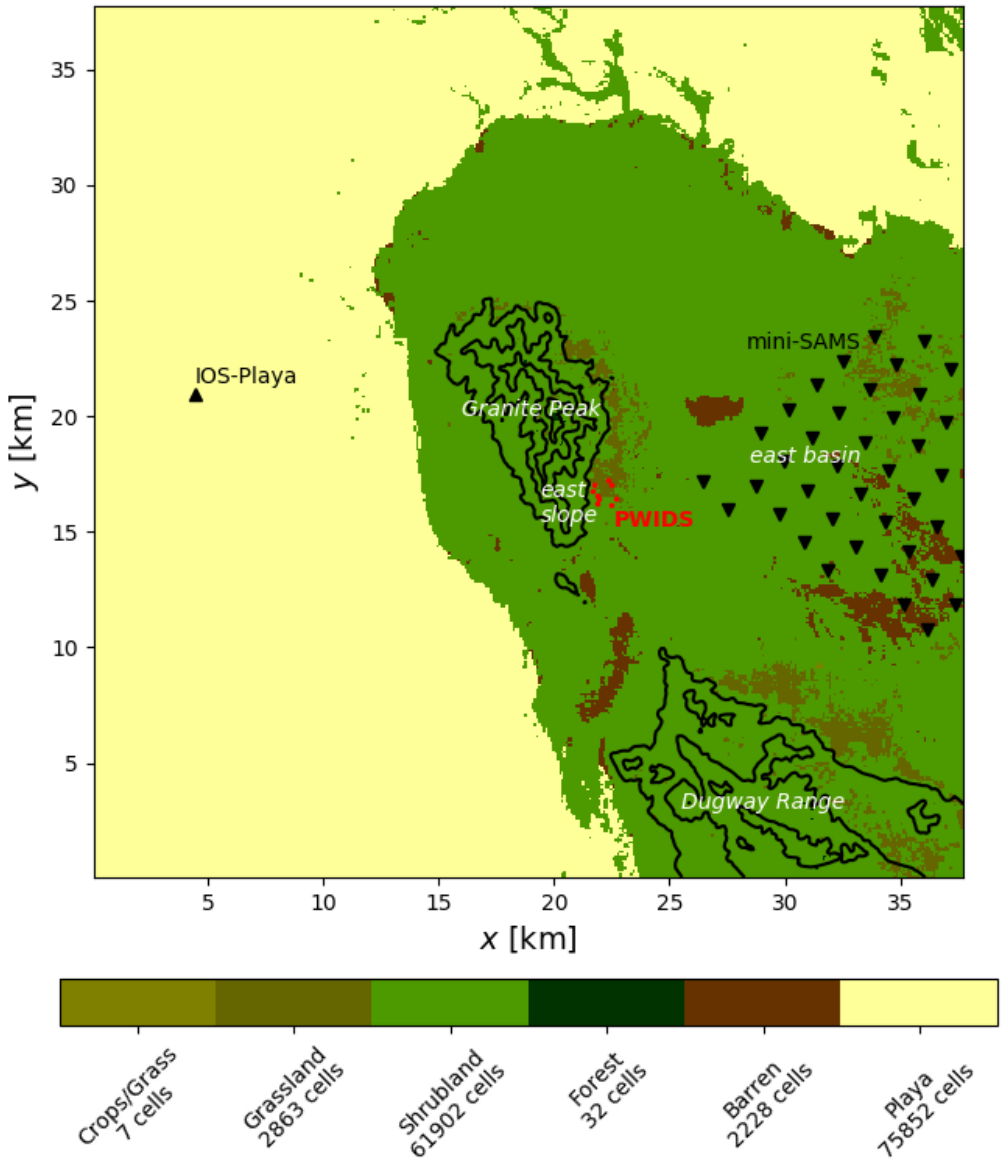

Figure 2.1: Large-eddy simulation domain, d03, with polygons marking the locations of the observation stations used in the current study and white text labels on select geographical areas. The launch site of the radiosonde at IOS-Playa: black, upward-pointed triangle; portable weather instrumentation data systems (PWIDS) on the east slope: red points; 'mini' Surface Atmospheric Measurement Systems (mini-SAMS) array in the east basin: black, downward-pointed triangle. Pixel colours represent categories in the improved land cover data added to the WRF simulation. Topography contour lines have 200-m intervals

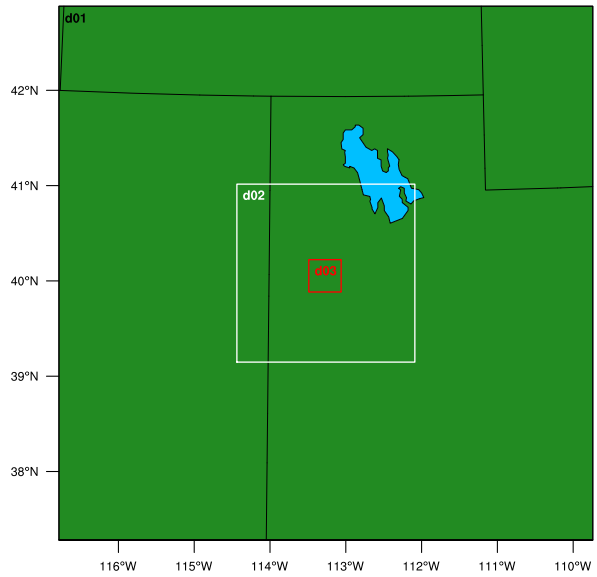

Figure 2.2: Nested domains, d02 and d03, shown in the area covered by d01, the outermost parent domain including the Great Salt Lake in the geographical 'chimney' of Utah state (black lines are state boundaries)

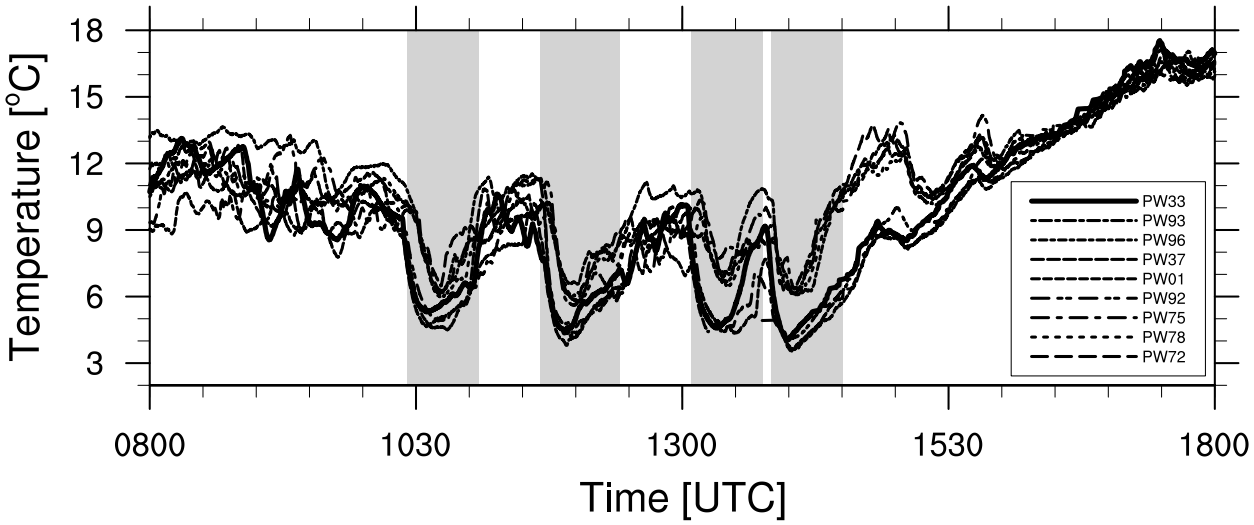

Figure 2.3: Two-metre temperature at the portable weather instrumentation data systems (PWIDS) on the east slope of Granite Peak on 14 October. Locations of the PWIDS are indicated by the red dots in Figure 2.1. Shading indicates periods of observed large temperature fluctuations

2.2 Background

Nocturnal cold-air pools develop readily under synoptically quiescent conditions in the sheltered confines of valleys and basins. They are characterized by increased stability and stagnation in the near-surface air. Figure 2.4 reveals such a cold-air pool in the basin east of Granite Peak, labelled east basin in Fig. 2.1. The formation of a cold-air pool is ultimately due to the diurnal variation of the surface radiation and energy budget as well as the presence of topography. At night, longwave emission becomes the largest term in the radiation and energy balance, driving the cooling of the near-surface air, which leads to the development of a near-surface stable layer. The deepening of the cold-air pool is the result of radiative and turbulent heat exchange processes, including intermittent shear-induced turbulence at the top of the stable layer (Whiteman et al. 2009). This in situ cooling occurs over flat terrain as well, but lower near-surface temperatures may persist if there is sheltering by topography, which reduces the mixing. Additionally, along the sloped sidewalls, the cooling of near-surface air leads to buoyancy-driven drainage flows. These drainage flows converge in topographic depressions of all scales, bringing cold air parcels down the sidewalls to the valley floor or to a point of neutral buoyancy within an extant cold-air pool. This effect is referred to as dynamical cooling (Zardi and Whiteman 2013). Though their relative contributions change throughout the night, the total induced cooling is of comparable magnitude for both in situ and dynamic effects (Burns and Chemel 2014). The temperature anomaly within a cold-air pool could be so significant that a displacement of the cold-air pool would register large changes in temperature at the surface, e.g. along the slope of the basin sidewalls.

In the context of the MATERHORN project, Jeglum et al. (2017) define a large temperature fluctuation as a decrease of at least 3 K within 30 min followed by a recovery of at least 50% of this temperature loss within another hour from the time of minimum temperature. Such a definition effectively isolates large temperature fluctuations associated with displacements of the cold-air pool from fluctuations due to other phenomena such as passing air fronts. The identified large temperature fluctuations are centred on the portion of the slope over which the boundary of the cold-air pool ascends and descends as it is displaced. The study of Jeglum et al. (2017) concluded that the main mechanism for displacing the cold-air pool was an orographic wake similar to those found in the simulations of Epifanio and Rotunno (2005).

From earlier simulations with free slip boundary conditions, Smolarkiewicz and Rotunno (1989) showed that boundary-layer separation is not the impetus for certain wakes in flows with upstream blocking (Fig. 2.5). In these cases, horizontal vorticity is generated baroclinically rather than by friction between the terrain and adjacent airstream. As such, these wakes are not dependent on boundary-layer separation like the wakes of classic bluff body theory. Though wakes whose dynamics are dominated by boundary-layer separation can be found in the atmosphere, they are unlikely to occur in the ranges of the controlling nondimensional parameters, defined below, investigated in the current work (Epifanio 2003). The baroclinicity can be attributed to the deformation of isentropes by the terrain. On the windward slope, Fig. 2.4 shows the prerequisite 'bulging' of isentropes, and on the lee

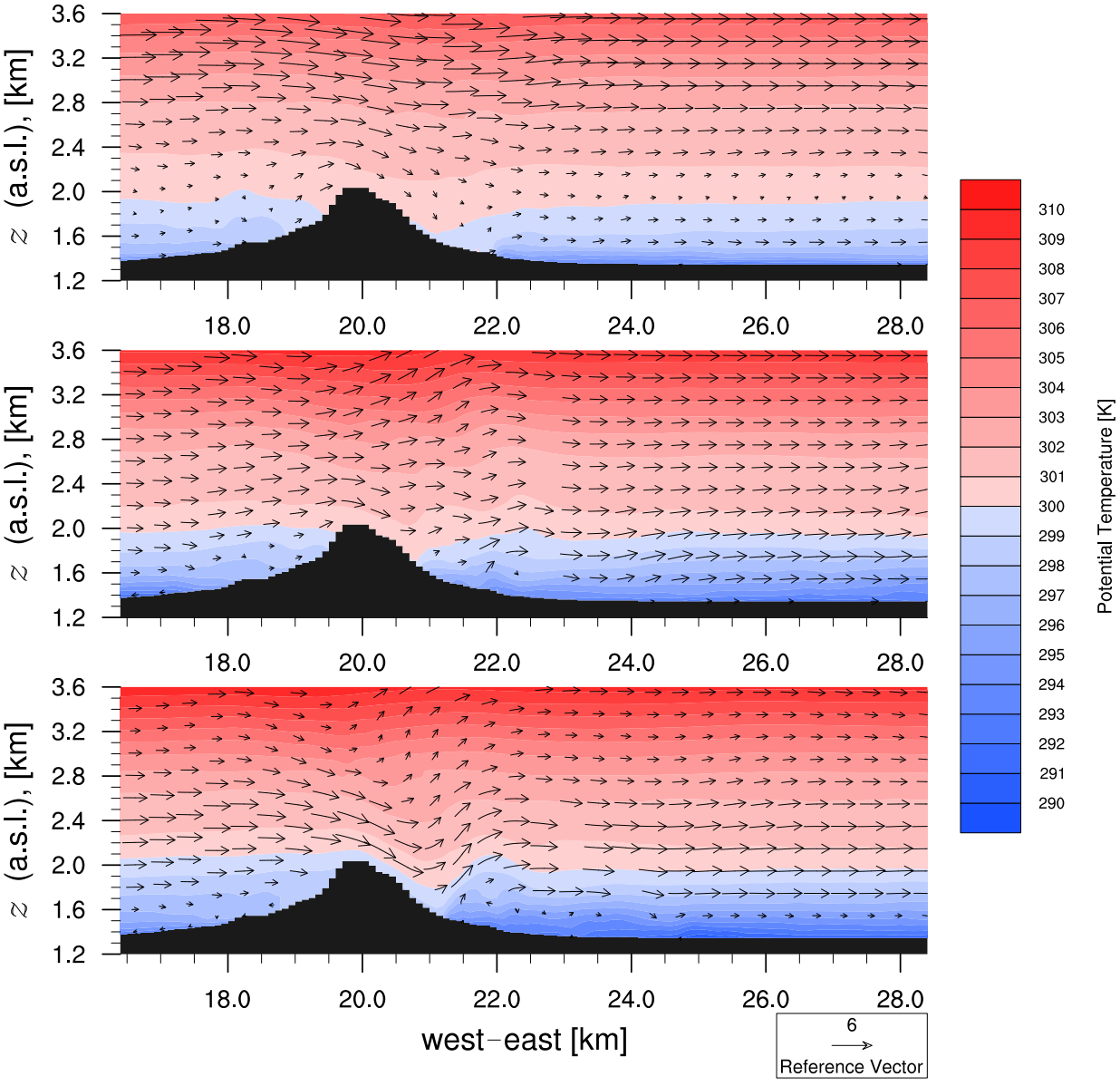

Figure 2.4: Potential temperature contours and quiver plots (U–W) from a west–east slice through the middle of d03 and intersecting Granite Peak in 60%-NAM d03, top: 0930 UTC (0330 MDT), middle: 1200 UTC (0600 MDT), bottom: 1330 UTC (0730 MDT)

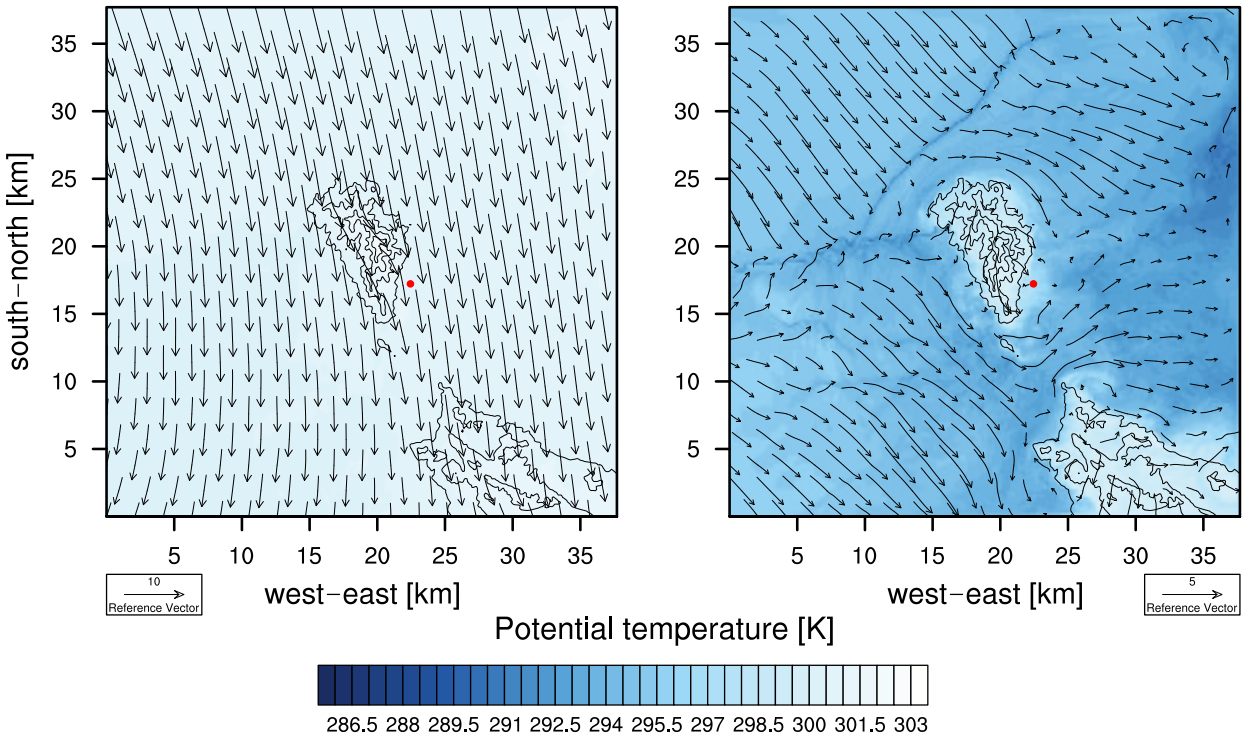

Figure 2.5: Potential temperature filled contours and quiver plot of horizontal velocity from 60%-NAM d03. Left panel: At 885 m a.g.l., north–north–westerly flow aloft passes over the mountain. Right panel: At 28 m a.g.l., north-westerly flow is blocked but lee vortices have not yet formed. Both panels from 0930 UTC. Topography contour lines have 200-m intervals. Red dot marks the location of PWIDS 33

slope, isentropes are deformed by flow over the obstacle, which is termed the descending flow (Fig. 2.4). It is important to distinguish between the descending flow and the drainage flow. Drainage flows are the shallow, buoyancy-driven flows that contribute to cold-air pooling in valleys and basins. Descending flows are on the scale of the obstacle and exist even for neutral flows to conserve mass. In certain stratified flow regimes, the descending flow may result in a horizontal potential temperature gradient (Fig. 2.6). Given a nearly vertical pressure gradient in atmospheric flows, which are approximately hydrostatic, a horizontal component of the potential temperature gradient results in baroclinic generation of horizontal vorticity. This vorticity can be greatly enhanced by the presence of finite amplitude effects resembling hydraulic jumps, i.e., standing density current waves, that might form in the lee of the obstacle (Schär and Smith 1993; Schär and Durran 1997). Ultimately, these processes generate two counter-rotating vertical-axis circulations downwind of the obstacle, which are referred to as lee vortices (Epifanio and Durran 2002a,b).

Work cited above considers obstacles with idealized topography and further simplify the problem by using one or two layers with constant stratification and uniform free stream

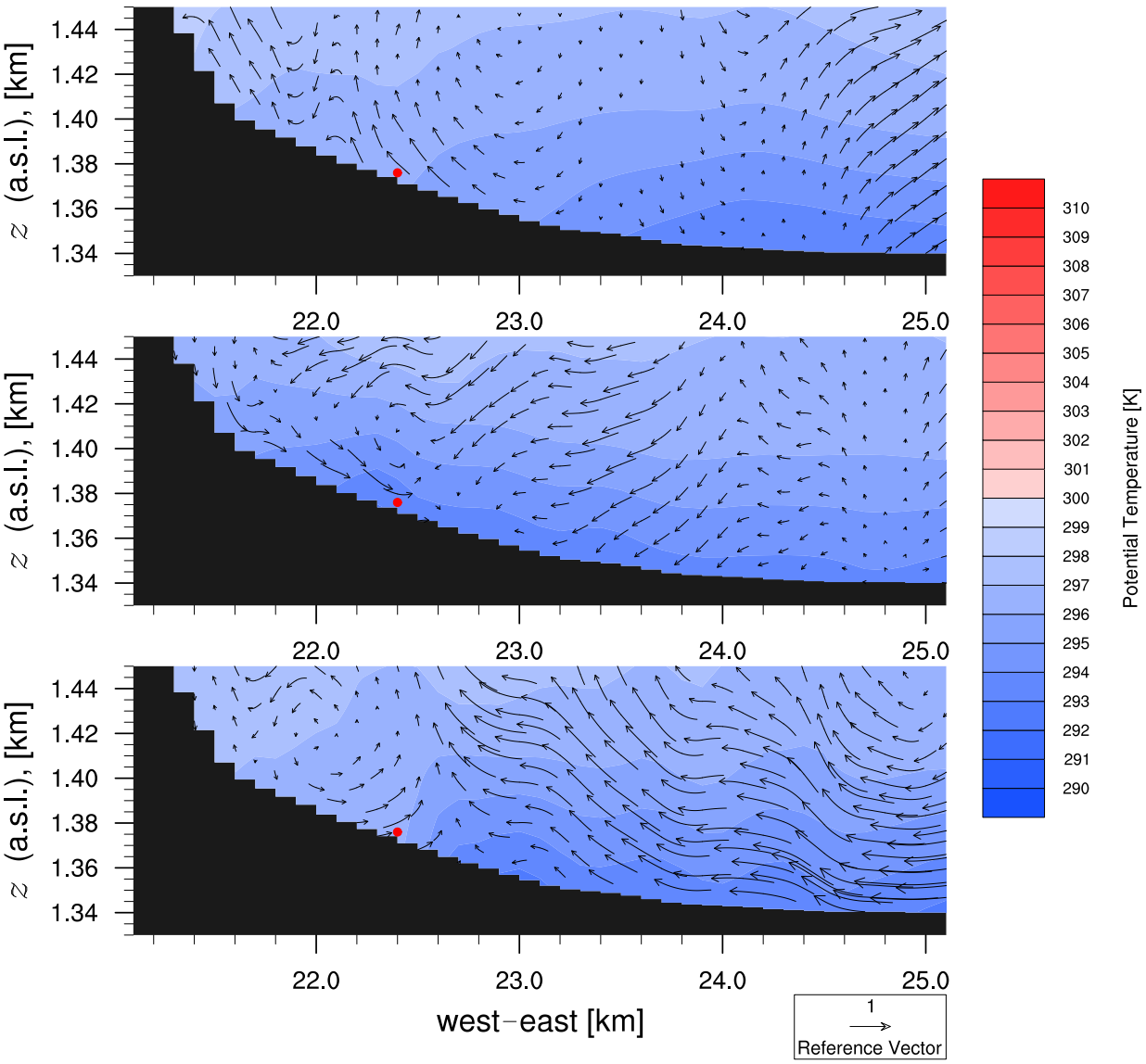

Figure 2.6: Potential temperature contours and quiver plots (U–W) from a west–east slice through PWIDS 33 in 60%-NAM d03. Top: 0950 UTC (0350 MDT), middle: 1020 UTC (0420 MDT), bottom: 1050 UTC (0450 MDT)

velocity, as in towing tank experiments, e.g. Baines (1979). A relevant parameter, the non-dimensional mountain height (inverse Froude number), is well defined in the ideal problem,

$$\epsilon = \frac{Nh}{U}, \tag{2.1}$$

where N is the buoyancy frequency, h is the height of the mountain, and U is the freestream velocity. The horizontal aspect ratio, β, taken as the cross-stream width of the mountain over the along-stream length, is also relevant to this three-dimensional problem in which fluid flows both over and around an obstacle. Given a value of β, there is a critical ϵ above which we expect lee vortices to form. Though the value of this lower bound is determined by the specific geometry in question, for symmetrical and slightly elongated ($\beta \gtrsim 1$) ridges, $\epsilon \approx 1$. Additionally, for the baroclinic mechanism to dominate the wake dynamics, an upper bound is given as $\epsilon \lesssim 10$ based on ideal simulations. At Granite Peak, the mountain geometry gives $\beta \approx 1$, so a moderate value for non-dimensional mountain height, $\epsilon = \mathcal{O}(1)$, suggests lee vortices would form by the baroclinic generation mechanism (Epifanio 2003).

Our study extends the work of idealized simulations of orographic wakes with upstream blocking by including meteorological forcing as well as realistic topography and heterogeneous surface and soil properties. A consequence of the realistic topography is the formation of a cold-air pool in the east basin. The displacement up the slope of this cold-air pool by lee vortices in the wake produces large temperature fluctuations. Additionally, we are able to analyze model skill by comparing our real model to observational data and test the sensitivity to soil moisture and large-scale forcing data.

2.3 Methods

Field Observations

The vast observational network available from the MATERHORN field experiment includes sensors of the Granite Mountain Atmospheric Science Testbed (GMAST), and heavily instrumented intensive observing sites (IOS), described in detail in Fernando et al. (2015). Here, we mainly use three observational assets labelled in Fig. 2.1. We compare our model results with the upstream soundings from IOS-Playa. We also use the 'mini' Surface Atmospheric Measurement Systems (mini-SAMS) array located in the basin east of Granite Peak (east basin) to determine the strength of the nocturnal cold-air pool. Thirdly, a subset of portable weather instrumentation data systems (PWIDS) deployed near IOS-ES on the eastern slope of Granite Peak (east slope) record the large temperature fluctuations observed during intensive observation period 6 (IOP) on 14 October 2012.

Nested WRF Models

The simulations presented here were performed with the Weather Research and Forecasting (WRF) model developed by the National Center for Atmospheric Research (NCAR), version

Table 2.1: Information on nested simulation domains

Domain	$\Delta x = \Delta y$	$\Delta z_{\min}$ - $\Delta z_{\max}$	Nx·Ny·Nz	Δt [s]	Closure
01	6.3 km	57 m - 170 m	100·100·121	30	MYJ
02	2.1 km	57 m - 170 m	100·100·121	10	MYJ
03	100 m	57 m - 170 m	379·379·121	0.2	TKE 1.5

3.7.1 (Skamarock et al. 2008). The dynamic core of the model provides a numerical solution of the compressible flow equations with a third-order Runge–Kutta time advancement scheme, with split time stepping to handle acoustic modes, as well as fifth-order horizontal advection and third-order vertical advection.

Physical parametrizations employed in the simulations include the Noah land-surface model (Chen and Dudhia 2001), the Rapid Radiative Transfer Model for longwave radiation (Mlawer et al. 1997), the Dudhia shortwave radiation model (Dudhia 1989), and a surface-layer parametrization based on Monin–Obukhov similarity theory (Chen et al. 1997). Following Massey et al. (2014), a 'hybrid' soil thermal conductivity scheme is implemented in the WRF model to correct the tendency for this model to underpredict the diurnal temperature range. 'Hybrid' refers to the use of two forms of parametrizations: those of Johansen (1975) are used for all soil classes except silt loam and sandy loam, which are handled by another scheme proposed by McCumber and Pielke (1981).

Figure 2.2 illustrates the nested domain set-up, while Table 2.1 provides additional information on each domain in the nest. Domains 1 and 2 resemble typical domains used in mesoscale NWP and use a PBL scheme for their turbulence closure (Janjić 1994). Domain 3 is run at large-eddy permitting resolution. Specifically, 100 m horizontal grid spacing and vertical grid spacing between 57 and 170 m are used. Using a staggered grid, the model's first half level where horizontal velocities are computed is approximately 28 m above ground level (a.g.l.). This near-surface vertical resolution is necessarily quite coarse due to the stability constraint related to resolving steep slopes, as further discussed below, but still allows a reasonable representation of the lee vortices. For this finest resolved domain we use a turbulent kinetic energy (TKE) 1.5-order LES turbulence closure, appropriate at higher resolutions (Deardorff 1980; Wyngaard 2004).

All domains are initialized with meteorological data either from the Global Forecast System (GFS) or from the North American Mesoscale (NAM) model reanalysis, made publicly available by the National Oceanic and Atmospheric Administration (NOAA). Both models are from the National Center for Environmental Protection (NCEP) but differ in horizontal resolution, GFS at 0.5 ° ($\sim$ 50 km) and NAM at a finer 12 km. The model is initialized at 0000 UTC 14 October 2012, 1800 local time (MDT) 13 October 2012. Model initialization precedes IOP 6 of the MATERHORN autumn campaign by 8 h for model spin-up, which is excluded from the analysis. The GFS or NAM data provide the lateral boundary conditions for the coarsest grid throughout the duration of the simulation. For the nested domains, lateral boundary conditions are provided through a one-way nesting procedure.

Table 2.2: Information on model configurations used in the tests of sensitivity to soil moisture and meteorological forcing

Name	Forcing source	Forcing resolution	Soil moisture
Min-NAM	NAM	12 km	All layer volumetric water content set to 0.005 m^3 m^{-3} everywhere but lakes
60%-NAM	NAM	12 km	5 cm volumetric water content set to 60% of NAM values everywhere but lakes
Full-NAM	NAM	12 km	Unaltered NAM values
60%-GFS	GFS	0.5°	5 cm volumetric water content set to 60% of GFS values everywhere but lakes
Full-GFS	GFS	0.5°	Unaltered GFS values

Land Cover and Topography

Of the land-cover data provided by NCAR for ready use with the WRF model, the finest available resolution is 30 arcsec, which is about 1 km at middle latitudes. Our simulations use a higher resolution land cover dataset created for 4DWX, an operational model used by Army forecasters at Dugway Proving Ground (Liu et al. 2008). These data are resolved at 1 arcsec and contain additional land-cover types: lava, playa, and white sand.

Similarly, standard topography data available with the WRF model are at resolutions no higher than 30 arcsec. Because the LES domain is much finer, we implement the United States Geological Survey (USGS) National Elevation Dataset (Gesch et al. 2002) topography with a resolution of 1/3 arcsec, roughly 10 m at these latitudes, for the LES domain.

Soil Moisture Initialization

The initialization of soil moisture is varied to test model sensitivity and to correct a bias in near-surface temperatures (Massey et al. 2014). Higher model soil moisture results in higher soil conductivity and heat capacity. The resulting increase in soil heat storage leads to model daytime cold biases and night-time warm biases (Zhang et al. 2013; Massey et al. 2016). To mitigate these errors, the 50-mm soil moisture is initialized to 60% of the values provided by the forcing dataset for two simulations, 60%-NAM and 60%-GFS. The sensitivity study also includes simulations with unaltered soil moisture, Full-NAM and Full-GFS, and with soil moisture further reduced to the minimum allowed by the WRF model, the Min-NAM simulation (Table 2.2).

Timestep and Vertical Resolution Limits

One of the challenges with fine horizontal resolution over complex terrain is that the resolved slopes become steeper with increasing grid resolution, and can lead to numerical stability issues that are limiting, potentially prohibitive. To address this, the mesoscale simulations

and the LES must differ in the relationship between horizontal grid size and timestep. From Table 2.1, note the two larger domains conform to the rule-of-thumb Courant limit developed for mesoscale simulations in the WRF model,

$$\Delta t \lesssim C\Delta x^*, \tag{2.2}$$

with Δt being the larger, non-acoustic timestep, $C = 6$ s km^{-1} and Δx^* taken as the smallest horizontal grid spacing. In the more finely resolved LES, the timestep suggested by this rule of thumb, $\Delta t = 0.6$ s, and a slightly reduced timestep, $\Delta t = 0.4$ s, lead to the LES terminating due to numerical instability almost immediately after initialization. Greatly reducing the timestep through trial and error to $\Delta t = 0.2$ s was required for model stability. This more restrictive timestep limit can be explained by modifying the Courant limit with another stability limit that follows from the work of Mahrer (1984) on the use of a terrain-following coordinate system over steep terrain,

$$\tan\alpha < b\frac{\Delta z}{\Delta x}, \tag{2.3}$$

for maximum slope α over a grid spacing of Δx and typically $1 \leq b \lesssim 5$ (Poulos 1996; Zhong and Chow 2013).

We hypothesize that the Mahrer condition must be combined with the Courant limit for cases in which the distance between a near-surface grid point and the sloped boundary in the true horizontal directions is less than the grid spacing. With this assumption, we take $\Delta x^* = \Delta z/\tan\alpha$ as a more restrictive length scale in the Courant condition,

$$\Delta t \lesssim C\frac{\Delta z}{\tan\alpha}, \tag{2.4}$$

and substitute (2.3), the inequality constraint on $\tan\alpha$,

$$C \cdot \frac{\Delta z}{b\frac{\Delta z}{\Delta x}} \lesssim C\frac{\Delta z}{\tan\alpha}, \tag{2.5}$$

to propose a new rule-of-thumb for timestep selection over steep slopes which ensures meeting the requirements of both the Courant condition and the steep terrain condition,

$$\Delta t \lesssim \frac{C}{b}\Delta x \lesssim C\frac{\Delta z}{\tan\alpha}. \tag{2.6}$$

The second inequality simply restates the steep terrain condition while the first inequality of (2.6) is a new condition that takes the same form as the WRF model's original rule-of-thumb Courant condition: direct proportionality between timestep and horizontal grid spacing, now with a smaller coefficient, C/b, as $b \geq 1$.

Using this new condition, the timestep chosen by trial-and-error, $\Delta t = 0.2$ s, implies a value of $b \approx 3$ which is typical for this coefficient. Further, our attempts to refine vertical

Table 2.3: Mini-SAMS 2-m temperature biases calculated for various time intervals: pre-sunrise, post-sunrise, and the whole morning of IOP 6

Simulation	Bias (RMSE) [K] 0800< t <1340 UTC	Bias (RMSE) [K] 1340< t <1800 UTC	Bias (RMSE) [K] 0800< t <1800 UTC
Full-GFS d03	6.59 (6.61)	1.50 (2.60)	4.35 (5.24)
Full-NAM d03	5.47 (5.48)	1.01 (2.18)	3.50 (4.35)
60%-NAM d03	3.03 (3.07)	0.82 (1.25)	2.05 (2.43)
Min-NAM d03	1.70 (1.77)	−0.20 (0.78)	0.86 (1.42)

resolution lead to model degradation, likely due to the violation of the second inequality, the steep terrain limit. Maximum resolved slopes are $\alpha \approx 45°$, such that vertical refinement is limited by

$$\Delta z \gtrsim \tan\alpha \frac{\Delta x}{b} \approx (1)\frac{100}{3} = 33.3 \,, \tag{2.7}$$

with Δz in m, which roughly matches the height of our first half model level, 28 m a.g.l., where horizontal velocities are computed. As such, the vertical resolutions used in the current simulations are necessarily coarse to ensure stability. The variable vertical spacing is determined through the WRF model's default grid stretching procedure upon specifying 121 vertical levels and retaining the default model top at approximately 500 hPa.

2.4 Model Validation and Sensitivity Tests

Sensitivity to Soil Moisture

Figure 2.7 compares radiosonde observations of potential temperature, wind direction, and wind speed to those from the large-eddy simulations of Min-NAM, 60%-NAM, and Full-NAM simulations. The radiosondes released from IOS-Playa, marked in Fig. 2.1, on 14 October at 0850 UTC (0250 MDT) and 1203 UTC (0603 MDT) are upstream of Granite Peak during the time period in which large temperature fluctuations are observed on the east slope. Except for the minimal soil moisture simulation, Min-NAM, the first 1 or 2 grid points in the WRF model exhibit the expected nocturnal warm bias. Over the next several grid points above ground level, the model shows a cold bias. Such a 'smoothed' temperature profile supports the hypothesis that 2-m temperature positive biases are due to an overly dissipative parametrization of the nocturnal boundary layer. The Min-NAM simulation exhibits an atypical nocturnal cold bias at the lowest model levels, indicating an overcorrection of soil moisture. Further aloft, differences between simulations with varied soil moisture initializations vanish and the WRF models, regardless of soil moisture, compare similarly well to the observation soundings above the first few grid levels.

Turning to instruments downstream of the mountain in the east basin containing the cold-air pool, Fig. 2.8 shows time series of 2-m temperature biases averaged over the 40

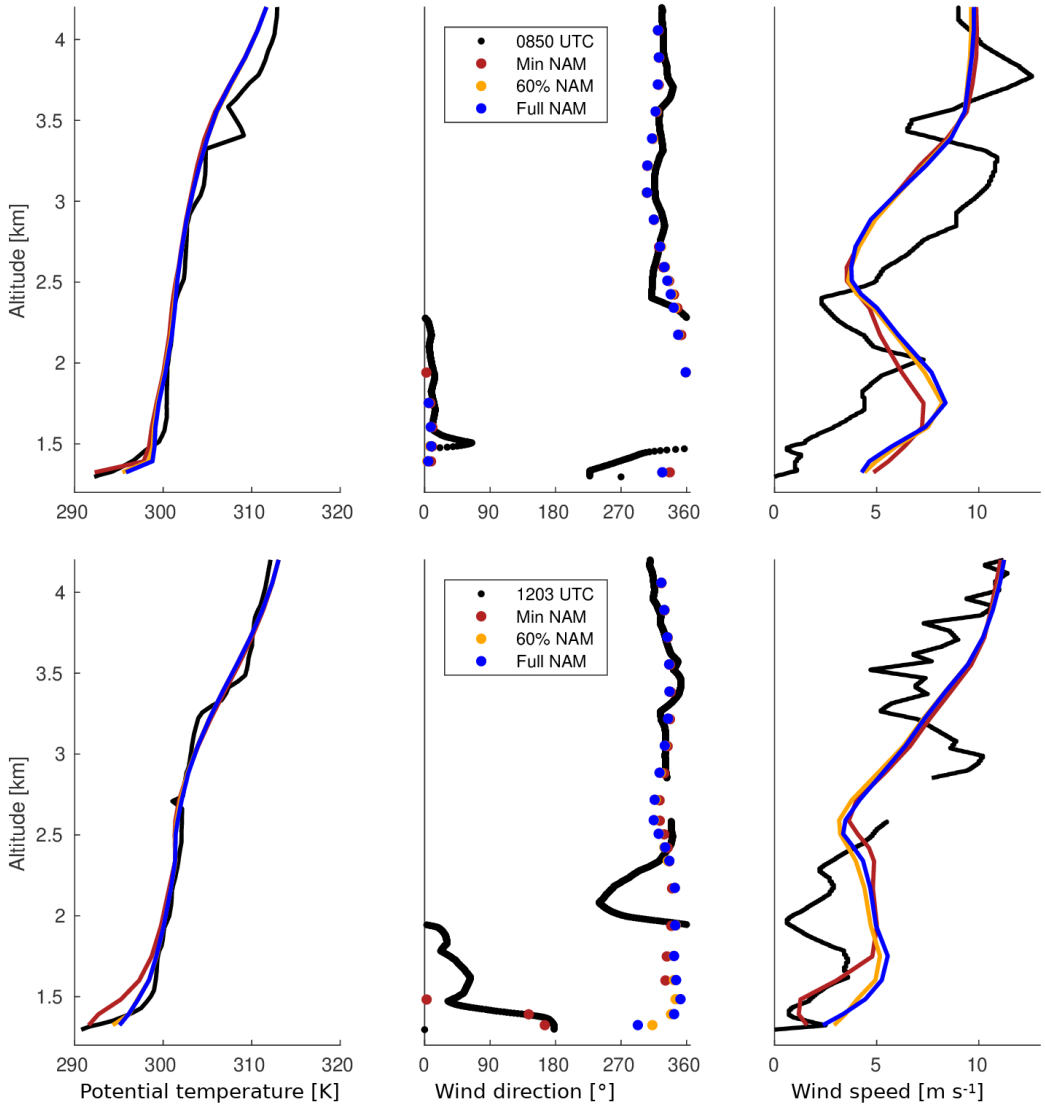

Figure 2.7: Soundings released at 0850 and 1203 UTC from the radiosonde station marked IOS-Playa in Fig. 2.1 compared to the large-eddy simulations, Min-NAM d03, 60%-NAM d03, and Full-NAM d03

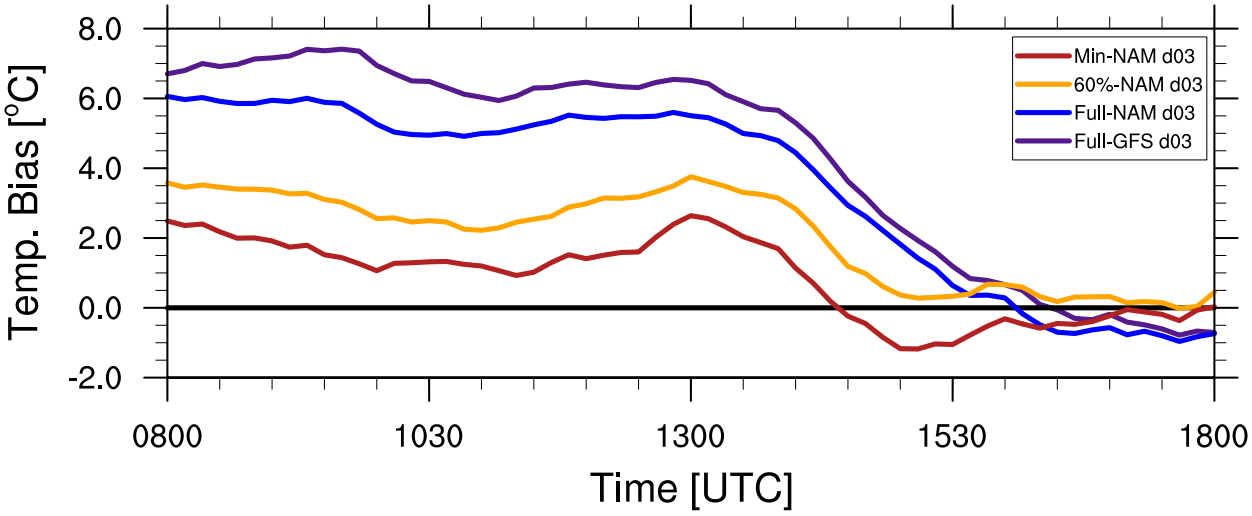

Figure 2.8: Biases of 2-m temperature, calculated as modelled minus observed temperature averaged over 40 mini-SAMS weather stations in the east basin, comparing the large-eddy simulations (d03) of the Min-NAM, 60%-NAM, Full-NAM, and Full-GFS simulations

mini-SAMS stations within the LES domain of the Min-NAM, 60%-NAM, Full-NAM, and Full-GFS simulations. In the east basin, the WRF model's near-surface temperature bias remains positive, i.e. a warm bias, until some time after sunrise (1340 UTC or 0740 MDT). During these hours before sunrise, simulations with increasing soil volumetric water content show increasingly warm biases. Unaltered GFS soil moisture produces the worst errors (Table 2.3). In the east basin, even the model with the driest soil has this characteristic warm bias, unlike the first grid level at the radiosonde site. The presence of the nocturnal warm bias in the east basin, even with minimal soil moisture as in the Min-NAM simulation, is likely due to a combination of excess mixing in the stable boundary layer and a lack of cold air inflow by drainage flows. Jeglum et al. (2017) also reported a nocturnal warm bias in their simulations with coarser horizontal resolution (500 m) even though they were able to use finer vertical resolution due to more moderate terrain slopes at this resolution.

Dynamic cooling is entirely absent because drainage flows are too shallow to be resolved in the current simulations (Smith and Porté-Agel 2014). Further, as stability inhibits the mixing of potentially warmer air aloft, this exacerbates the long-standing modelling challenge of maintaining a strongly stable near-surface inversion. Considering the condition in Eq. 2.6, vertical resolutions fine enough to resolve the drainage flows, $\mathcal{O}(1\text{ m})$, lead to numerical instabilities in a terrain-following coordinate system over slopes as steep as those of Granite Peak, at least for current horizontal resolutions. Recent advances with the immersed boundary method may help resolve this issue in the future (Arthur et al. 2018; Bao et al. 2018; Wiersema et al. 2018). (For example, Arthur et al. (2018) simulated drainage flows on Granite Peak in a semi-idealized set-up with 25-m horizontal resolution.) Until these numer-

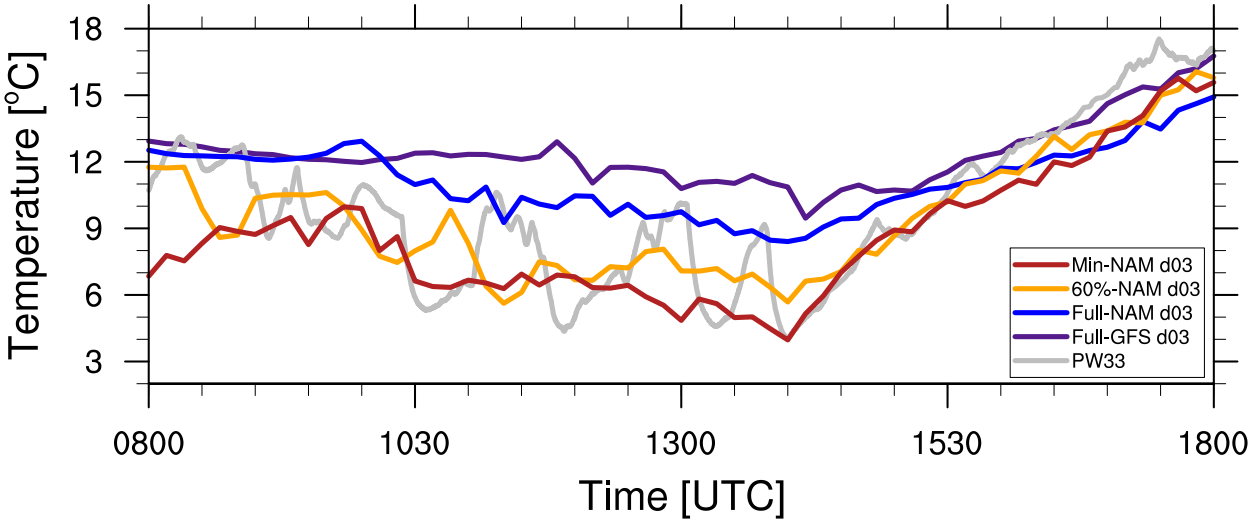

Figure 2.9: Two-metre temperature from PWIDS 33 on the east slope of Granite Peak, comparing large-eddy simulations forced by NAM with full, 60%, and minimal soil moisture initializations as well as the full soil moisture LES forced by GFS

Table 2.4: East slope PWIDS 2-m temperature biases calculated for various time intervals: pre-sunrise, post-sunrise, and the whole morning of IOP 6

Simulation	Bias (RMSE) [K] $0800 < t < 1340$ UTC	Bias (RMSE) [K] $1340 < t < 1800$ UTC	Bias (RMSE) [K] $0800 < t < 1800$ UTC
Full-NAM d03	1.84 (2.31)	−0.52 (1.48)	0.81 (2.00)
60%-NAM d03	−0.44 (1.65)	−0.89 (1.17)	−0.62 (1.46)
Min-NAM d03	−1.85 (2.34)	−1.65 (1.83)	−1.74 (2.11)
Full-GFS d03	2.74 (3.19)	0.72 (1.64)	1.84 (2.62)
60%-GFS d03	1.13 (2.11)	−0.73 (1.32)	0.32 (1.82)

ical techniques are available, shallow drainage flows in steep terrain will remain a challenge for NWP models. Without this dynamic cooling, nocturnal warm biases can be expected in areas of cold-air pooling even when minimizing soil moisture to tune the in situ cooling.

Figure 2.9 shows time series of 2-m temperature from one east slope PWIDS station, PWIDS 33, against spatially interpolated data from the WRF model with various initial soil moisture fields. For the same LES models, Table 2.4 gives 2-m temperature biases averaged over all nine PWIDS (only eight when PWIDS 37 is missing data) on the east slope of Granite Peak. The biases are further averaged over different time periods. Though the Full-GFS simulation performs best after the morning transition, the full soil moisture simulations have the largest errors during the period of large temperature fluctuations at night when they show strong warm biases. The Min-NAM simulation exhibits an atypical nocturnal cold bias, again indicating an overcorrection of soil moisture. The simulation initialized with 60% soil

moisture appears to be a good compromise, with a mean bias less than half a degree Celsius during the pre-sunrise period (Table 2.4). The simulations initialized with 60% soil moisture are selected for the comparison of meteorological forcing and the discussion of dynamics in the following sections.

Sensitivity to Meteorological Forcing Data

Two meteorological forecast products are chosen to initialize all domains and to force d01, the outermost mesoscale domain, by providing lateral boundary conditions. Though commonly used, the relatively coarse GFS resolution (0.5 °) may not suffice over complex terrain where topographically-forced flows are expected. To address this concern, the other forecast product, the finer resolved (12 km) NAM model, provides finer resolved forcing data in the current simulations. However, neither the NAM-forced nor GFS-forced LES produce large temperature fluctuations when initialized with full soil moisture fields (Fig. 2.9), i.e. for Full-NAM and Full-GFS simulations, so the attention of this section narrows to models initialized with 60% soil moisture, 60%-NAM and 60%-GFS simulations.

Figure 2.10 compares potential temperature, wind direction, and wind speed from the radiosondes to those from d03 of 60%-GFS and of 60%-NAM simulations. The radiosondes released from IOS-Playa, marked in Fig. 2.1, on 14 October at 0850 UTC (0250 MDT) and 1203 UTC (0603 MDT) are upstream of Granite Peak during the time period in which large temperature fluctuations are observed on the east slope. At the lowest grid level, potential temperature does not differ between the models as much as in the soil sensitivity tests. Both models show a near-surface inversion that is weaker than in the observations partly due to a near-surface warm bias. Wind direction between models and observations agree above ridge height, ≈2.3 km above sea level (a.s.l.). Below this height, differences are apparent, particularly at the lowest levels. This disagreement may result from differences in the extent of blocking between the modelled and physical flows. Wind speed agreement is good on average, but the observations show high wavenumber oscillations that neither model resolves.

Turning to instruments downstream of the mountain in the east basin containing the cold-air pool, Fig. 2.11 shows 2-m temperature biases averaged over the 40 mini-SAMS stations within the LES domain. NAM-forced simulations slightly outperform those forced by GFS but all models exhibit a persistent nocturnal warm bias despite the soil moisture correction. In the late morning, some time after sunrise (1340 UTC or 0740 MDT), both mesoscale simulations remain too warm though with greatly reduced magnitudes compared to biases before sunrise. At the same time, LES model biases decrease to nearly zero in the east basin.

In the time series of 2-m temperature on the east slope of Granite Peak shown in Fig. 2.12, 60%-NAM d03 and the 60%-GFS d03 show more appreciable differences than in the upstream radiosonde soundings or in the average temperature bias across the mini-SAMS array. Further, these disparities have greater importance in this study motivated by the signature of large temperature fluctuations in these time series. The mesoscale simulations,

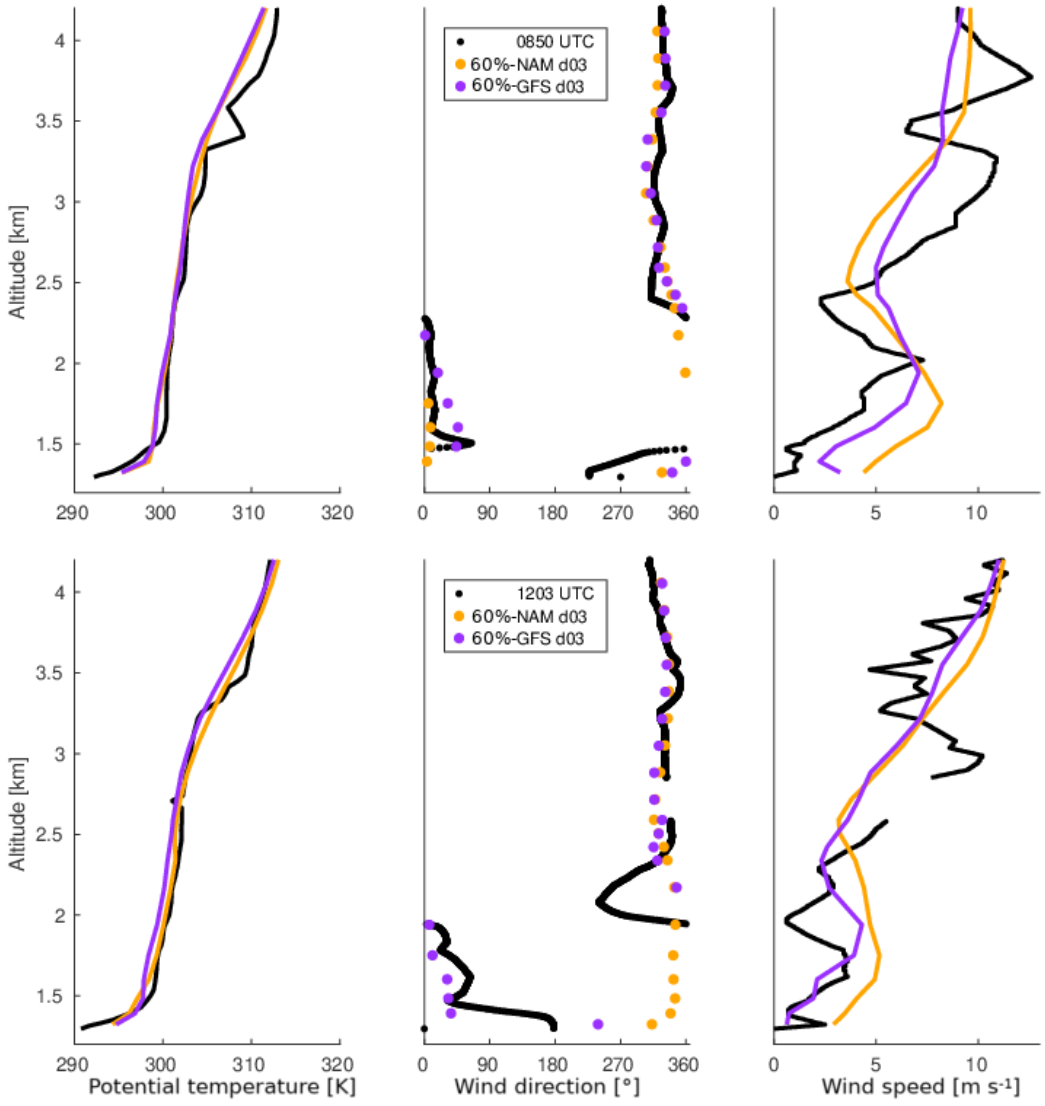

Figure 2.10: Soundings released at 0850 (top) and 1203 UTC (bottom) from the radiosonde station marked IOS-Playa on Fig. 2.1 compared to the large-eddy simulations, 60%-NAM d03 and 60%-GFS d03

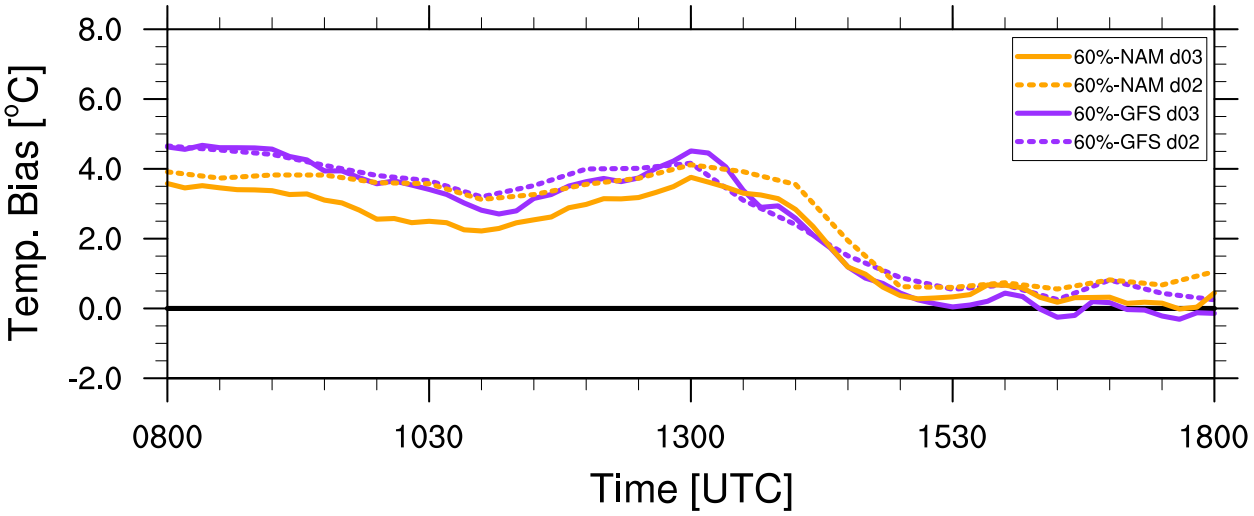

Figure 2.11: Biases of 2-m temperature, calculated as modelled minus observed temperature averaged over 40 mini-SAMS weather stations in the east basin, comparing the finer mesoscale simulation (d02) and the large-eddy simulation (d03) from NAM and GFS both with the 60% soil moisture initialization

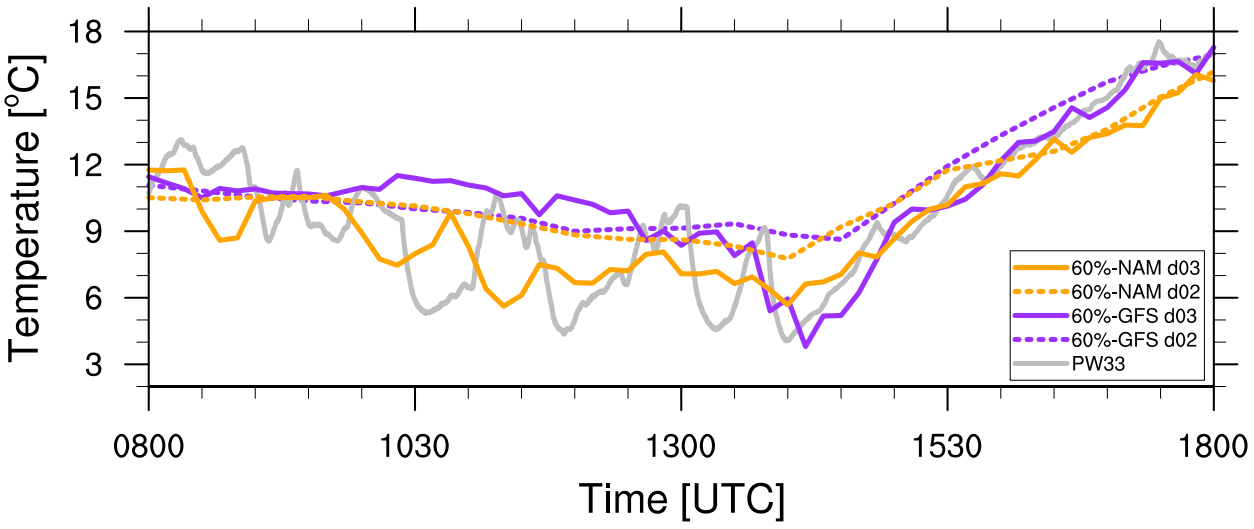

Figure 2.12: Two-metre temperature from a PWIDS station on the east slope of Granite Peak, comparing the finer mesoscale simulation (d02) and the large-eddy simulation (d03) from NAM and GFS both with the 60% soil moisture initialization

60%-NAM d02 and 60%-GFS d02, contain no large temperature fluctuations and the 60%-GFS d03 LES only resolves one large temperature fluctuation. Interestingly, the timing of the sole large temperature fluctuation reproduced by 60%-GFS d03 is nearly perfect. However the study of this large temperature fluctuation, the latest, is complicated by the fact that recovery of temperature occurs after sunrise (1340 UTC or 0740 MDT) such that any warming cannot be fully attributed to the recession of the cold-air pool. Two large temperature fluctuations occur in 60%-NAM d03, but they are not precisely concurrent with the observed temperature fluctuations. Even with errors predicting the timing, 60%-NAM d03 has the lowest magnitude bias during the early morning period between 0800 and 1340 UTC (0200 and 0740 MDT, Table 2.4). As such, 60%-NAM d03 seems to capture the phenomenon of large temperature fluctuations best, and results from this configuration will be the focus of the following sections.

2.5 Results and Discussion

Modelled Large Temperature Fluctuations

Four observed large temperature fluctuations are highlighted grey in Fig. 2.3, the time series of 2-m temperature from nine PWIDS on the east slope of Granite Peak. The first two of these, recorded at all PWIDS on the east slope, are roughly concurrent with two large temperature fluctuations in the LES, d03, of the 60%-NAM simulation (Fig. 2.12). To analyze the occurrence of multiple large temperature fluctuations within the same model, we focus on 60%-NAM d03 during the period of large fluctuations roughly concurrent with the two in the observation data.

In 60%-NAM d03, a large temperature fluctuation begins at 0950 UTC (0350 MDT). Temperatures decrease by 3 K to a first temperature minimum at 1020 UTC (0420 MDT), until recovering most of the temperature loss by 1050 UTC (0450 MDT). Immediately following this temperature recovery, another large temperature fluctuation is initiated and the temperature decreases by just over 4 K by 1120 UTC (0520 MDT). This time, the temperature does not fully recover and rises only 2 K by 1140 UTC (0540 MDT). During these times, the occurrence of large temperature fluctuations in the LES reduces the temperature on the east slope of Granite Peak in comparison to its parent mesoscale model, which does not resolve any large fluctuations (Fig. 2.12).

Though 60%-NAM d03 resolves large temperature fluctuations, the temperature minima remain several K higher than the minima from field data. This is due to the nocturnal warm bias in the basin to the east of the Granite Peak, which remains positive even with minimal soil moisture (Fig. 2.8). When insufficiently cold basin air is displaced up the mountain slope to the location of PWIDS 33 in the LES model, a smaller temperature decrease is recorded than when colder basin air is displaced up the mountain in reality.

Cold-Air Pool Displacement by Lee Vortices

Flow visualizations are presented as evidence of lee vortices being the mechanism for the cold-air pool displacement. The instances of large temperature fluctuations in the model time series coincide with the existence of vertical axis circulations with a return flow that advects air from the east basin to the east slope.

Figure 2.5 shows the state of the horizontal flow and temperature fields from the first half model level at 28 m a.g.l. from 60%-NAM d03 at 0930 UTC (0330 MDT), immediately before a large temperature fluctuation is initiated. We see the flow aloft is north–north–westerly (left panel), as in the radiosondes, such that lee vortices would form near the stations on the east slope of Granite Peak. Inspection of lower level flow at this time shows that the flow is blocked, though no lee vortices are present before the model large temperature fluctuation initiates (right panel). By 0940 UTC (0340 MDT), lee vortices have begun to form with a return flow that advects colder air from the east basin cold-air pool toward the east slope stations (Fig. 2.13). Temperature there continues to decrease over the next half hour while the return flow is present. Then, the centres of the circulations are advected downstream and temperature on the east slope begins to recover at 1020 UTC (0420 MDT) as the zonal component of the wind switches from easterly to westerly (Fig. 2.14). During these times, another feature of lee vortices becomes visible. These are the 'warm cores' of the lee vortices predicted by ideal simulations (Schär and Durran 1997).

During the interim of the two largest model temperature fluctuations, PWIDS 33 occupies the boundary of colder (darker blue) air to the east and warmer (lighter blue) air upslope to the west (Fig. 2.15). The lee vortices are being advected farther downstream while simultaneously growing in size. Eventually, a second large temperature fluctuation is initiated by these same lee vortices, now large enough for the return flow to reach the east slope stations yet again. Similar to the previous fluctuation, temperature decreases while the return flow is present. Unlike the previous large temperature fluctuation, the second recovery in temperature is not associated with advection of the circulations farther from the observation station. Instead, through the gap between Granite Peak and the Dugway Range to the south, flows are growing in strength until they eventually 'wash out' the lee vortices (Fig. 2.16).

From this series of events, we see that multiple large temperature fluctuations can be associated with the same lee vortices that have changed size or position relative to the observation site. While noting a single pair of lee vortices may be associated with multiple large temperature fluctuations, it is also worth noting that there may be lee vortices without any large temperature fluctuations. This is the case in Full-NAM d03: lee vortices occur (Fig. 2.17), but no *large* temperature fluctuation is recorded on the east slope. Though Full-NAM d03 shows fluctuations in temperature at the same time 60%-NAM d03 does, the magnitude of the fluctuation is diminished due to the increased warm bias in the cold-air pool. As the temperature decrease is less than 3 K, this event does not qualify as a large temperature fluctuation by the threshold values defined by Jeglum et al. (2017) though it is dynamically similar in that lee vortices are associated with some fluctuations in temperature

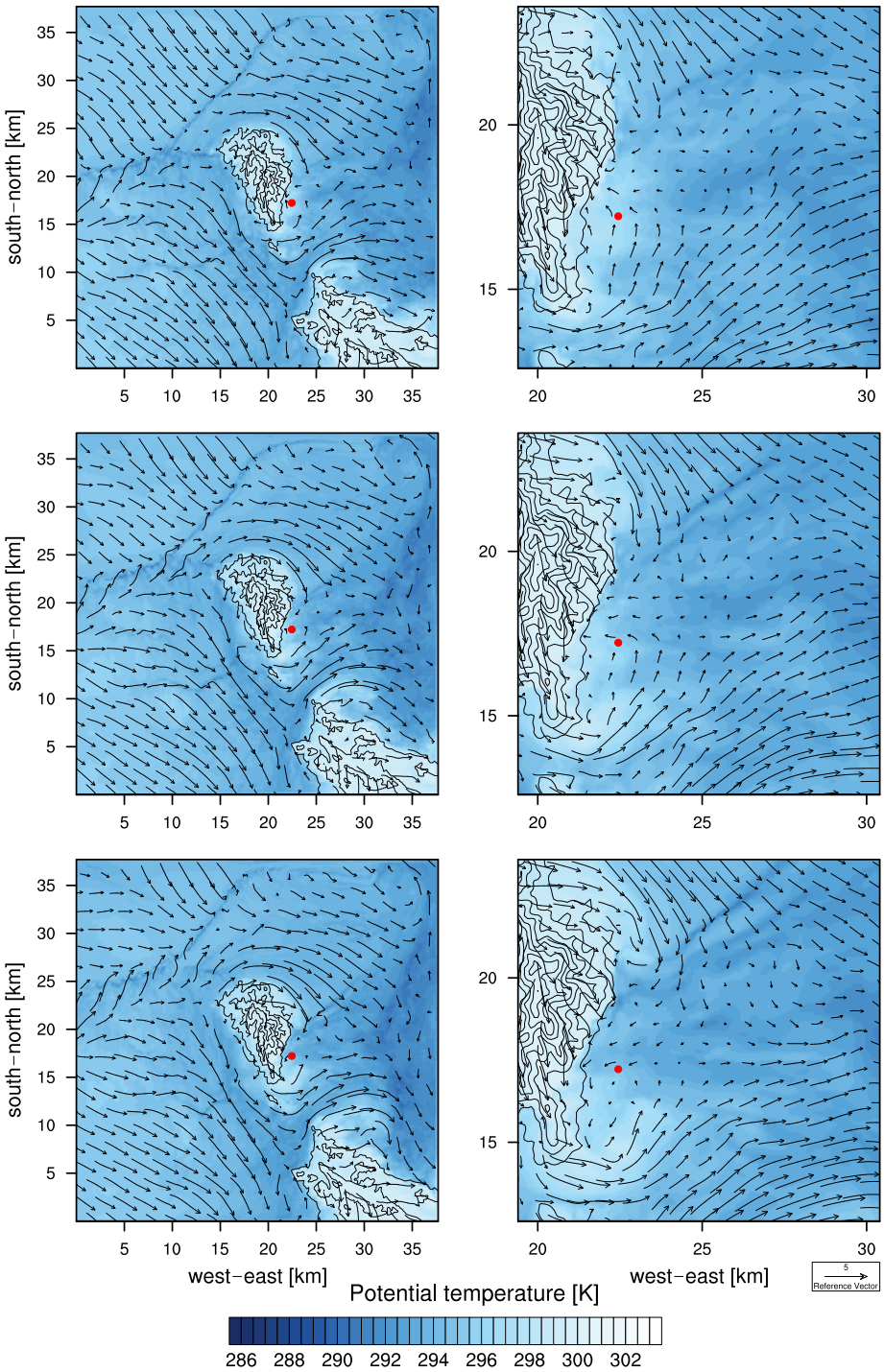

Figure 2.13: Contours of potential temperature and quiver plot of horizontal velocity at 28 m a.g.l. from 60%-NAM d03. Topography contour lines have (left) and 100 m (right) intervals, respectively. Left and right panels are taken from the same times; the left panel shows the full extent of d03, and the right panels is zoomed in around the east slope and east basin. Top panels at 0940 UTC. Middle panels at 0950 UTC. Bottom panels at 1000 UTC. Flow remains blocked, lee vortices with return flow correspond with a decrease in temperature on the east slope during the first model large temperature fluctuation discussed in the body text

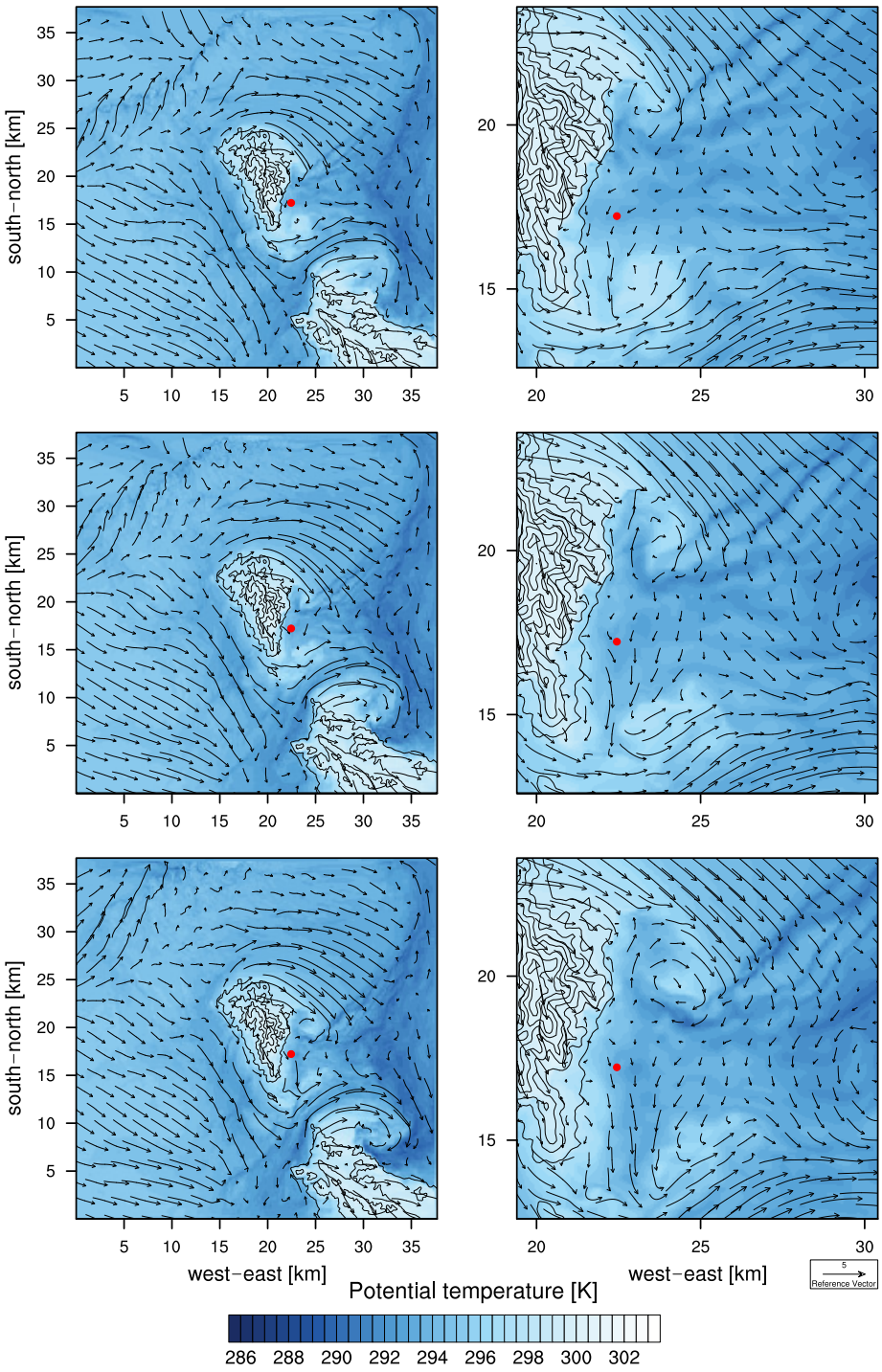

Figure 2.14: As in Fig. 2.13 but for 1010 UTC (top), 1020 UTC (middle), and 1030 UTC (bottom). Lee vortices are advected downstream, ceasing the decreasing in temperature on the east slope during the first model large temperature fluctuation discussed in the body text

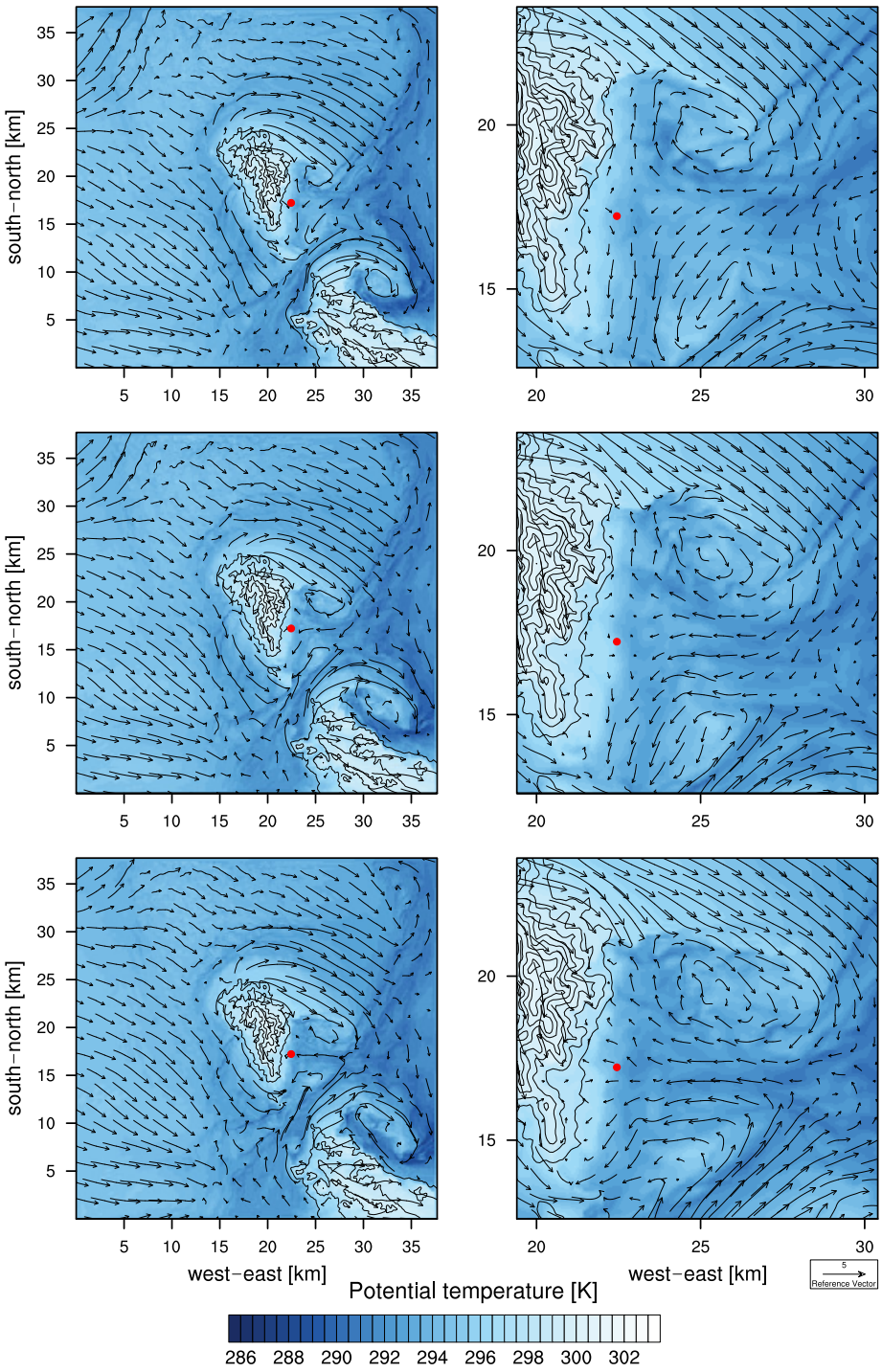

Figure 2.15: As in Fig. 2.13 but for 1040 UTC (top), 1050 UTC (middle), and 1100 UTC (bottom). Lee vortices grow as they are advected downstream, eventually return flow reaches the east slope initiating the second model large temperature fluctuation discussed in the body text

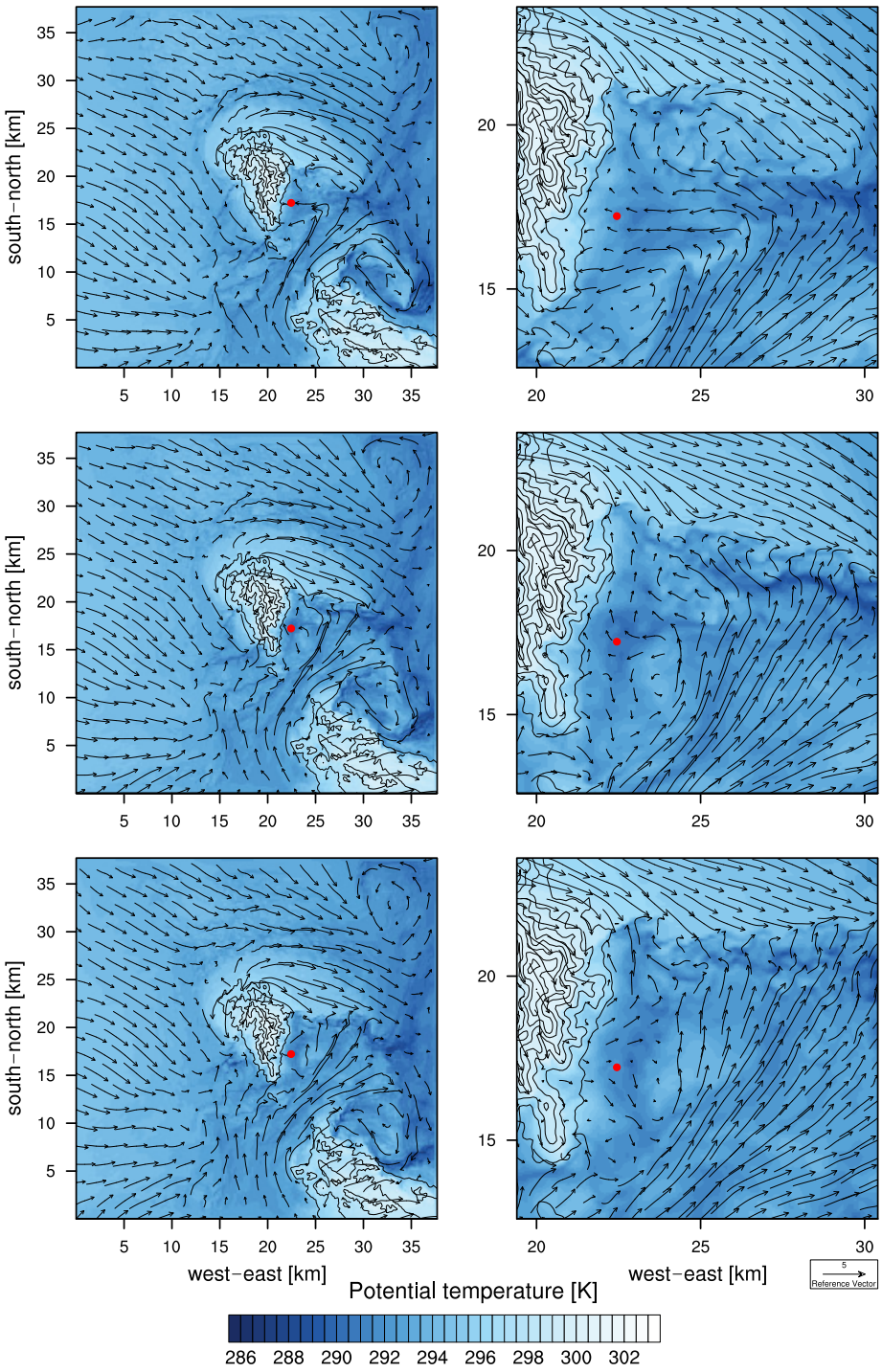

Figure 2.16: As in Fig. 2.13 but for 1110 UTC (top), 1120 UTC (middle), and 1130 UTC (bottom). Return flow continues temperature decrease on the east slope until a strong gap flow disrupts the lee vortex circulation, ending the second model large temperature fluctuation discussed in the body text

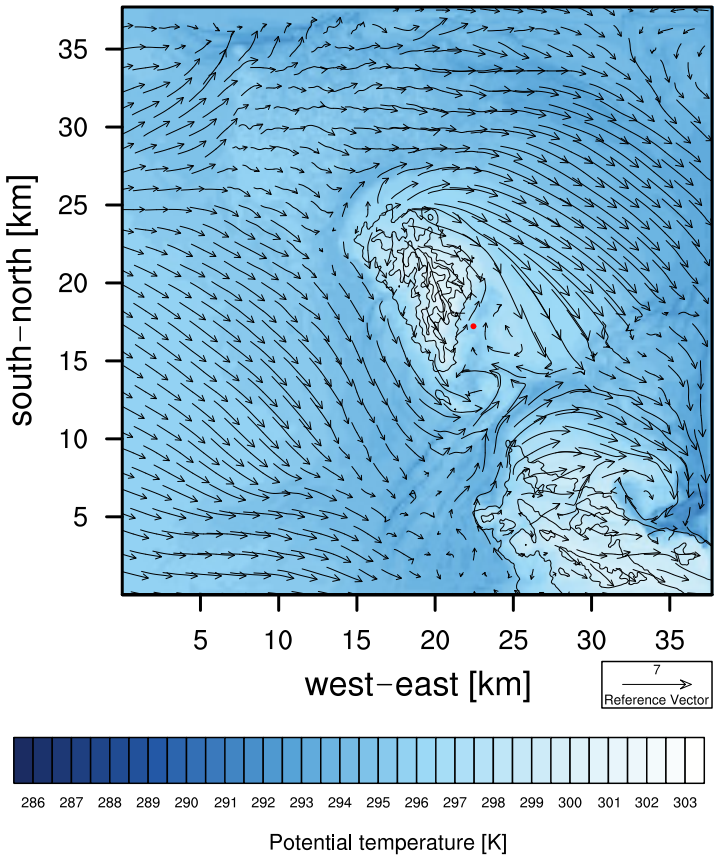

Figure 2.17: Contours of potential temperature and quiver plot of horizontal velocity at 28 m a.g.l. from Full-NAM d03. Taken at 1100 UTC (0500 MDT). Topography contour lines have 200-m intervals. Lee vortices dynamics are similar to the 60%-NAM d03 despite the lack of large temperature fluctuations. Two counter-rotating vertical axis circulations are visible near the east slope

on the lee slope.

Vortical Structure

Two counter-rotating vertical axis circulations develop on the lee side of Granite Peak in our real case large-eddy simulations. Though the baroclinicity generates horizontal vorticity, tilting of the horizontal vorticity in turn generates vertical vorticity whose spatial distribution can be compared to that of ideal simulations, e.g. those of Epifanio and Durran (2002a). In Fig. 2.18, we see the blocked northwesterly wind diverted around the northern lateral edge of Granite Peak flows into a region of negative (clockwise) vertical vorticity, while flow diverted around the southern edge leads to a region of positive vertical vorticity. The sign of vorticity matches that expected from idealized simulations, as seen in Fig. 1b in Epifanio

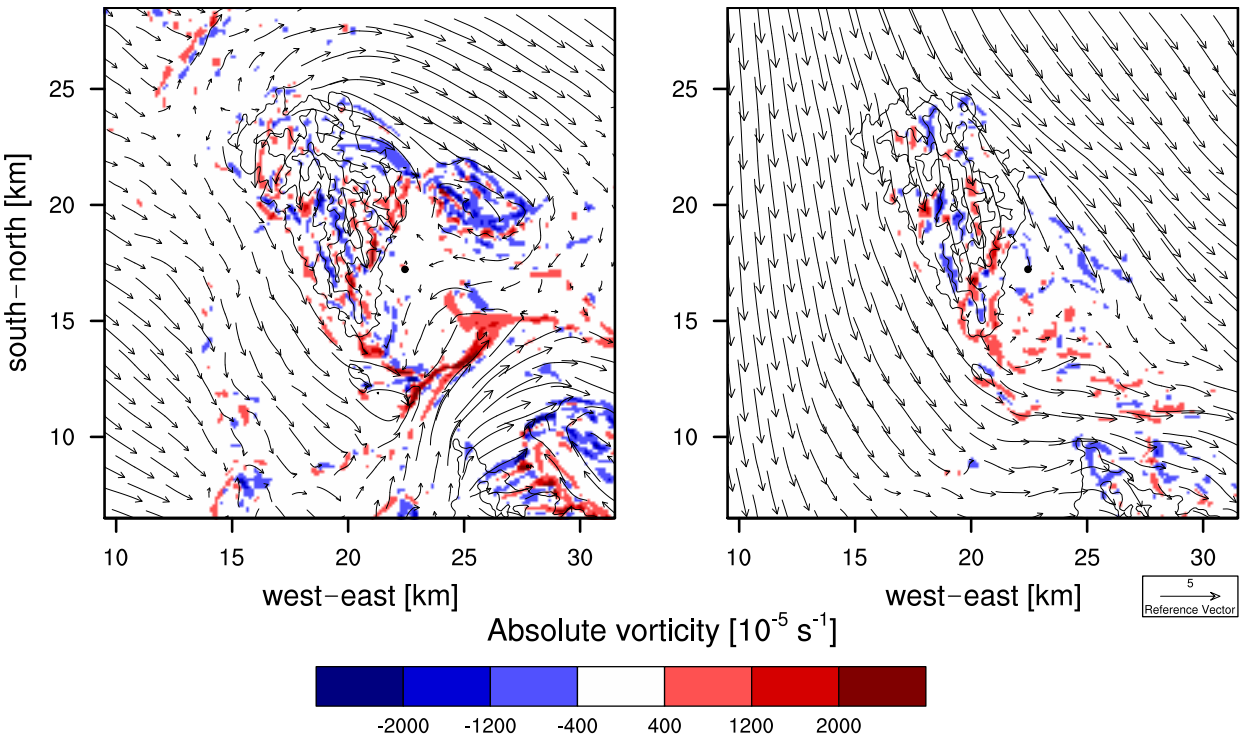

Figure 2.18: Vorticity contours at 1050 UTC (0450 MDT) from 60%-NAM d03. Left: First model level, 28 m a.g.l., with vorticity pattern of lee vortices that agrees qualitatively with those of Fig. 1b in Epifanio and Durran (2002b) from idealized simulations. Right: Third model level, 200 m a.g.l. Topography contour lines have 200-m intervals

and Durran (2002b). The vorticity pattern is stronger at the lowest model level, 28 m a.g.l. shown in the left panel, and extends approximately 200 m a.g.l. until it is nearly absent at the third model level shown in the right panel. Unlike idealized simulations of similar phenomena, vorticity is already present in the inflow but is also clearly enhanced on the lee side of Granite Peak. It is unclear how much of this enhancement is associated with further generation of vorticity by the baroclinic generation mechanism of Smolarkiewicz and Rotunno (1989), or with the interactions with the hydraulic-jump-like lee wave discussed by Schär and Smith (1993). An analysis following Epifanio and Durran (2002b) would be necessary to partition lee side vorticity among these mechanisms but is not conducted here. Rather, it suffices to demonstrate that the combination of these effects generates sufficient lee side vorticity to induce the reversed flow necessary for large temperature fluctuations to occur.

Contours of potential temperature from vertical cross-sections provide evidence for two of the proposed vorticity generation mechanisms, baroclinicity and finite-amplitude effects. In Fig. 2.4, a mountain lee wave is present through most of the night. Within a hydraulic-jump-like region of the lee wave, vertical vorticity is generated by the tilting and stretching

of vortex tubes. Some amount of this vorticity originates from the baroclinic generation mechanism. Baroclinicity on the lee slope is also evident in the potential temperature field. Far from the obstacle, isentropes are nearly horizontal but over the lee slope, they are tilted downward due to the potentially warmer descending flow. As such, there exists a significant horizontal component of the potential temperature gradient (Fig. 2.6). From hydrostatic balance, the pressure gradient is nearly vertical such that a horizontal ($-x$ direction in the $x-z$ planes plotted here) potential temperature gradient generates horizontal (directed into the page) vorticity baroclinically, as in the classic 'lock exchange' hydraulics problem.

Upstream Conditions

Though the orographic wakes presented here resemble those previously studied by analytical means or idealized simulations, e.g. those of Smolarkiewicz and Rotunno (1989), Schär and Durran (1997), and Epifanio and Rotunno (2005), there are important extensions and additional complications to consider in the real case LES of the current study. Beyond the complex shape of the terrain, nonuniform upstream conditions pose such a challenge. As mentioned previously, the presence of vorticity upstream of Granite Peak is one deviation from the ideal inflow conditions. Similarly, the inflow is nonuniform for wind speed, wind direction and buoyancy frequency.

From the profile of model wind direction in Fig. 2.7 or by comparing the vector plots in Fig. 2.5, we see the low-level free stream flow is west–north–westerly while flow farther aloft is north–north–westerly. In this case, the directional shear has the same sign as expected from an Ekman spiral, a common feature of stably stratified boundary layers in rotating reference frames. Further study would benefit from revisiting the idealized simulations while imposing directionally sheared inflow to better identify the impact of such nonuniform velocity profiles.

Similar to the wind conditions in the real case models, the background stratification is neither uniform nor steady as it is in idealized models. Rather, potential temperature has a more realistic profile in which stratification is stronger near the cold ground. Epifanio and Rotunno (2005) used a two layer background stratification profile with this feature, but within each layer the simplification to constant stratification is still applied. In that study, the characteristic buoyancy frequency used in the non-dimensional mountain height is that of the lower and more strongly stratified layer; we follow this approach below.

Non-dimensional Parameter Space

As a practical matter, the heterogeneity of buoyancy frequency, N, and of wind speed, U, preclude an unambiguous definition of non-dimensional mountain height, $\epsilon = Nh/U$. Nonetheless, ad hoc methods can be developed to calculate ϵ with bulk lapse rates and average velocities. Using the first five grid levels to compute a characteristic buoyancy frequency, and the first 10 grid levels for a characteristic velocity scale, we calculate ϵ at a point north–east of Granite Peak chosen a posteriori on the basis of the vector plots. The peak height at Granite Peak is 840 m above the valley floor (Fernando et al. 2015). We

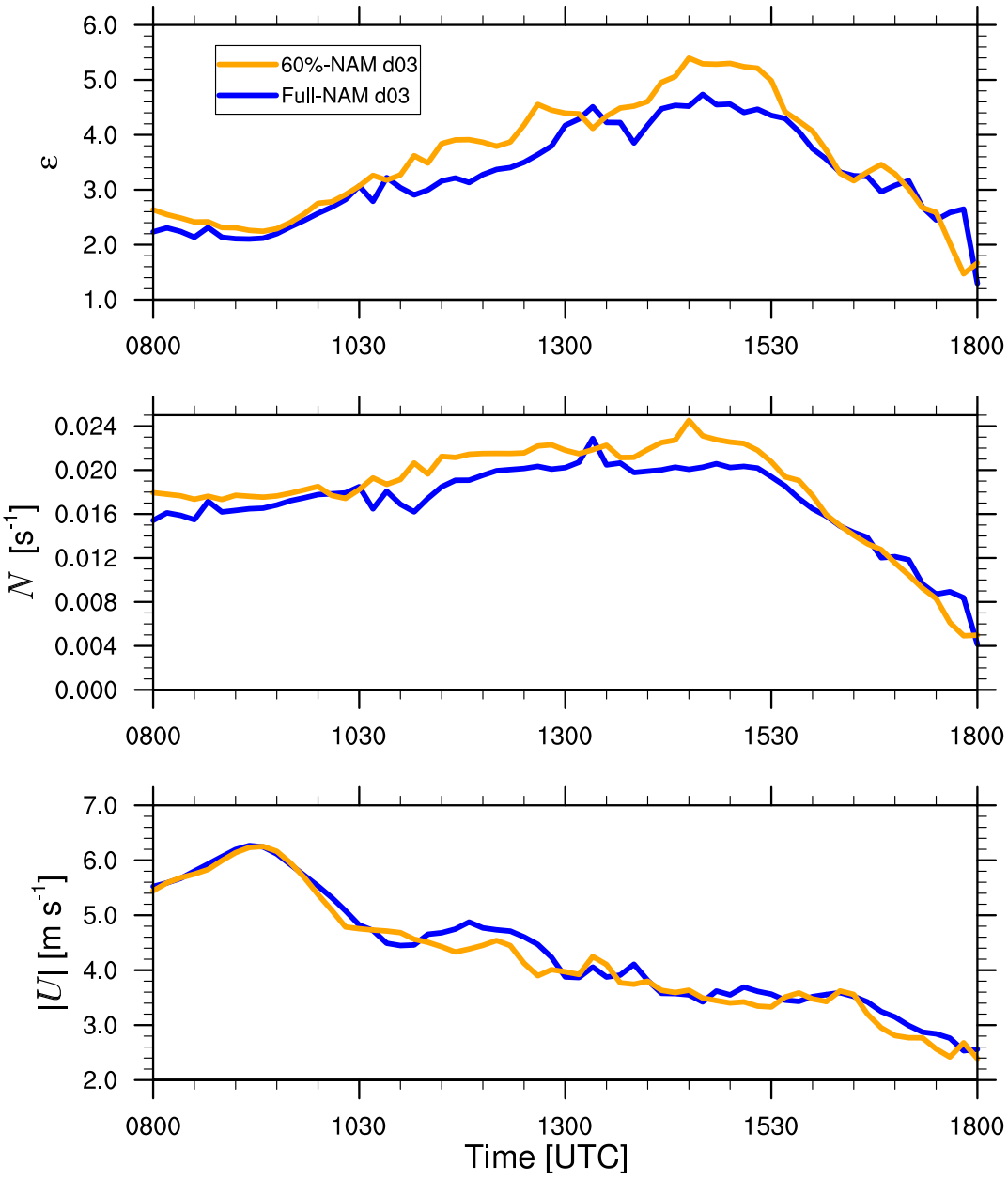

Figure 2.19: Time series of non-dimensional mountain height, $\epsilon = Nh/U$ (top), computed with mountain height, h, taken as 800 m; buoyancy frequency, N (middle), taken as average over first five grid levels; and wind speed, $|U|$ (bottom), taken as average over first 10 grid levels at 40°12.5' N, 113°22.5' W in the LES forced by NAM with full or 60% soil moisture initialization

use a rounded $h = 800$ m to calculate non-dimensional mountain height plotted in the top panel of Fig. 2.19. The variability of ϵ is decomposed into N and U, shown in the other panels. Though buoyancy frequency is generally increasing throughout the night, most of the increase in ϵ is due to a decrease in wind speed during this time. Soon after sunrise (1340 UTC), non-dimensional mountain height begins to rapidly decrease despite low wind speeds. At this time, changes in ϵ are dominated by the decrease of N as the nocturnal boundary layer is broken up.

Together with the horizontal aspect ratio, the non-dimensional mountain height determines the regime of orographic wake formation in the idealized problem. The time series of ϵ in Fig. 2.19 reveals an average value of approximately 3 throughout the period of lee vortex formation in 60%-NAM d03. Though Granite Peak is elongated in the longitudinal direction, consideration of the skewed angle of approach of the low-level impinging flow justifies taking $\beta \approx 1$, i.e. the cross-stream and along-stream dimensions of the obstacle are approximately equal. These values of β and ϵ lie within the regime of blocked flow and baroclinic generation of lee vortices in the parameter space of the idealized problem (see Epifanio 2003 for a schematic of this parameter space). That is, ϵ is not so large that boundary layer separation, rather than baroclinicity, is likely to dominate the wake dynamics as it might for $\epsilon \gtrsim 10$ (Epifanio 2003). This suggests that the same non-dimensional parameters may prove valuable in the analysis of real case lee vortex dynamics and in the ultimate parametrization of these orographic wakes in large scale models. Though a large enough non-dimensional mountain height seems a necessary condition for lee vortex formation, it is not sufficient. Lack of lee vortices in the later half of the early morning is due to a strong gap flow to the south of Granite Peak that interferes with dynamics of the orographic wake in 60%-NAM d03.

In the full soil moisture simulations, values for non-dimensional mountain height also lie within the lee vortex regime of the β–ϵ parameter space and we see lee vortices develop (Fig. 2.17). Though there is a return flow in the wake, there are no large temperature fluctuations at the location of the east slope stations in the full soil moisture LES (Fig. 2.9). This lack of large temperature fluctuations in the full soil moisture simulation is explained by the east basin warm bias that is much worse in the full soil moisture simulations (Fig. 2.8). Only when both a cold-air pool that is sufficiently cold and lee vortices are present, as in 60%-NAM d03, do large temperature fluctuations occur.

2.6 Summary and Conclusions

Nested large-eddy simulations using the WRF model are shown here to be able to recreate the unique large temperature fluctuations observed on the east slope of Granite Peak during IOP 6 of the MATERHORN field campaign. The LES results and analysis presented are able to explain the topography-induced lee vortices that generate these temperature fluctuations in concert with displacement of the east basin cold pool. This success required careful attention to surface conditions and numerical parameters such as grid spacing and timestep

considerations over steep terrain. The ubiquity of these temperature fluctuations, occurring on all quiescent nights of the MATERHORN's autumn campaign, suggests that these constitute a significant source of mesoscale model error. Temperature-sensitive operations located on sloped terrain, e.g. fire weather prediction, could therefore benefit from the utilization of large-eddy simulations to supplement and extend traditional forecast products.

Along the eastern slope of Granite Peak, the large temperature fluctuations are associated with the displacement of a cold-air pool that forms in the nearby basin. The warm bias of the model cold-air pool is greatly improved by drying the shallowest layer and thus increasing in situ cooling. Numerical stability constraints limit the vertical grid spacing allowed with the fine horizontal (100 m) resolution used here and the associated steep terrain slopes, which affects the model's ability to resolve drainage flows. Without this dynamical cooling from drainage flows, a warm bias remains in the east basin and diminishes the temperature decrease on the slope when the cold-air pool is displaced upslope. Future studies may avoid this source of error by using a vertical grid that is not terrain-following, such as the immersed-boundary method (Lundquist et al. 2012; Arthur et al. 2018; Bao et al. 2018; Wiersema et al. 2018), to enable better representation of flow near the terrain surface.

A new stability limit was also proposed here to enable simulations over steep terrain: reducing the constant of proportionality between timestep and grid spacing by a factor of $b \approx 3$ in the current work or, more generally, $1 \leq b \lesssim 5$ (Poulos 1996; Zhong and Chow 2013). Future studies that continue to use terrain-following coordinate systems over steep slopes should consider this new stability limit as a guideline in selecting numerical simulation parameters.

We have shown that the cold-air pool displacement is associated with the return flow of the lee vortices, as postulated by Jeglum et al. (2017) and shown in their WRF model simulations for another date. These lee vortices occur in the real case simulation within a non-dimensional parameter regime which agrees well with the regime in which lee vortices are expected to form in idealized simulations, such as those of Smolarkiewicz and Rotunno (1989) and Epifanio and Rotunno (2005). However, due to the interference of other flow phenomena like gap flows, large non-dimensional mountain height is not a sufficient condition to predict the occurrence of lee vortices. As such, the parametrization of lee vortices for mesoscale and larger scale models cannot be completed without simultaneously addressing a wider range of interactions between stable flows and complex terrain.

Chapter 3

Efficacy of the cell perturbation method in large-eddy simulations of boundary layer flow over complex terrain

The following chapter is a reproduction, with slight modification, of Connolly, A., L. van Veen, J. Neher, B. Geurts, J. Mirocha, and F. K. Chow, submitted: Efficacy of the cell perturbation method in large-eddy simulations of boundary layer flow over complex terrain. *Atmosphere*, –.

Original Abstract: A challenge to simulating turbulent flow in multiscale atmospheric applications is the efficient generation of resolved turbulence motions over an area of interest. One approach is to apply small perturbations to flow variables near the inflow planes of turbulence-resolving simulation domains nested within larger mesoscale domains. While this approach has been examined in numerous idealized and simple terrain cases, its efficacy in complex terrain environments has not yet been fully explored. Here, we examine the benefits of the stochastic cell perturbation method (CPM) over real complex terrain using data from the 2017 Perdigão field campaign, conducted in an approximately 2-km wide valley situated between two nearly parallel ridges. Following a typical configuration for multiscale simulation using nested domains within the Weather Research and Forecasting (WRF) model to downscale from the mesoscale to a large-eddy simulation (LES), we apply the CPM on a domain with horizontal grid spacing of 150 m. At this resolution, spurious coherent structures are often observed under unstable atmospheric conditions with moderate mean wind speeds. Results from such an intermediate resolution grid are often nested down for finer, more detailed LES, where these spurious structures adversely affect the development of turbulence on the subsequent finer grid nest. We therefore examine the impacts of the CPM on the representation of turbulence within the nested LES domain under moderate mean flow conditions in three different stability regimes: weakly convective, strongly convective, and weakly stable. In addition, two different resolutions of the underlying terrain are used to explore the role of the complex topography itself in generating turbulent structures. We demonstrate that the CPM improves the representation of turbulence within the LES domain, relative to the use of high-resolution complex terrain alone. During the convective conditions, the CPM improves the rate at which smaller-scales of turbulence form, while also accelerating the attenuation of the spurious numerically-generated roll structures near the inflow boundary. During stable conditions, the coarse mesh spacing of the intermediate LES domain used herein was insufficient to maintain resolved turbulence using CPM as the flow develops downstream, highlighting the need for yet higher resolution under even weakly stable conditions, and the importance of accurate representation of flow on intermediate LES grids.

3.1 Introduction

Over the past several decades, computational power has grown such that it is now becoming routine to perform multiscale atmospheric simulations, in which a larger-scale mesoscale flow field is dynamically downscaled using grid nesting, with finer mesh spacing over regions of interest. Such nesting can be pursued successively to large-eddy simulation (LES) scales, within which the energetically important scales of boundary-layer turbulence are explicitly

resolved. Near the inflow boundaries of nested large-eddy permitting domains, however, finer-scale turbulence is lacking because it is not explicitly captured in the coarser bounding domain simulation. The development of turbulence in the nested simulation often requires a long distance from the lateral boundaries, referred to as fetch. Goodfriend et al. (2014), in a computational fluid dynamics code, and Mirocha et al. (2013), using a numerical weather prediction (NWP) model, explored the transition distance required for turbulence to be generated at a coarse-to-fine grid interface. Both studies found that it takes significant fetch to sufficiently develop turbulence compared to stand-alone periodic simulations at the finer resolution, and that this fetch depends on the chosen turbulence closure model. One way to address this issue is to require very large domain sizes so that there is sufficient distance from the lateral boundary to the region of interest in the flow. This of course results in significantly increased computational costs, considering that up to 75% of the domain can be lost to spurious flow structures according to Mirocha et al. (2013).

A recent approach to address this issue is the cell perturbation method (CPM) of Muñoz-Esparza et al. (2014), Muñoz-Esparza et al. (2015); Muñoz-Esparza and Kosović (2018). The CPM adds small amplitude, $\mathcal{O}(1\text{ K})$, perturbations to the temperature field along inflow boundaries to trigger the rapid development of turbulence on the finer nested grid. The CPM has been tested primarily with idealized domains and over flat terrain and found to be successful in greatly reducing the fetch required to develop finer structures, which can develop in as few as 25 points farther into the domain from the perturbation region (Muñoz-Esparza et al. 2014). This reduces computational cost by reducing the required domain size to develop turbulence on the finer, more expensive grids. Further, the CPM is easy to implement and does not require additional cost due to larger domains or from running a priori simulations as in other turbulence generating methods (Keating et al. 2004).

An outstanding question for multiscale simulation over complex terrain is whether the topography itself suffices to generate finer scale turbulence in the nested domains, or whether additional turbulence generating techniques are effective. In some applications over complex terrain, a main improvement with nesting to high resolutions is that topography-driven flows such as gap flows can be resolved (Wood 2000; Fernando et al. 2015). In many cases, however, it has been found that increasing the grid resolution by nesting does not lead to improved results (Marjanovic et al. 2014). Instead, the large flow features from the outer domain carry over into the inner domain, and detailed examination of the flow shows lack of the expected finer scale flow structures on the inner domain. This can be due to insufficient detail in the forcing provided by topography and land cover data (Chow et al. 2006), but also an insufficient fetch for finer-scale turbulence to develop may be a likely cause. A typical pattern observed is "streaky" roll structures in the wind field (Mirocha et al. 2014; Muñoz-Esparza et al. 2014; Rai et al. 2017) or spurious large-scale convection cells which persist on the inner domain (Zhou et al. 2014; Ching et al. 2014). Mirocha et al. (2013); Ching et al. (2014) found that prohibitively large fetches were required for turbulence to develop in an LES nested in a mesoscale simulation performed by the Weather Research and Forecasting (WRF) model. The development of turbulence was aided by the application of convective forcing or by adding idealized, sinusoidal topography. Nonetheless, 100s or 1000s

of points, depending on the details of the turbulence parameterization, were required for proper turbulent scales to develop. As seen by Mirocha et al. (2013); Muñoz-Esparza et al. (2014, 2015), in some cases it can take up to three-quarters of the inner domain length before finer structures develop. If the inner nest is too small, then it is possible for almost no finer structures to develop, and the benefit of the finer resolution may largely be lost. Warner et al. (1997) more than 20 years ago discussed the need to place nested domain boundaries far from the region of interest to minimize spurious influence from the grid nesting boundaries. Now that LES nested within NWP is becoming more commonplace, a new focus on the representation of turbulent motions on the inner grids is warranted.

The detailed turbulent motions at the microscale are of particular interest in applications such as wind energy. Prediction of power generation, blade fatigue, and turbine wake interactions depends critically on the representation of turbulence (Ayotte 2008). Wind energy forecasting over complex terrain was a primary focus of the Perdigão field campaign which took place in Portugal in 2017 (Fernando et al. 2019). Nested large-eddy simulations performed for the Perdigão experiment also develop unphysical streaky structures despite the complex topography present, as shown later below. At the high computational costs required for LES, it is paramount to develop realistic turbulence as fast as possible in the inner domains.

This work focuses on the benefits of CPM to reduce the large fetch required to generate finer turbulent motions on nested domains over complex terrain. The Perdigão field site is used as a test case. CPM has previously been tested in real case simulations of two wind farms over relatively flat terrain by Muñoz-Esparza et al. (2017); Arthur et al. (2020). Based on spectra of vertical velocity, Muñoz-Esparza et al. (2017) showed unperturbed LES, $\Delta =$ 90 m, took 45 km of fetch to sufficiently develop turbulence, while applying perturbations reduced this to 9 km. Arthur et al. (2020) found marginal benefits on mean flow fields from using CPM, however the structure of the turbulence was certainly enhanced with much finer scales as seen in velocity contours. Arthur et al. (2020) applied CPM between domains with 250 m grid spacing and 50 m grid spacing, and again between the 50 m grid and a final nest with 10 m grid spacing. However, this fine LES was intentionally designed with 300 grid points of fetch before the model performance versus field observations was evaluated, making the additional effects of CPM difficult to extract. Their analysis focused on near-neutral and slightly unstable conditions at a field site with terrain smoothly varying by roughly 40 m in elevation over 5 km.

Here, we focus on the Perdigão field site which consists of two approximately parallel ridges and complex hilly terrain. There is a single wind turbine on one of the ridges, and one of the overall goals of the project is to provide data to improve simulation capabilities, including the generation of accurate turbulent structures as well as the impacts of terrain and atmospheric stability on wake behavior in complex terrain (Fernando et al. 2019). In this paper, we prioritize testing a grid nesting framework to consistently and efficiently generate appropriate turbulent motions on the finer grids. The CPM is used to trigger turbulence on a 150-m resolution LES domain, nested within a 2250-m resolution mesoscale domain. Other work is pursuing finer nests to 50 m and 10 m resolutions (Chow et al. 2018; Wise et al.

2020), but our focus here is on the 150 m domain where spurious numerically-generated rolls are apparent and the model struggles to develop finer structures.

The goal of this work is to study the effect of the CPM on the resolved turbulence when combined with the effects of complex topography. The previous real case studies that have performed LES with CPM have used fine meshes and large domains, which require significant computational costs (Muñoz-Esparza et al. 2017; Arthur et al. 2020). Other studies have considered turbulence in 'coarse' LES over complex terrain but without CPM (Rai et al. 2017; Wagner et al. 2019). We will examine the relative impacts of topography and the CPM in multiscale WRF simulations using observations from Perdigão. Both mean flow and turbulence characteristics will be examined using the CPM relative to two different resolutions of the underlying terrain to examine impacts of terrain steepness and smaller-scale variabilty. The model results are compared to field observations from the Perdigão field campaign (Section 3.4). We then analyze the performance of the CPM by comparing different domain sizes (fetches) and turbulence energy spectra (Sections 3.4-3.4). We discuss the computational savings made possible by the CPM, as well as the sensitivity of these results to the time of day and to the resolution of model topography. The CPM is successful at reducing fetch and is especially cost-saving during the weakly convective period during which unperturbed simulations require the longest fetch to fully develop turbulence.

3.2 Background

Several methods have been proposed to address challenges faced by grid nesting and the related generation of appropriate turbulent length scales. These range from turbulence recycling methods (Lund et al. 1998), which artificially increase the fetch by 'recycling' information on the turbulence within the domain to its inflow boundary, to the purely stochastic methods, which instigate turbulence through perturbations not based on fundamental physical equations (Tabor and Baba-Ahmadi 2010). Other techniques, the prepared methods, use a priori simulations with periodic boundary conditions to then augment the inflow of the nested simulations so that physically generated turbulence is present at the boundary (Keating et al. 2004). However, performing a priori simulation also has a computational cost that could negate the gains of the turbulence generation method. Using engineering fluid mechanics codes, the wind energy community has long employed many of these methods for synthetic turbulence generation (Kleinhans et al. 2009). Due to the complexity of meteorological models, not all techniques are readily portable to NWP codes. For example, the existence of multiple inflow boundaries makes it unclear how to generalize recycling methods. Further, the a priori simulations used in prepared methods generally require periodic boundary conditions. In addition to issues of induced periodicity, periodic boundary conditions could not be used for nested simulations which must be forced by their parent at the boundary.

Given these issues with recycling and prepared methods, Mirocha et al. (2014) provide an initial formulation of a potential turbulence generation method suitable for NWP ap-

plications by applying stochastic perturbations to all the horizontal velocity and potential temperature fields. Muñoz-Esparza et al. (2014) improved this initial perturbation technique by applying stochastically generated perturbations to only the potential temperature field over a series of small cells, with discontinuities at the cell boundaries, and generalized the approach via a series of sensitivity studies over a range of wind speeds (Muñoz-Esparza et al. 2015), and later stability regimes (Muñoz-Esparza et al. 2017; Muñoz-Esparza and Kosović 2018). Accelerating the development of turbulence in this fashion has shown great efficacy in numerous applications.

Muñoz-Esparza et al. (2014) compare the CPM to other stochastic perturbation methods, some requiring a priori simulation, by perturbing only the potential temperature field. Because synthetic turbulence based on momentum perturbation can violate the governing equations, perturbing only the potential temperature is the preferred practice. They find CPM develops realistic turbulence over comparable or fewer points of fetch than the other methods, while retaining a level of simplicity for ease of implementation.

Muñoz-Esparza et al. (2015) extend the CPM approach by proposing that the magnitude of potential temperature perturbations for neutral flows be based upon the perturbation Eckert number and the perturbation time scale. This formulation for perturbation magnitude was later modified for stable conditions by Muñoz-Esparza and Kosović (2018), suggesting a Richardson number approach instead that improved performance during stable conditions. Here, we do not include the stability correction and instead utilize the formulation of Muñoz-Esparza et al. (2015) to investigate whether it suffices for the weak stability conditions that are the focus of this paper.

3.3 Methods

Cell perturbation method

Following Muñoz-Esparza et al. (2015), pseudorandom perturbations are applied to the potential temperature field near the inflow boundaries over "cells" of 8×8 grid points in the horizontal plane. Three such cells, for a total width of 24 grid points parallel to the inflow boundaries, are applied at each vertical level from the first vertical level up to a height of $0.9z_i$, where z_i is the planetary boundary layer height provided by the mesoscale parent simulation. The maximum height at which perturbations are applied is increased from $\frac{2}{3}z_i$ used by Muñoz-Esparza et al. (2014, 2015) in case of shallow boundary layers.

The perturbation temperature, $\tilde{\theta}_\mathrm{p}$, is drawn from a uniform distribution in the range $[-\tilde{\theta}_\mathrm{pm}, \tilde{\theta}_\mathrm{pm}]$. Figure 3.1 illustrates these perturbations for an example domain. We follow Muñoz-Esparza et al. (2015) who suggest that the range of the uniform distribution be determined from a perturbation Eckert number:

$$Ec = \frac{U_g^2}{c_p \tilde{\theta}_\mathrm{pm}} \tag{3.1}$$

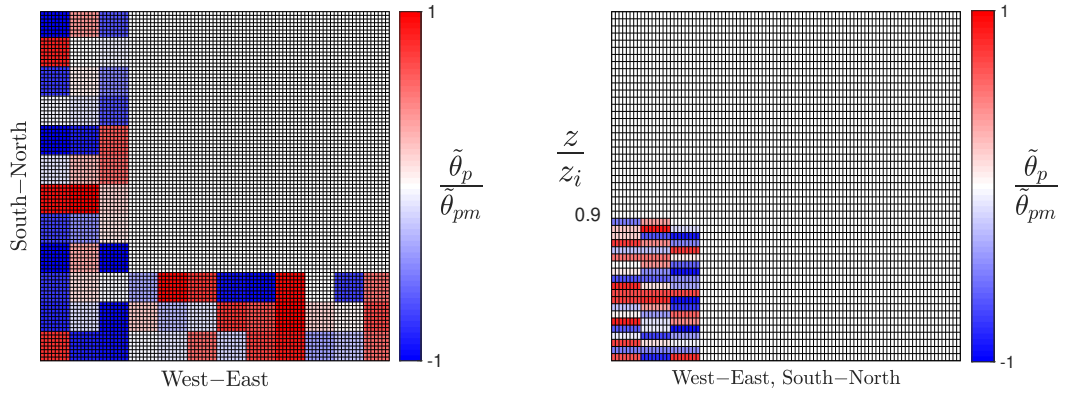

(a) (b)

Figure 3.1: Example slices illustrating potential temperature perturbations applied (a) for southern and western inflow boundaries in the manner of the cell perturbation method as a horizontal cross section and (b) a vertical cross section with inflow from the left boundary. The potential temperature perturbation, θ_p, is drawn from a uniform distribution centered at zero with θ_{pm} as the maximum possible magnitude, applied from the first vertical level to a height of 0.9 times the boundary layer height, and using the same perturbation for a 8×8 grid point 'cell' with 3 such cells, 24 grid points, along each lateral boundary.

where U_g is the geostrophic wind, computed as the average wind speed at $1.1z_i$, and c_p =1004.6 J kg^{-1} K^{-1} is the specific heat capacity of air taken as a constant. Muñoz-Esparza et al. (2015) determined an optimal Eckert number, $Ec = 0.2$, such that

$$\tilde{\theta}_{\mathrm{pm}} = \frac{U_g^2}{0.2c_p}. \tag{3.2}$$

Another non-dimensional parameter is used to determine the frequency with which new perturbations should be applied to the boundary, the perturbation time scale:

$$\Gamma = \frac{t_p U_w}{d_c} \tag{3.3}$$

where t_p is the perturbation time period, U_w is representative of the weakest winds at the inflow boundary, and d_c represents a length scale over which the perturbation should be advected before new perturbations are applied. Muñoz-Esparza et al. (2015) suggest values of $\Gamma \approx 1$ so that perturbations are not either missing for long periods of time, in the case of $\Gamma \gg 1$, nor rapidly superposed, in the case of $\Gamma \ll 1$. In this study, the CPM uses a value of $\Gamma = 0.75$ favoring a slightly more rapid refresh of the perturbations. Additionally, U_w is calculated as the average inflow wind speed at the second vertical level, moved up from the first vertical level in Muñoz-Esparza et al. (2015) in case of low near surface wind speeds over complex terrain. The length scale is computed as

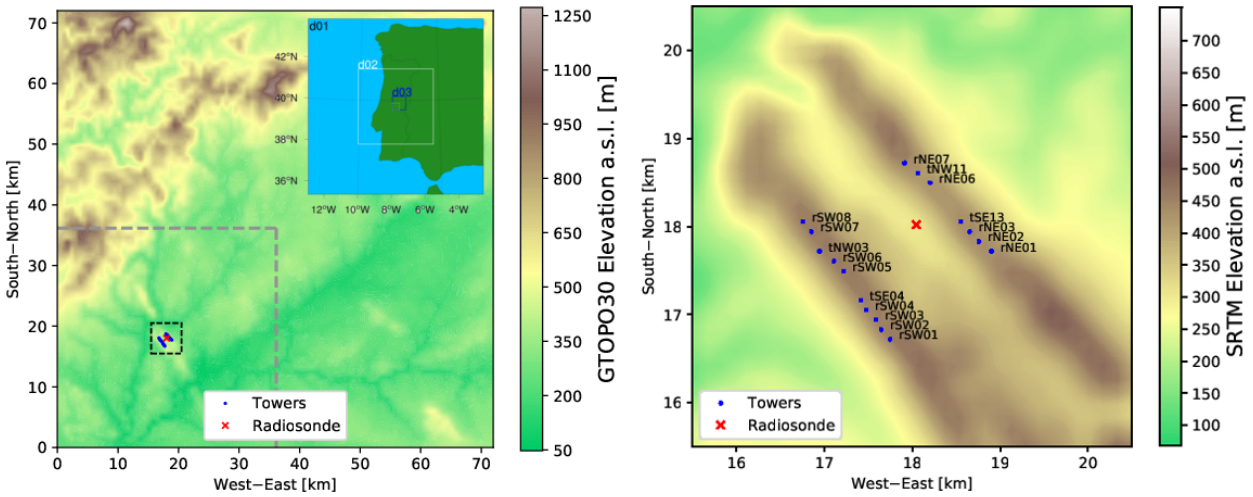

Figure 3.2: Left: Contours of 30 arcsec resolution, GTOPO30, topography used in d03_30s, d03_30s_cpm, and d03_30s_ref (Table 3.1) over the larger d03_30s_ref domain. Dashed gray lines demarcate the locations of the boundaries of the smaller LES. Left, inset: Nested WRF domains, d02 and d03, shown in the area covered by d01, the outermost parent domain including much of the Iberian Peninsula and the surrounding water. Right: Vale do Cabrão and field stations used to validate the coarse LES. Contours of 3 arcsec resolution, SRTM topography used for d03_3s and d03_3s_cpm (see Table 3.1) zoomed in on a subregion of those domains marked by the dashed black line in the left panel.

$$d_c = \frac{24\Delta x}{\cos\hat{\phi}} \tag{3.4}$$

where $\hat{\phi}$ is the average angle of the wind relative to the inward normal of the inflow boundary. As such, d_c is equal to the width of the perturbation area when flow is normal to the inflow boundary, but d_c becomes larger for skewed angles of approach. Note, a boundary is considered an inflow boundary if it has net inflow at $1.1z_i$, when averaging across the entire boundary. That is, perturbations are not applied at every instance where inflow occurs over the whole domain but are only applied along the full length of inflow boundaries. For example, if the primary flow direction is from the south-west, then the southern and western boundaries will include perturbations along the entire length of the boundaries (Figure 3.1).

Numerical Simulation Setup

The current simulations use the Weather Research and Forecasting (WRF) model version 3.9.1.1 (Skamarock et al. 2008) developed by the National Center for Atmospheric Research (NCAR). The WRF model allows multiscale modeling through its nesting capabilities, so that we can generate various microscale LES configurations nested in the same mesoscale parent models. The first two domains, d01 and d02, are mesoscale simulations performed at

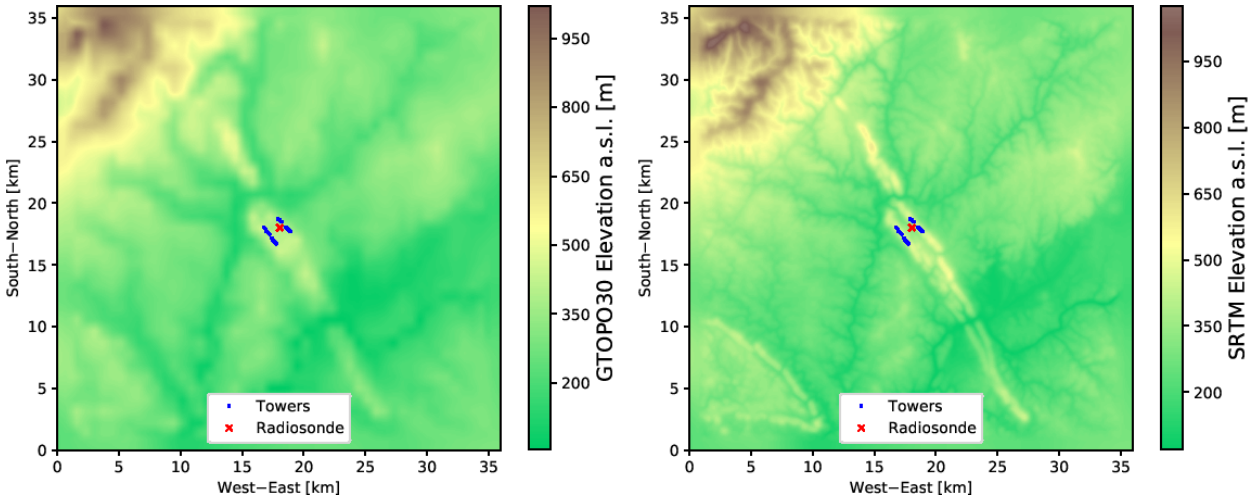

Figure 3.3: Left: Model topography used in d03_30s and d03_30s_cpm from the 30 arcsec resolution GTOPO30. Right: Model topography used in d03_3s and d03_3s_cpm from the 3 arcsec resolution SRTM.

Table 3.1: Information on nested simulation domains include simulation name, horizontal grid spacing, number of grid points, time step, turbulence closure method, resolution of topography, and use of CPM. All domains use the same vertical grid spacing, stretching from 21 m near the bottom surface to 170 m at 2 km a.s.l., and up to 400 m aloft, selected to closely follow the levels used by the ECMWF forcing data below 5000 Pa.

Domain	$\Delta x, \Delta y$	Nx·Ny·Nz	dt [s]	Closure	Topography Resolution	CPM
d01	6.75 km	141·141·89	30	MYNN	2 arcmin	off
d02	2.25 km	181·181·89	10	MYNN	30 arcsec	off
d03_30s	150 m	241·241·89	0.5	TKE 1.5	30 arcsec	off
d03_30s_cpm	150 m	241·241·89	0.5	TKE 1.5	30 arcsec	on
d03_30s_ref	150 m	481·481·89	0.5	TKE 1.5	30 arcsec	off
d03_3s	150 m	241·241·89	0.5	TKE 1.5	3 arcsec	off
d03_3s_cpm	150 m	241·241·89	0.5	TKE 1.5	3 arcsec	on

6.75 km and 2.25 km, respectively. The microscale simulations, with the prefix d03 used for various configurations, are run at a resolution of 150 m and use an LES turbulence closure (Deardorff 1980; Wyngaard 2004). A relatively large grid nest ratio of 15:1 (2250 m:150 m), is used between d02 and d03 because a smaller nest ratio would result in grid spacing within the turbulent gray zone, in which it is unclear whether a PBL scheme or LES turbulence closure should be used (Wyngaard 2004). It should be noted that a more traditional nest ratio of 3:1 also produced streaky structures in previous work from Mirocha et al. (2014) and Zhou et al. (2014). Further details for each domain are given in Table 3.1, and Figure 3.2 illustrates the nest locations. The CPM is applied only at the boundary of the microscale simulations, where they receive inflow information from d02, the parent domain. These simulations are labeled with the suffix _cpm.

The dynamic core of the WRF model is based on a third order Runge–Kutta time advancement scheme, with split time stepping to handle acoustic modes, as well as fifth-order horizontal advection and third-order vertical advection. Physical parameterizations employed in the current simulations include the Noah land surface model (Chen and Dudhia 2001), the Rapid Radiative Transfer Model for longwave radiation (Mlawer et al. 1997), the Dudhia shortwave radiation model (Dudhia 1989), and the WRF Single-Moment 5-class microphysics scheme (Hong et al. 2004). All domains use a Mellor-Yamada level-3 surface layer parameterization. The mesoscale simulations, d01 and d02, also use the PBL scheme designed to be coupled with this surface layer model (Nakanishi and Niino 2006), while d03 uses a TKE 1.5 LES turbulence closure (Deardorff 1980).

Of the land cover data provided by NCAR for use with WRF, the finest available resolution is 30 arcsec, about 1 km at middle latitudes, from the United States Geological Survey (USGS). Our simulations also incorporate a higher resolution, 100 m, land cover data set, the Coordination of Information on the Environment (CORINE), which is then transformed into USGS land use types (Bossard et al. 2000; Pineda et al. 2004).

Topography data is made available at resolutions no higher than 30 arcsec with the standard WRF download. This Global 30 Arc-Second Elevation (GTOPO30) product is used for d03_30s, d03_30s_cpm, and d03_30s_ref. As the LES domain is more finely resolved than GTOPO30 topography, finer resolved topography data can be ingested. Two other LES cases, d03_3s and d03_3s_cpm, ingest 3 arcsec ($\approx$ 90 m) topography from the Shuttle Radar Topography Mission (SRTM) (Farr et al. 2007), to test the sensitivity of the CPM to the input topography resolution used only over the smallest domain. Figure 3.3 shows this 3 arcsec resolution topography next to the 30 arcsec resolution topography for the smaller d03 LES domains.

For all domains, the simulations are initialized with data from the European Centre for Medium-range Weather Forecast (ECMWF) model (Owens and Hewson 2018). The ECMWF High-Resolution Forecast (HRES) model with $\approx$ 9 km horizontal resolution and 137 vertical model levels is used to incorporate the highest vertical resolution forcing data available. This is not a standard option in WRF and required modifying the WRF preprocessing system (Duda 2011). The model is initialized at 0600 UTC on 20 May 2017. Time is given in UTC for all the analysis, which corresponds with local standard time at the field

site (Portugal observes Western European Summer Time such that UTC+1 is the local time on the simulation date). The first 5 hours of the simulation are relegated to model spinup and excluded from analysis. The ECMWF data provide the lateral boundary conditions for the coarsest grid at relatively fine, 1 hr, intervals throughout the duration of the simulation. For the nested domains, lateral boundary conditions are provided through one-way nesting.

A common strategy to ensure fully developed turbulence in the inner nested simulation domain is to increase the domain size or to locate the area of interest far away from the inflow boundary, i.e. not have it centered within the domain (Rai et al. 2017; Muñoz-Esparza et al. 2017; Taylor et al. 2018; Wiersema et al. 2020). Both of these strategies serve to increase the fetch or distance from the region of interest to the grid boundary. We therefore also test a larger domain size and compare this to results from smaller domains with and without CPM. This reference LES domain, d03_30s_ref, is twice as large in each horizontal dimension compared to the other LES domains. For the reference simulation, the GTOPO30 topography is used because it is readily available with the WRF download and covers the entire globe. The 30 arcsec topography is likely to be used for the purposes of generating turbulence in a coarse LES nest while high resolution topography is usually only used for finer nests covering less extensive areas. The larger domain, d03_30s_ref, is positioned such that the smaller LES domain fits within the south-western quadrant of the reference simulation domain. Two subregions presented later in Section 3.4, occupy the same physical location in every LES. Given easterly winds on this simulation date, the reference domain has significantly more fetch than the smaller LES at these locations. The d03_30s_ref simulation requires about 5 times more CPU-hours compared to the d03_3s_cpm simulation. Meanwhile the computational cost difference between same sized domains with or without CPM is entirely negligible.

3.4 Results and Discussion

Mean Flow Fields

Instrumentation deployed during the Perdigão field campaign included GPS Advanced Upper-Air Sounding System (GAUSS) radiosondes as well as 195 three-component sonic anemometers and 55 temperature-humidity sensors mounted on masts of heights ranging from 2 m – 100 m above ground level (a.g.l.) (Fernando et al. 2019). These towers sampled at 20 Hz but we analyze data averaged to 5 min intervals for comparison of the WRF model to a subset of the tower data from masts at 2 m, 10 m, and 100 m above ground level. The focus of the comparisons to field data is on mean flow fields, wind and temperature data, to provide a basic validation of model performance and context for the investigation of turbulence in the following section. The simulated time period is 20 May 2017. This was a dry, clear day with high clouds and a low pressure system setting up to the southwest of Portugal. Surface winds veered from northeasterly in the morning to easterly in the afternoon, and veered back to northeasterly over the evening. Wind speeds were low, $<$10 m s^{-1}, until night time, when

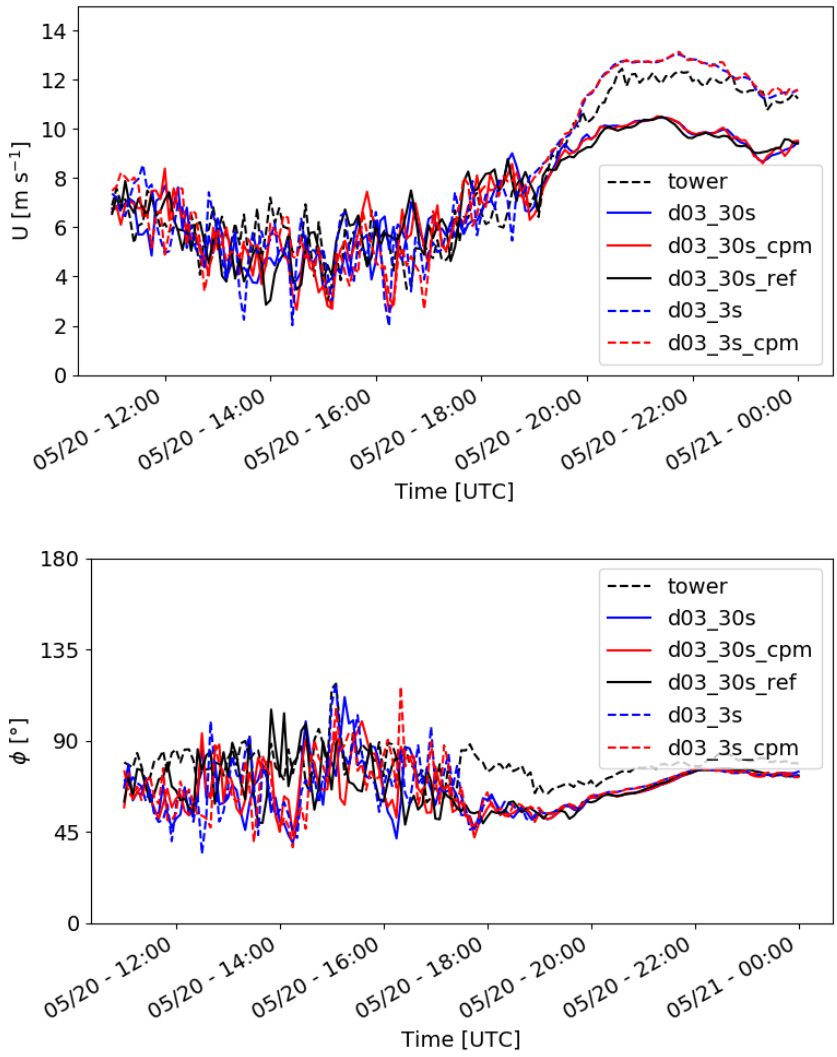

Figure 3.4: Wind speed (top), and wind direction (bottom) time series from 100 m a.g.l. at a tower, tse04, on the ridge of the Vale do Cabrão.

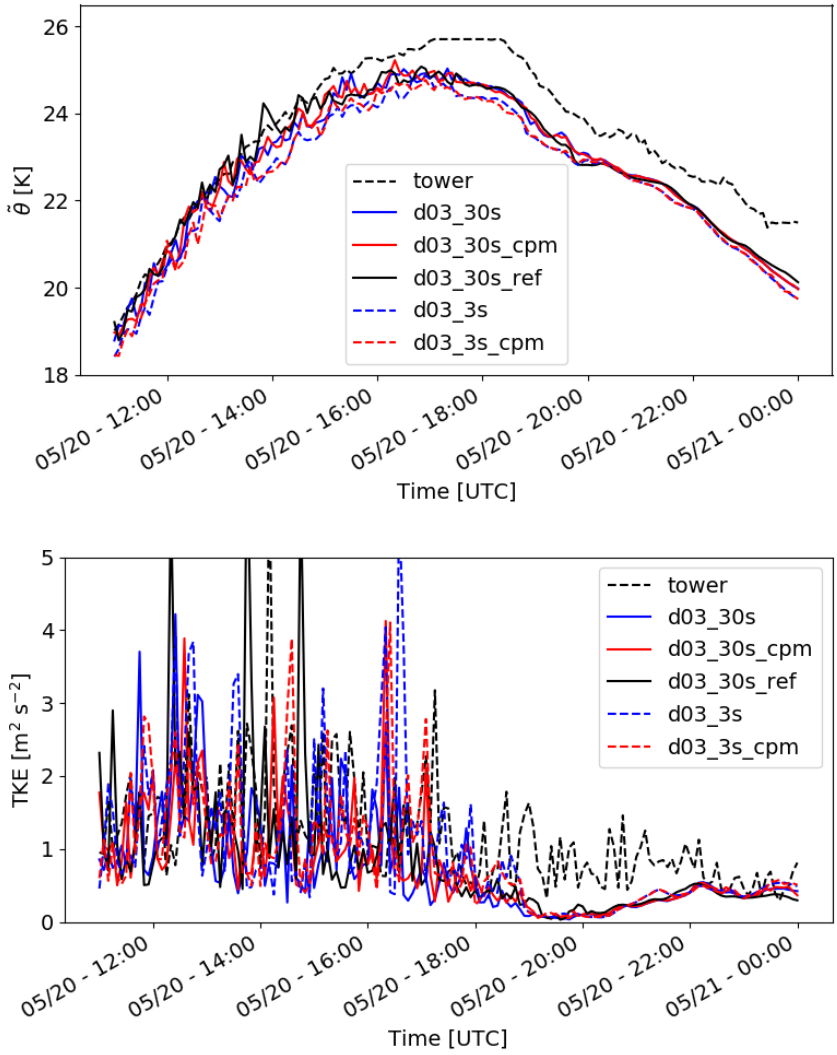

Figure 3.5: Temperature (top) and TKE (bottom) time series from 100 m a.g.l. at a tower, tse04, on the ridge of the Vale do Cabrão.

those accelerated to moderate, <15 m s^{-1}, values.

This section describes comparisons of model results to field data from radiosonde and tower data from the valley ridges. The towers within the valley are not included because the valley is unresolved in simulations with standard 30 arcsec topography. For much of the extent of the valley, the two ridges are merged into a single ridge (Figure 3.3). Error statistics at 2 m and 10 m a.g.l. presented in Table 3.2 reflect errors calculated across 17 towers on the ridges only. These are known as towers tNW03, tNW11, tSE04, tSE13, rSW01, rSW02, rSW03, rSW04, rSW05, rSW06, rSW07, rSW08, rNE01, rNE02, rNE03, rNE06, and rNE07 using the naming convention from the field campaign. The LES data at 2.5 min output

Table 3.2: Biases and root-mean-square errors (RMSE) averaged over the time period between 1100 UTC on May, 20 2017 and 0000 UTC on May 21, 2017 comparing LES model fields interpolated to the locations of towers, excluding those within the unresolved valley. Biases are averages of the difference taken as model data minus observed tower data. The LES data at 2.5 min output interval is first downsampled as described in the body text.

	T2 [K]		U10 [m s^{-1}]		ϕ10 [°]		TKE10 [m^2 s^{-2}]	
Simulation	Bias	RMSE	Bias	RMSE	Bias	RMSE	Bias	RMSE
d03_30s	-0.45	1.15	-1.28	2.52	0.2	25.2	-0.87	1.27
d03_30s_cpm	-0.46	1.14	-1.29	2.53	1.2	25.3	-0.86	1.26
d03_30s_ref	-0.34	1.11	-1.29	2.54	2.9	24.6	-0.86	1.25
d03_3s	-0.69	1.41	0.39	1.84	2.0	24.6	-0.66	1.09
d03_3s_cpm	-0.70	1.41	0.37	1.86	1.4	23.7	-0.65	1.09

Table 3.3: As in Table 3.2 but for data at 100 m above ground level.

	T100 [K]		U100 [m s^{-1}]		ϕ100 [°]		TKE100 [m^2 s^{-2}]	
Simulation	Bias	RMSE	Bias	RMSE	Bias	RMSE	Bias	RMSE
d03_30s	-0.45	0.62	-0.86	1.55	-9.8	17.8	-0.40	0.90
d03_30s_cpm	–0.44	0.61	-0.90	1.55	-9.5	16.5	-0.35	0.85
d03_30s_ref	-0.38	0.61	-0.86	1.67	-7.4	15.6	-0.32	0.97
d03_3s	-0.87	0.93	0.12	1.04	-9.8	16.9	-0.25	0.95
d03_3s_cpm	-0.86	0.93	0.13	0.97	-9.8	16.2	-0.25	0.83

interval is first downsampled to the 5 min averaging interval of the tower data using the trapezoidal rule. Adopting the convention that u_i^{2n} corresponds to the velocity field after $2n2.5$ min simulated time, the downsampling technique for velocity is

$$\overline{u_i^{2n}} = \frac{1}{4}\left(u_i^{2n-1} + 2u_i^{2n} + u_i^{2n+1}\right) \tag{3.5}$$

for integer, n. Potential temperature is averaged with the same approach as with velocity. Turbulent kinetic energy is calculated as

$$TKE^{2n} = \overline{TKE_{\text{sg}}^{2n}} + \frac{1}{2}\sum_{i=1}^{3}\frac{1}{3}\sum_{m=-1}^{1}\left(\overline{u_i^{2n}} - u_i^{2n+m}\right)^2 \tag{3.6}$$

where the first term represents average subgrid TKE, prognosticated by the LES closure (Moeng 1984), and the second term represents the resolved turbulence. Heights of 2 m and 10 m a.g.l. are used because they are commonly reported for model validation. Specifically, temperature taken at 2 m, T2, along with wind variables taken at 10 m, U10 for wind speed, ϕ10 for wind direction, and TKE10 for turbulent kinetic energy, are reported. Additional

Table 3.4: Biases and root-mean-square errors (RMSE) comparing LES results to GAUSS radiosonde data from soundings released from the center of the Vale do Cobrão (red 'x' in Figure 3.2) at 11:13:11 UTC, 17:16:25 UTC, and 23:13:28 UTC. Biases are averages of the difference taken as model data minus observed radiosonde data interpolated to the heights of the LES model levels below 5 km above sea level.

Simulation		d03_30s		d03_30s_cpm		d03_30s_ref		d03_3s		d03_30s_cpm	
		Bias	RMSE	Bias	RMSE	Bias	RMSE	Bias	RMSE	Bias	RMSE
U [m s^{-1}]	1113	-1.21	2.09	-1.13	2.04	-1.18	2.05	-1.11	1.94	-1.19	2.06
ϕ [°]	1113	-2.71	29.32	-3.05	33.77	1.09	28.99	-7.12	37.18	-9.64	38.04
θ [K]	1113	-0.63	0.85	-0.62	0.87	-0.64	0.81	-0.55	0.68	-0.57	0.82
Q_v [g kg^{-1}]	1113	-0.33	0.68	-0.23	0.64	-0.08	0.48	-0.19	0.59	-0.19	0.57
U [m s^{-1}]	1716	0.29	1.87	0.53	1.62	0.39	1.32	0.20	1.34	0.20	1.39
ϕ [°]	1716	-0.97	27.21	-2.12	25.65	-3.34	21.75	1.19	23.19	4.68	25.55
θ [K]	1716	-0.92	1.25	-1.03	1.26	-0.91	1.36	-0.87	1.23	-0.95	1.21
Q_v [g kg^{-1}]	1716	0.25	0.66	0.28	0.57	0.14	0.69	0.22	0.72	0.27	0.64
U [m s^{-1}]	2313	-0.76	2.27	-0.76	2.27	-0.87	2.34	-0.62	2.05	-0.64	2.05
ϕ [°]	2313	-0.21	6.90	-0.39	7.10	0.47	6.83	4.29	26.15	3.98	25.77
θ [K]	2313	-1.31	1.46	-1.31	1.46	-1.27	1.41	-1.17	1.31	-1.17	1.31
Q_v [g kg^{-1}]	2313	0.25	0.66	0.25	0.66	0.24	0.66	0.16	0.64	0.16	0.64

instrumentation was also installed at 100 m a.g.l. for two of these towers, tSE04 and tSE13. These two towers are used to calculate the error statistics in Table 3.3 at 100 m a.g.l., which is closer to typical hub heights of large wind turbines, and also avoids near-surface extrapolation errors in the WRF output. Extending the naming convention above, these variables are abbreviated as T100, U100, ϕ100, and TKE100 for temperature, wind speed, wind direction, and turbulent kinetic energy at 100 m a.g.l., respectively. Time series of these variables at tSE04 are shown in Figure 3.4 and Figure 3.5.

Varying the resolution of the topography results in larger differences across models for these variables than application of CPM does. Notably, the bias of wind speed flips sign depending on the topography resolution (Table 3.2) due to a bifurcation of models during the ramp up of wind speed seen during the evening, when winds increase from $\approx$6 m s^{-1} at 1700 UTC to $\approx$12 m s^{-1} by 2030 UTC at tSE04 and 100 m a.g.l. (Figure 3.4). After this ramp up, simulations with 30 arcsec topography underestimate the wind speeds by $\approx$2 m s^{-1} while those with 3 arcsec topography overestimate wind speed by $\lesssim$ 1 m s^{-1} for the remainder of the night. The temperature time series in Figure 3.5 also show more sensitivity to topography resolution. In this case it is the finer resolved topography models that have a greater magnitude bias earlier in the simulated period. All models develop an approximately 2 K cold bias throughout the daytime that persists through the nocturnal period. The TKE time series show that the TKE from the model is generally lower than that measured from the towers. Using CPM and finer topography do not have a strong effect on the TKE far from the boundary, at the location of the towers, but the biases are slightly reduced overall.

Model results are also compared to the GAUSS radiosonde observations from soundings

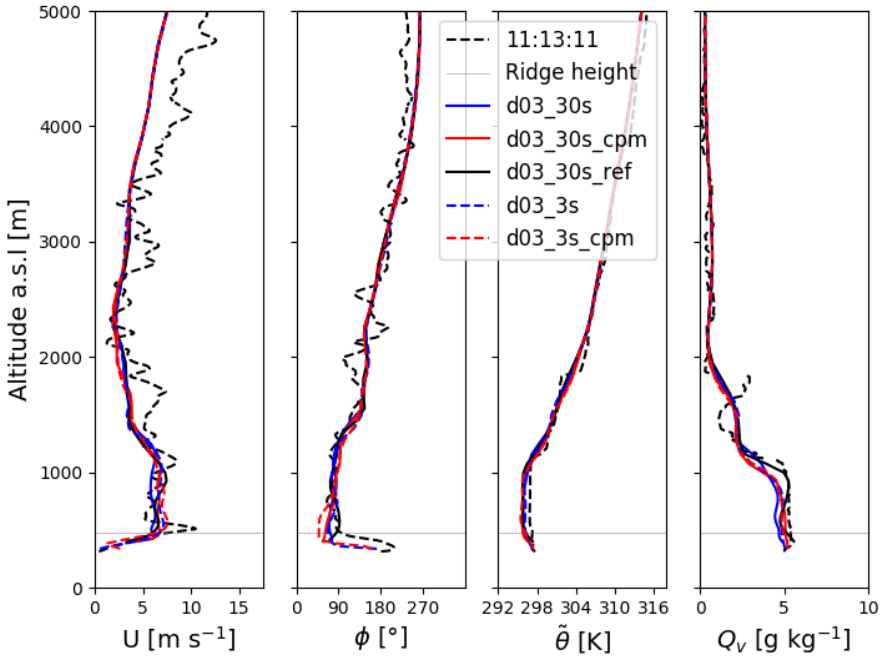

Figure 3.6: Profiles of wind speed, wind direction, potential temperature, and specific humidity comparing LES results to GAUSS radiosonde data from a sounding released from the center of the Vale do Cobrão (red 'x' in Figure 3.2) at 11:13:11 UTC 20 May 2017. The horizontal gray line, labeled 'Ridge height,' is given as 473 m a.s.l., corresponding to the base of tSE04.

released on the valley floor at approximately 1115 UTC (Figure 3.6), 1715 UTC (Figure 3.7), and 2315 UTC (Figure 3.8). These times of day represent three different atmospheric stability regimes: strongly convective, weakly convective, and weakly stable, respectively. All the LES domains appear to perform similarly, as confirmed by error statistics (Table 3.4). For example, biases for wind speed are consistently under 1.5 m s^{-1}, though root-mean-square errors (RMSE) can be larger in part due to fine-scale oscillations not resolved by the model. Similarly, biases of wind direction are quite low, less than 10° in magnitude, though root-mean-square errors are higher, ≈30° across model configurations. In these profiles, only the simulations with the finer 3 arcsec topography input include the strong veer observed at the lowest elevations. For simulations with coarser 30 arcsec topography, the solution is not even defined until nearer the altitude marked 'Ridge height' on the sounding profiles in Figures 3.6, 3.7, 3.8. This height is given as 473 m above sea level (a.s.l.), corresponding to the base of tSE04, the tower whose time series from 100 m above this height are shown in Figures 3.4 and 3.5. As in the tower data, all models show a cold bias at each sounding time and tend to underpredict the boundary-layer depth during the daytime. Despite this,

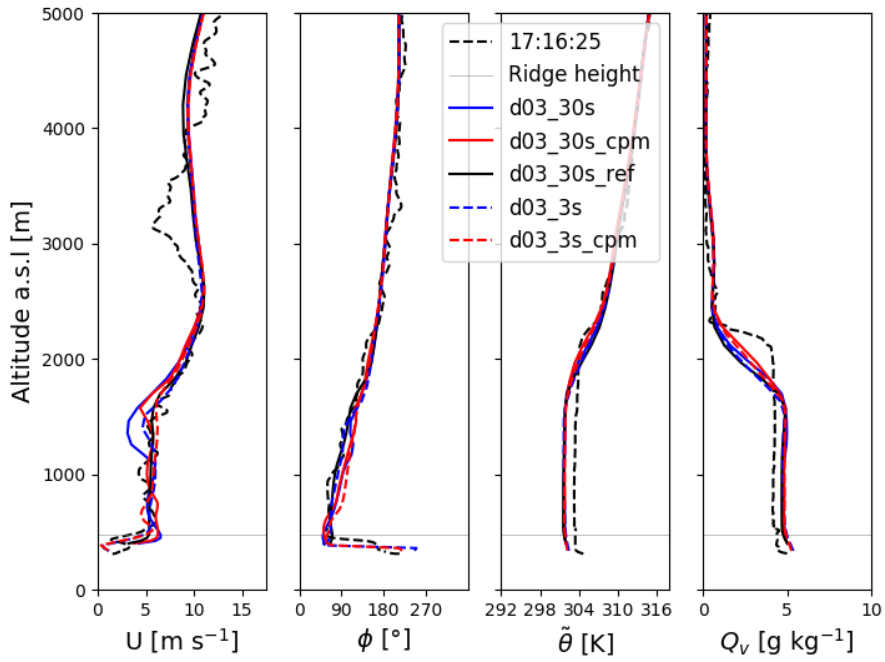

Figure 3.7: As in Figure 3.6 but comparing to a sounding released at 17:16:25 UTC 20 May 2017.

the general diurnal cycle is qualitatively captured well. At 1113 UTC, below a capping inversion around 1 km a.s.l., there is a well mixed layer with nearly due easterly flow. By 1716 UTC, the capping inversion is around 2 km a.s.l and the well mixed layer has grown in the profiles of temperature and water vapor while the wind fields are similar. The wind speeds do increase, to a maximum of 17 m s^{-1}, near the bottom of a residual layer around 1 km a.s.l at 2313 UTC. Temperature profiles are generally stable below the residual layer at this later time. Though all the models generally perform similarly, the profiles of the nocturnal boundary layer at 2315 UTC show particularly notable agreement across models.

Results in Figures 3.4 – 3.8 and in Tables 3.2 and 3.4 show that the WRF simulations compare similarly well to the radiosonde and surface tower data for all cases. Notably, the simulations with and without CPM are similar in the time series, profiles, and error statistics considered so far while more significant difference are due to the topography resolution. Negligible differences across models may seem to suggest that the CPM has no discernible effect on the simulations. It is important to recognize that so far the variables used to validate the model are all mean fields, taken far from the domain lateral boundaries. In the following section, examining the model's representation of turbulence, it is shown that the CPM does indeed affect simulations in important ways by reducing the fetch required for turbulence to fully develop.

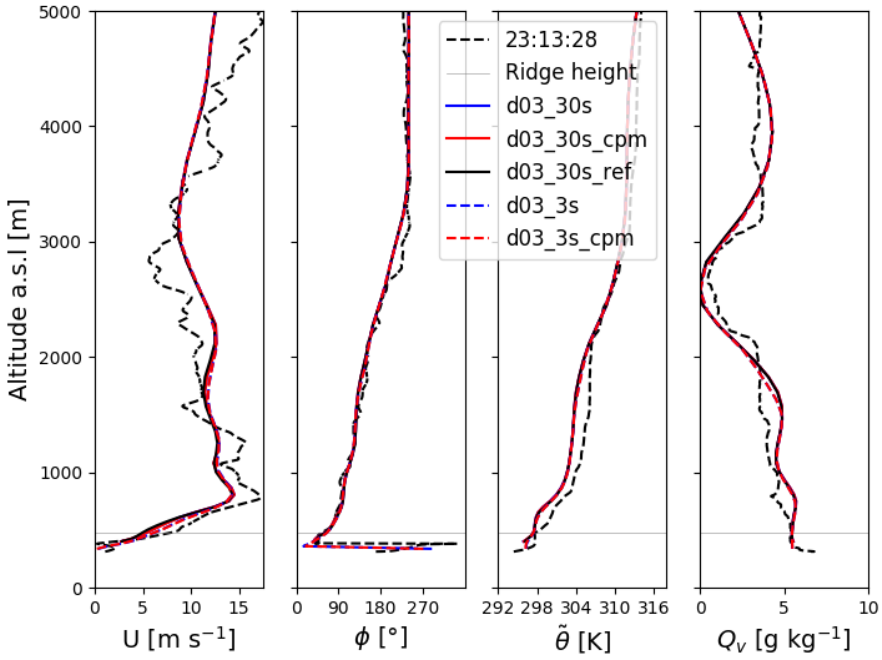

Figure 3.8: As in Figure 3.6 but comparing to a sounding released at 23:13:28 UTC 20 May 2017.

Turbulence Structure

With 150 m grid spacing, some of the eddies in the inertial subrange are explicitly resolved in the LES. Differences in the resolved turbulence produced by the different model configurations can be quite striking, despite the differences in the mean flow fields examined above being relatively small. The following sections examine the turbulent structure of the LES simulations over the Perdigão domain at various times during the day. The analysis is focused on three time periods coincident with the three radiosonde releases discussed in the previous section. Each time is representative of a different stability class: strongly convective (1115 UTC), weakly convective (1715 UTC), and weakly stable (2315 UTC). As seen in the radiosondes (Figures 3.6, 3.7, and 3.8), the mean horizontal flow in the boundary layer is easterly above the ridge with ∼200 m relief. The model's seventh vertical level, at ∼200 m a.g.l., lies within this region of easterly flow though its elevation a.s.l. varies with the terrain. This level is selected for the investigation of turbulence through contours and spectra from the vertical velocity field. In LES, the resolved component of vertical velocity is nearly equal to its turbulent fluctuation, because the spatial average of vertical velocity tends to zero as the average is taken over larger areas. The contours of vertical velocity can therefore be used to visually assess part of the turbulent kinetic energy of the flow. Turbulent structures

appear as regions of higher magnitude vertical velocity, updrafts and downdrafts.

While the contours of vertical velocity are helpful to get a qualitative sense of the effects of the CPM, a more quantitative analysis is aided by computing the kinetic energy spectra. For this purpose, one-dimensional spectra are computed from N points of u_i ($u_1 = u$ for zonal, $u_2 = v$ for meridional, or $u_3 = w$ for vertical velocity) on a transect of length $L = N\Delta s$ in the s-direction ($s = x$ for West–East, or $s = y$ for South–North). In example, for w, following Durran et al. (2017), the discrete spectral density, E_{ws}, is defined such that

$$\frac{1}{2}\langle w^2 \rangle_s = \frac{1}{L}\sum_{j=1}^{N}\frac{w_j^2}{2}\Delta s = \sum_{m=1}^{N/2+1} E_{ws,m}\Delta k_s \tag{3.7}$$

where $\Delta k_s = \frac{2\pi}{L}$, and $\langle\cdot\rangle_s$ indicates averaging in the s-direction throughout the manuscript. To achieve this normalization, the discrete spectral densities are calculated as

$$E_{ws,m} = \frac{\Delta s|\hat{w}_m|^2}{2\pi N\left(1+\delta_{m,\frac{N}{2}+1}\right)} \tag{3.8}$$

where $\hat{w}$ is the discrete Fourier transform of w following the normalization conventions of numpy's fft or rfft routine, and δ is the Kronecker delta operator (Durran et al. 2017). In this normalization convention, the forward transform is not normalized such that

$$\hat{w}_m = \sum_{j=1}^{N} w_j \exp\left[\frac{-2\pi i}{N}(m-1)(j-1)\right]. \tag{3.9}$$

Weakly Convective Case

At 1715 UTC, turbulent structures are visually apparent in the contours of vertical velocity in Figure 3.9 and Figure 3.10. Each of the simulations contains a region of smoother flow near the eastern inflow boundary, where vertical velocity is nearly zero and larger-scale structures persist over longer distances than they do in the rest of the domain. From the vertical velocity contours, it appears that finer scale turbulence develops consistently only after ≈20 km of fetch from the eastern boundary in d03_30s_ref. That is, turbulence appears fully developed only over $x \in$ [0,50] km, which excludes the eastern 22 km in the domain. Similarly, the larger structures diminish only after about 16 km of fetch in d03_30s for this easterly flow case, i.e. limiting the region with well developed turbulence to $x \in$ [0,20] km. There are some regions which develop particularly streaky velocity structures, apparent in the south-east of d03_30s_ref, $x \in$ [60,70] km and $y \in$ [0,30] km. These streaky structures have been observed in numerous previous studies (Weckwerth et al. 1996; Rai et al. 2017; Babić and De Wekker 2019). While convective rolls likely do develop in weakly convective and sheared boundary layers, they are also likely over-represented in numerical simulations. The presence of these rolls indicates under-developed model turbulence that influences local turbulence characteristics and shear related mixing (Geurts 2001). In flat terrain cases, these structures can persist up to 54 km before they begin to dissipate (Muñoz-Esparza

et al. 2014, 2015). In the example here, most of the largest streaky structures break up as the flow passes over the rolling hills in the domain. Further, these structures do not occur in the same physical locations in the reference domain as they do in the smaller simulations. Rather, they are distinctly tied to the distance or fetch from the inflow boundary.

One way to quantify the fetch required for turbulence to fully develop is to compute the spectral densities, defined above, at varying distances from the inflow boundary. Following Muñoz-Esparza et al. (2017), Figure 3.11 computes such spectra from the vertical velocity field shown in Figure 3.9a over N=128 points in the South–North direction with $y \in [8.4,27.6]$ km to evaluate the particularly 'streaky' region noted above. A resolved inertial subrange, over which spectra are nearly parallel to a -5/3 power law line, is expected to develop with increasing fetch as more turbulent kinetic energy is produced. We also expect energy spectral densities to be increasing over farther fetch as turbulence develops, as seen over the first 40 points of fetch, after which the signal is less clear over the next 40 points of fetch. Measured this way, the spectra suggest turbulent energy at 60 points of fetch is more intense than at 80 points of fetch. This region of the domain, however, is precisely the region over which turbulent streaks seem to be breaking up in the velocity contours. During these easterly wind conditions, spectra computed in the y-direction therefore do not seem to reliably capture what is observed in the contours to be the transition from larger scale streaks to finer scale turbulent structures. As the rolls are oriented with a spin around the x-axis and thus produce strong oscillations in the y-direction, the correspondingly large y-direction spectra are misleading in the current context.

To remedy this, another method of measuring the turbulence is required. Simply computing two-dimensional spectra is one possibility that has been tested (not shown). However, computing one-dimensional spectra in the x-direction produces a clearer signal of the change in turbulence over fetch, because the roll structures are enlarged in the x-direction given easterly winds. For this reason, we prefer a pseudo-two-dimensional technique in which spectra are calculated for N=64 points in the x-direction before being averaged over 180 y-direction indices, and over 13 time indices (30 minutes at 2.5 min intervals). The horizontal velocities have their linear tendencies, from the difference between the 1^{st} and 64^{th} points, removed before Fourier decomposition. Two subregions are selected to compute spectral density at different distances from the inflow boundary. One subregion, outlined with solid black lines in Figure 3.9 and all following contour plots, has 40 points of fetch before the first points in d03_30s, d03_30s_cpm, d03_30s, and d03_30s_cpm. This region will be referred to as the short fetch subregion. The other subregion, referred to as the long fetch subregion, is outlined with a dashed black line and has 120 points of fetch for the same LES domains.

The pseudo-two-dimensional energy spectra for each velocity component are computed at the short fetch subregion and long fetch subregion (Figure 3.12). At both fetches, the velocity fields are taken at 200 m a.g.l. and averaged over 30 minutes centered around 1715 UTC, the time plotted in Figure 3.9 and Figure 3.10 when weakly convective conditions are observed. The efficacy of CPM is demonstrated at the short fetch subregion, where we have the benefit of comparing spectra from near the boundary of the small domains to d03_30s_ref which allows for a much longer fetch before the first transect location. Recall, these smaller LES

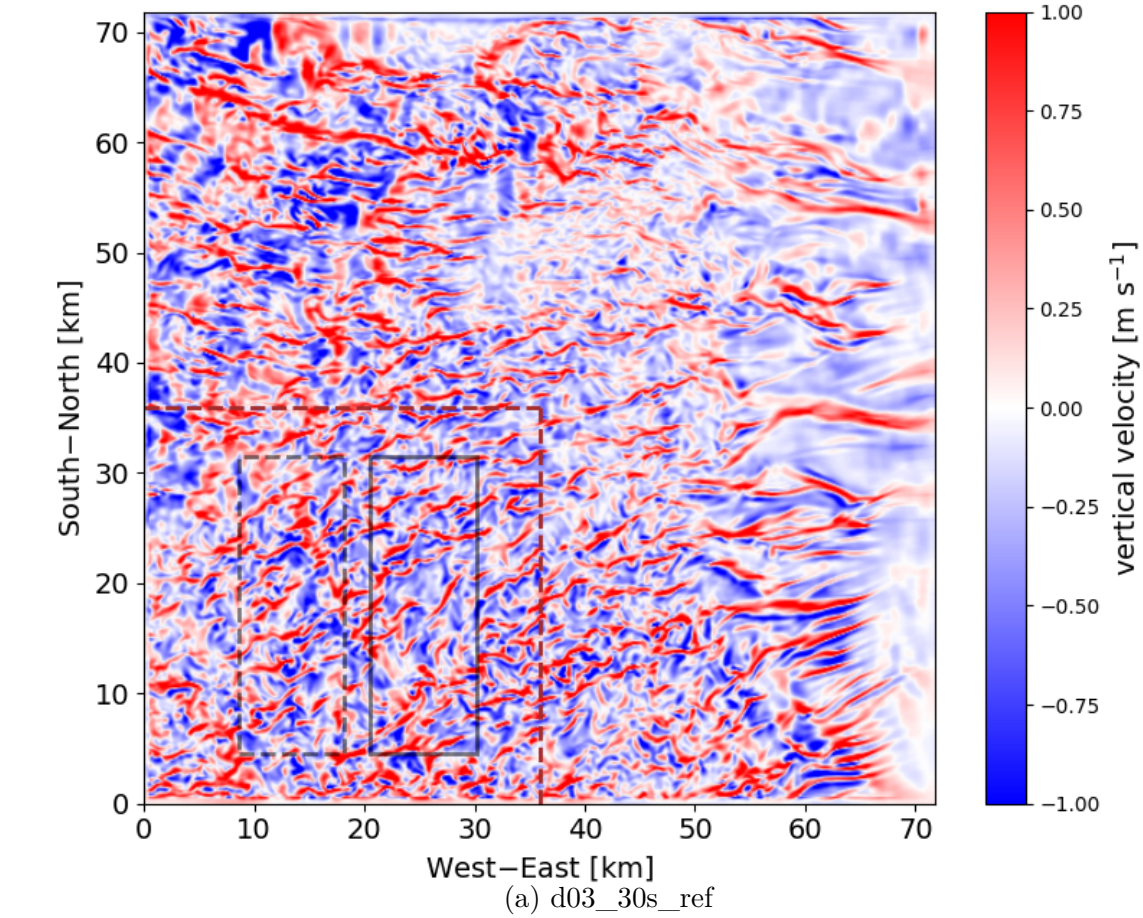

(a) d03_30s_ref

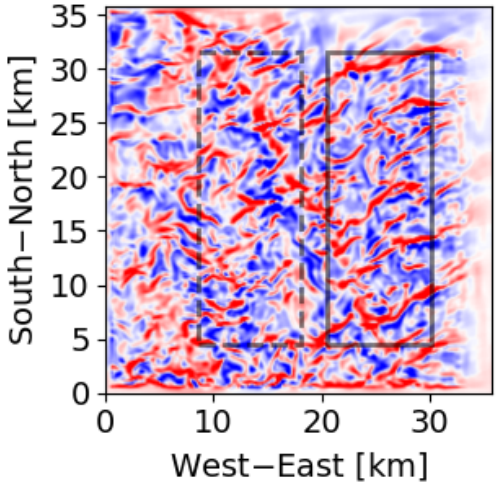

(b) d03_30s_cpm

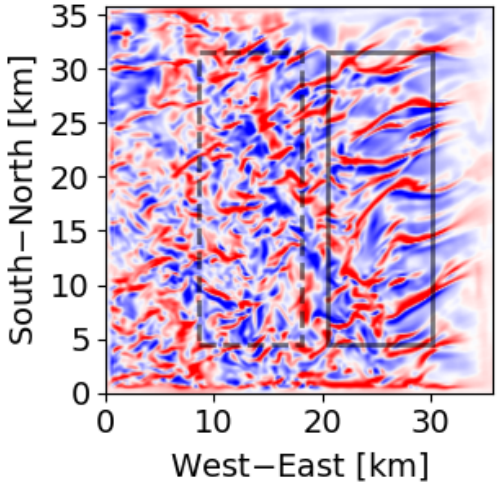

(c) d03_30s

Figure 3.9: Contours of vertical velocity from ∼200 m a.g.l., the 7th model level of d03_30s, d03_30s_cpm, and d03_30s_ref at 1715 UTC 20 May 2017. Dashed brown lines in (a) demarcate the locations of the boundaries of the smaller LES, whose results are shown in (b) and (c). Solid black and dashed black outlined subregions are used for computing power spectra in Figure 3.12.

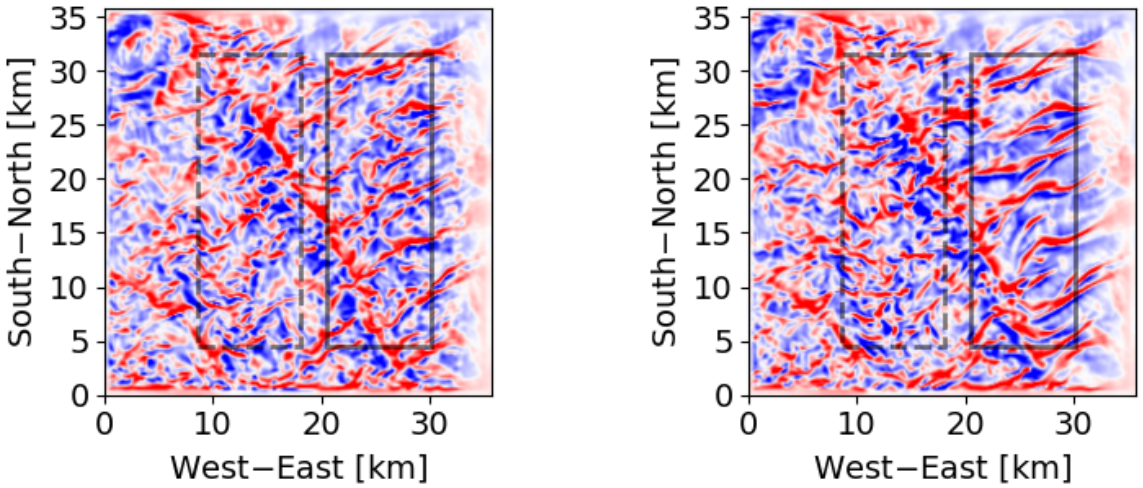

(a) d03_3s_cpm (b) d03_3s

Figure 3.10: As in Figure 3.9b and Figure 3.9c but for simulations with 3 arcsec topography input.

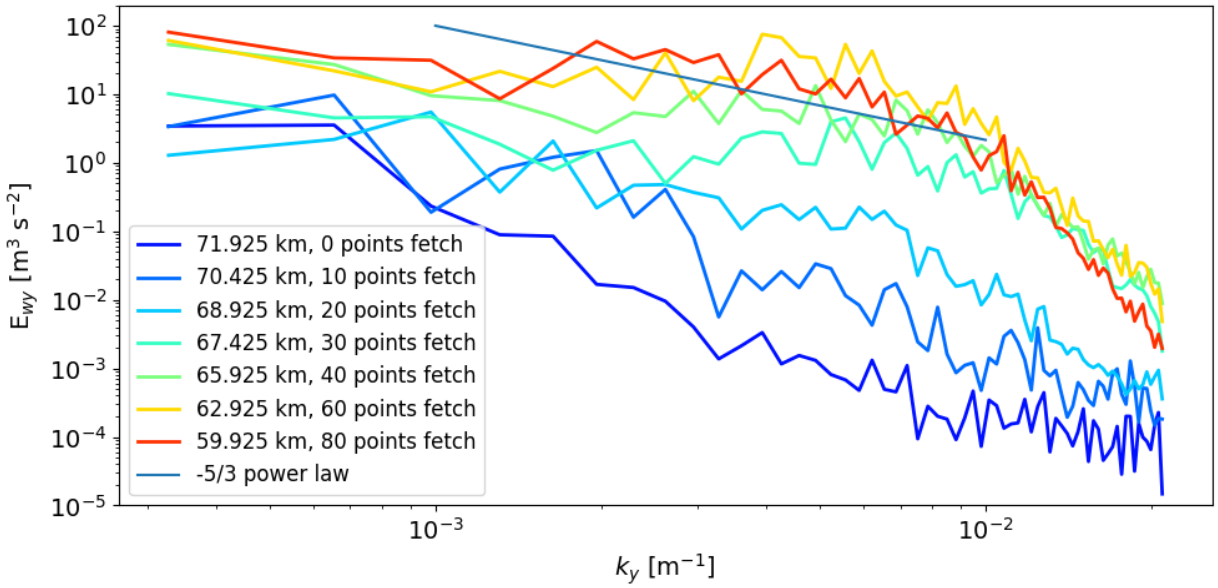

Figure 3.11: Spectral density of vertical velocity from 128 point y-transects at different x locations and points of fetch from the eastern inflow boundary of d03_30s_ref. Model data are from the seventh vertical level, and averaged over 13 times from model output at 2.5 min intervals over the 30 minutes centered about 1715 UTC, roughly concurrent with the 1716 radiosonde release on 20 May 2017.

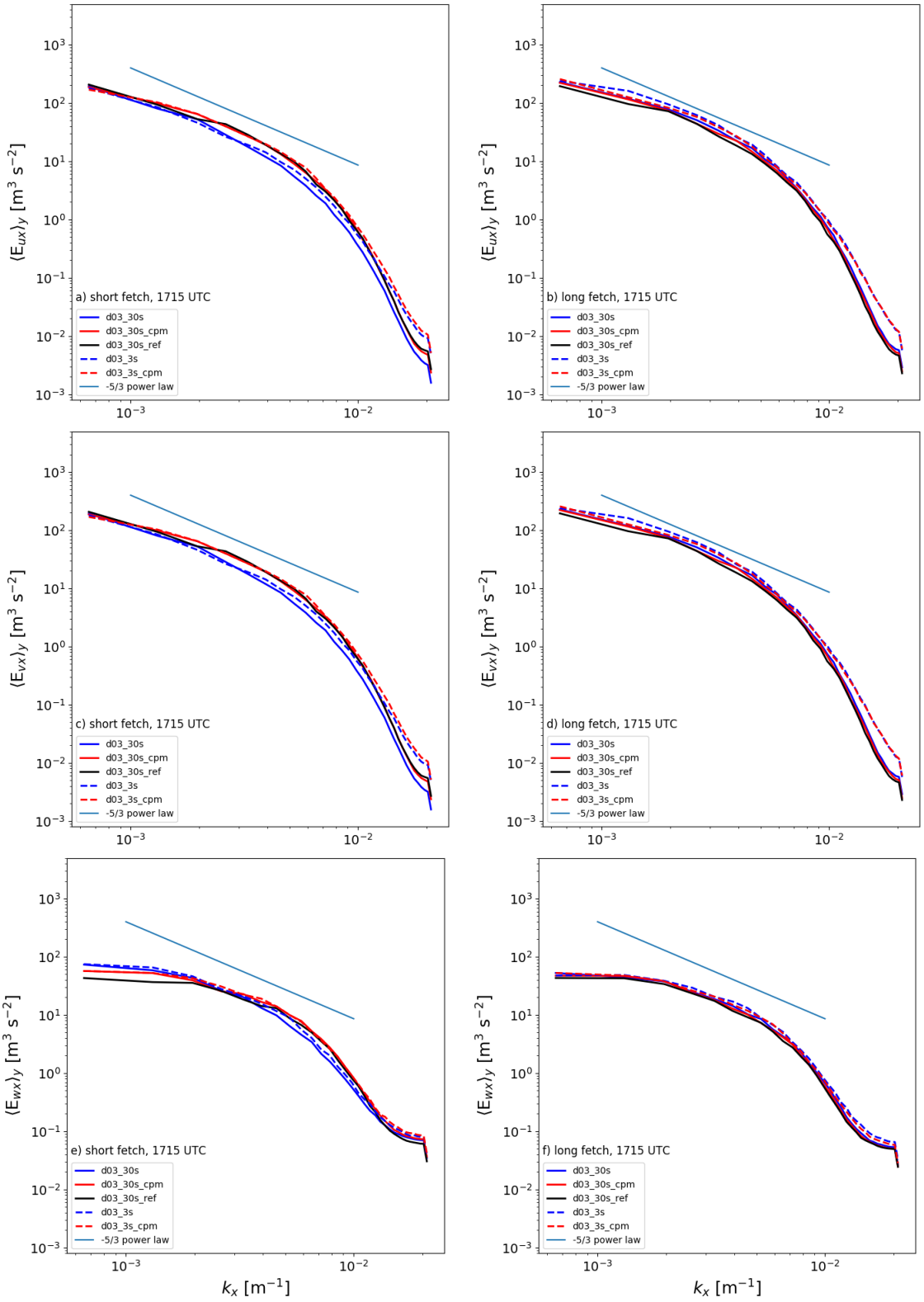

Figure 3.12: Spectral density of zonal (top), meridional (middle), and vertical (bottom) velocity from subregions shown in Figure 3.9 after a minimum of 40 (left) points and of 120 (right) points of fetch from the smaller LES boundary (280 and 360 points for d03_30s_ref). Spectra are averaged for 180 transects for each of 13 times (30 min) centered about nominal time 1715 UTC, roughly concurrent with the 1716 radiosonde release on 20 May 2017.

domains fit within a quadrant of the reference simulation, d03_30s_ref. The regions are drawn for the same physical locations as in the smaller LES, but the reference domain will have an additional fetch of 240 grid points.

As we may expect from the contour plots, short fetch spectra from d03_30s_cpm and d03_3s_cpm agree well with those from d03_30s_ref for a range of wavenumbers, e.g. $k \in [4 \cdot 10^{-3}, 1.1 \cdot 10^{-2}]$ m^{-1} for vertical velocity, over which simulations without CPM are missing energy. Though the addition of higher resolution topography, as in d03_3s, increases the energy compared to its low resolution topography counterpart, d03_30s, their spectral densities are missing energy at these wavenumbers compared to the reference simulation spectra. These wavenumbers are not entirely in the resolved inertial subrange, over which the model spectra are nearly parallel to the -5/3 slope line, and include wavenumbers just greater than those of the resolved interial subrange. Particularly for vertical velocity spectra, at the lowest wavenumbers the smaller LES actually have more energy than the reference simulation, perhaps due to effects of the boundary or the presence of the streaks. Similarly, the vertical kinetic energy of the very highest wavenumbers are increased in the smaller LES compared to the reference simulations. This may suggest that the turbulent energy cascade is still developing at the high wavenumbers for the smaller simulations. For the high resolution topography simulations, some of this energy at the highest wavenumbers is likely due to the effects of the terrain. Especially for the horizontal velocity spectra after long fetch, the high resolution topography runs have increased energy at the highest wavenumbers, even as the rest of the spectra collapse (Figure 3.12). The eventual collapse of spectra from LES with and without CPM suggests the application of CPM does not affect the long fetch characteristics of the turbulence while it does accelerate the development of turbulence. For the weakly convective conditions observed around 1715 UTC, simulations with CPM developed turbulence over 40 points of fetch that is similar to that from a simulation without CPM but with 280 points of fetch.

Muñoz-Esparza and Kosović (2018) show the importance of the CPM can be predicted by the ratio of characteristic wind speed at the top of the capping inversion, U_{ci}, to a convective velocity scale,

$$w_* = \left(\frac{g}{\theta} z_i \left\langle w'\theta' \right\rangle_{\text{sfc}} \right)^{1/3}, \tag{3.10}$$

where $\left\langle w'\theta' \right\rangle_{\text{sfc}}$ is the surface heat flux. They find that for $U_{ci}/w_* > 5$, the CPM will be especially beneficial. In the current weakly convective case, with $U_{ci} = 10$ m s^{-1}, $z_i = 2$ km and $\left\langle w'\theta' \right\rangle_{\text{sfc}} = 0.05$ K m s^{-1}, the ratio, $U_{ci}/w_* = 7$, and the expected effects of CPM are apparent, as predicted, at this time. As this time was selected on the basis of the radiosonde launch schedule, and not on maximizing the ratio, U_{ci}/w_*, the CPM may be even more beneficial later in the evening transition as the surface heat flux decreases.

In summary, the x-direction one-dimensional spectra, computed over short fetch and long fetch regions, demonstrate a clear advantage to using CPM to trigger appropriate length scales. Instead of requiring 280 grid points to develop turbulence under standard grid nesting configurations, nested WRF simulations using CPM can develop over only about 40

points to an equivalent level of turbulence. There is no detrimental effect seen from adding the perturbations, as the level of turbulence at long fetches is unaffected and mean flow differences are minimal.

Strongly Convective Case

The benefits of the CPM are clearly demonstrated during the evening transition time period selected above. Other times of day show different and sometimes less impact of the CPM due to the effects of atmospheric stability. At 1115 UTC, stronger convection is evidenced by smaller thermal cells in the vertical velocity contours (comparing Figures 3.13 and 3.14 to Figures 3.9 and 3.10). Under strong convective conditions the flow is seen to develop considerably smaller scales, which challenges the numerical resolution and accuracy by introducing additional high-pass dynamics in the computational model (Geurts and van der Bos 2005). During this time, the fetch required for streaky structures to develop into fully convective turbulence appears to drop to approximately 12 km in d03_30s_ref and only 6 km in the smaller domains, as seen in the contours of vertical velocity. This is confirmed by the vertical velocity power spectra (Figure 3.15) of the smaller LES that generally agree with the spectrum from d03_30s_ref, even after limited fetch. Examining power spectra associated with the other two components of velocity, we can see some benefit of the CPM method, but this effect is small compared to that of the weakly convective case. Corroborating the hypothesis of Rai et al. (2017), the combined influence of complex terrain and convection are sufficiently strong that finer scale turbulence develops quickly after the inflow enters the domain regardless of CPM being applied or not. The lessened effects of CPM in this strongly convective case compared to the previous weakly convective case are related to the ratio of characteristic wind speed to convective velocity scale. In the strongly convective case, with $z_i = 1$ km and $\langle w'\theta' \rangle_{\text{sfc}} = 0.3$ K m s^{-1}, the ratio, $U_{ci}/w_* = 2.8$, is less than the threshold, $U_{ci}/w_* \lesssim 3$, proposed by Muñoz-Esparza and Kosović (2018). This confirms for a real terrain case what has been observed in ideal cases, that the CPM is less impactful when the convective velocity scale is sufficiently large relative to a characteristic wind speed. Further, during these strongly convective conditions, the use of higher resolution topography does not affect the spectra as much.

Weakly Stable Case

At night (2315 UTC), the reference simulation, d03_30s_ref, does not generate apparent small scale turbulent motions even over its extensive fetch; neither do the smaller LES cases. Rather, the velocity contours (Figure 3.16 and Figure 3.17) are dominated by what appear to be internal gravity wave structures with alternating streaks of negative and positive vertical velocity. These streaks are aligned in the spanwise direction (and are not aligned in the streamwise direction as are the spurious convective rolls or streaks seen earlier). Simulations with the same topography resolution result in similar spectra (Figure 3.18) at the short fetch subregion regardless of the application of CPM. This is similar to the strongly convective

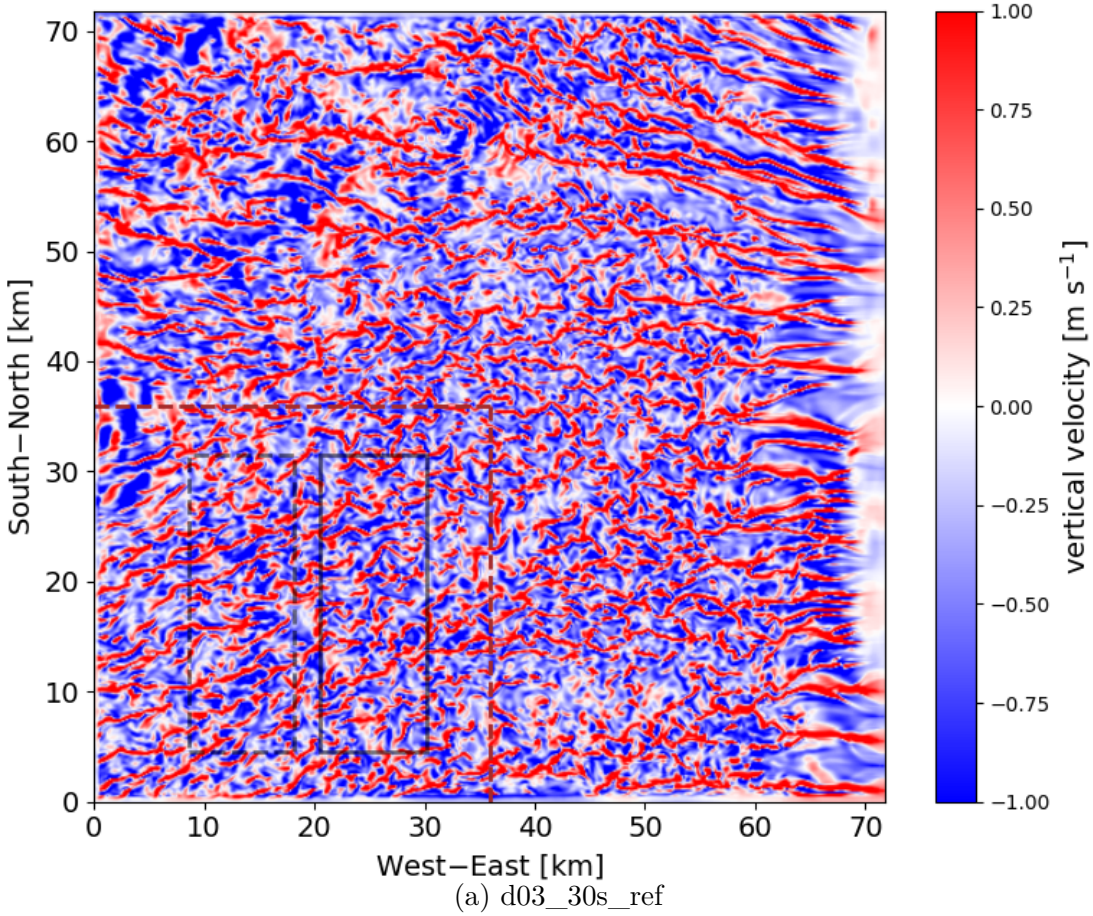

(a) d03_30s_ref

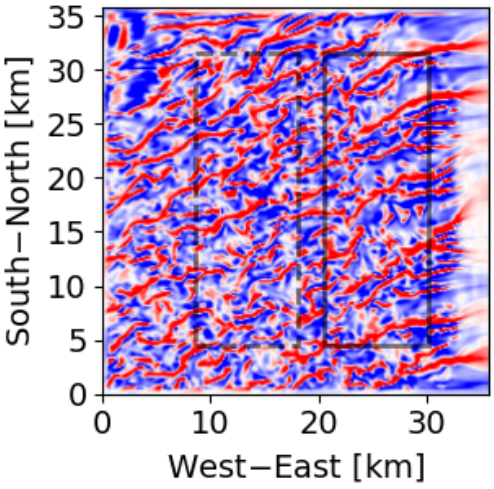

(b) d03_30s_cpm

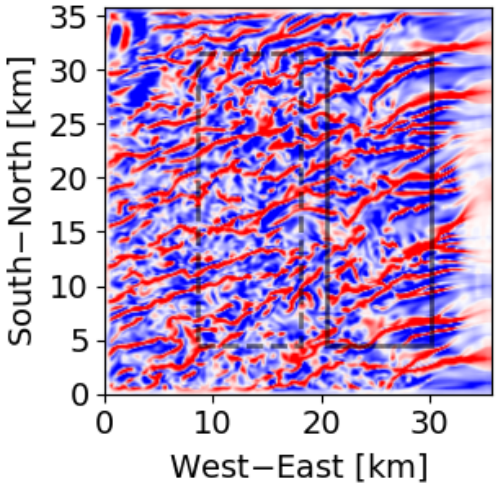

(c) d03_30s

Figure 3.13: As in Figure 3.9 but at 1115 UTC 20 May 2017.

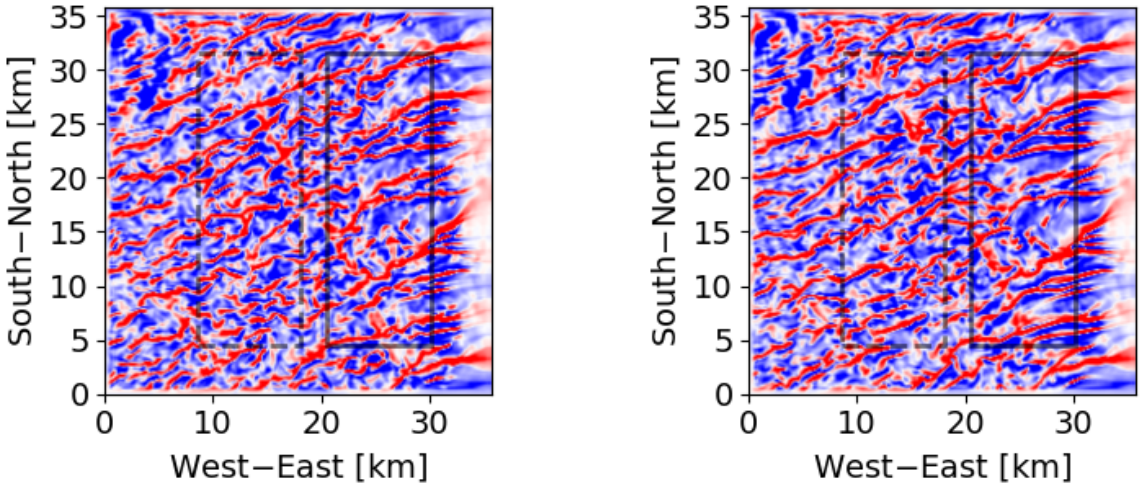

(a) d03_3s_cpm (b) d03_3s

Figure 3.14: As in Figure 3.13b and Figure 3.13c but for simulations with 3 arcsec topography input.

case in that the application of CPM does not significantly change the model turbulence. Conversely, varied topography results in differences between spectra that persist to the long fetch subregion more notably than in the convective cases. The higher resolution topography simulations have much higher spectral density at all but the lowest wavenumbers. This is reflected in small scale structures apparent in the vertical velocity contours of the high resolution topography cases (Figure 3.17) that are missing in the low resolution topography LES including the reference simulation (Figure 3.16). However, this increased energy is likely more reflective of increased wave energy in the mean flow field, rather than turbulent energy, because no inertial subrange develops.

Using higher resolution topography and extending the domain fetch as in d03_30s_ref do not help the model produce an inertial subrange in this stable case. This indicates that the $\Delta x = 150$ m resolution may be insufficient for the stable conditions described here. The CPM does not provide significant benefit for simulations of the nocturnal boundary layer at this coarse resolution. Increasing the resolution of the input topography is recommended for developing the fine scale features of the nocturnal boundary layer, but, at the current resolution, these features are most likely associated with the mean gravity waves due to the topography itself rather than with resolved turbulence.

3.5 Summary and Conclusion

The cell perturbation method (CPM) is used here to accelerate the development of realistic turbulence in nested large-eddy simulations performed using the WRF model over complex terrain. This is, to the authors' knowledge, the first study in which the effects of CPM

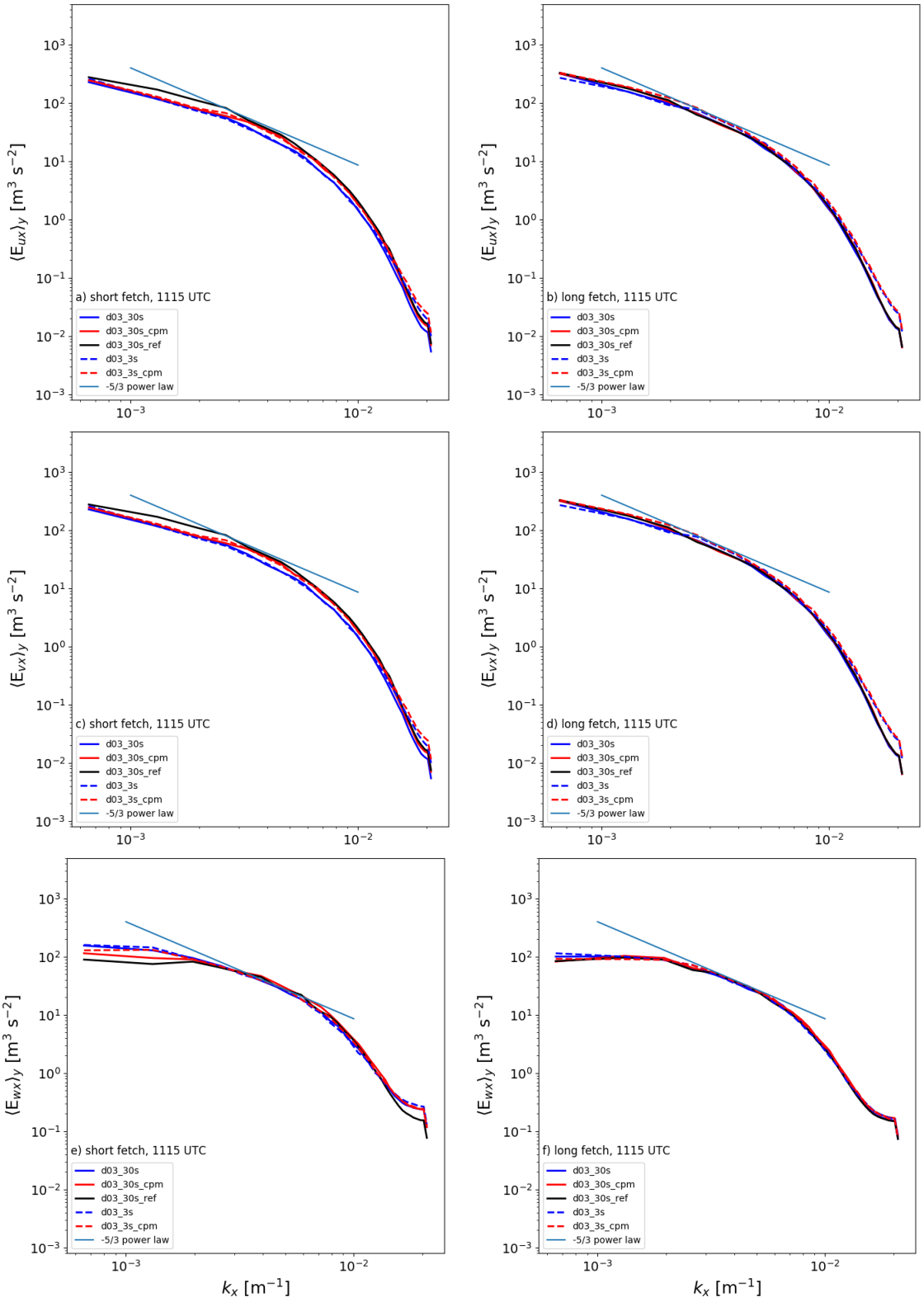

Figure 3.15: As in Figure 3.12 but for the nominal time, 1115 UTC, roughly concurrent with the 1113 radiosonde release on 20 May 2017.

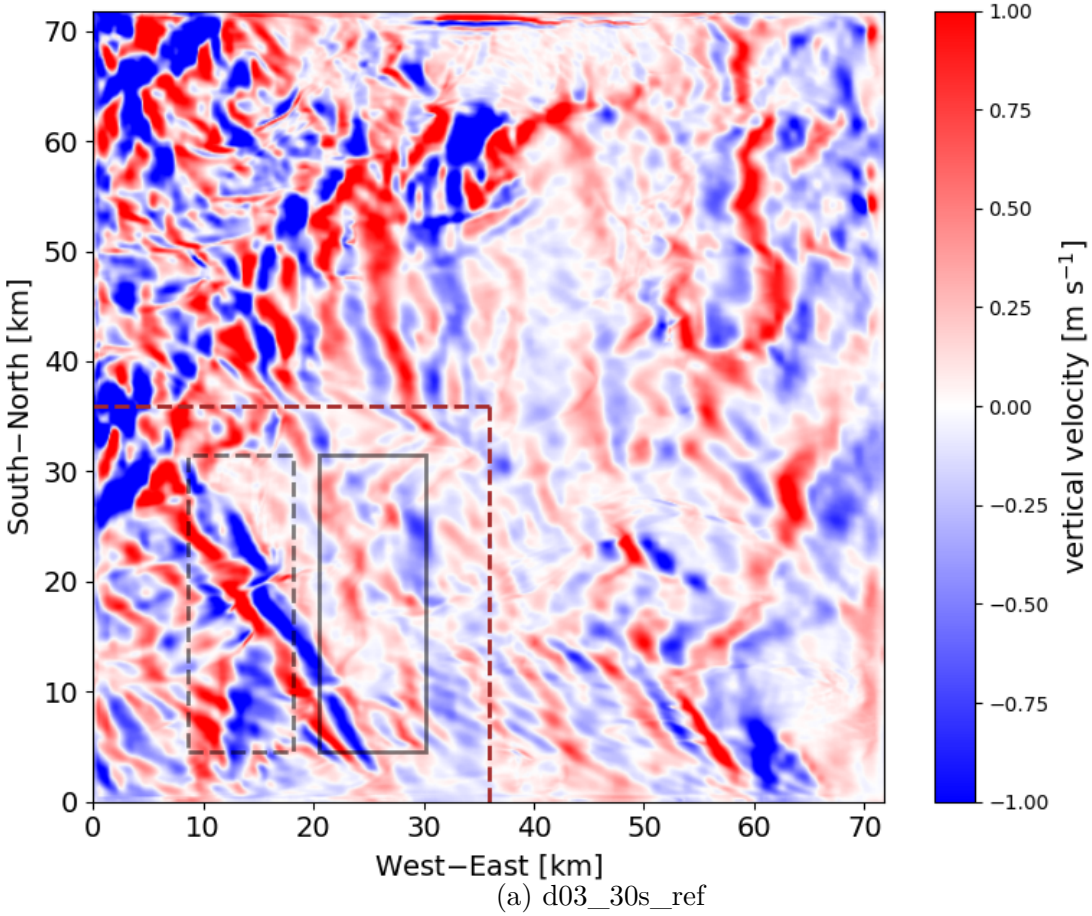

(a) d03_30s_ref

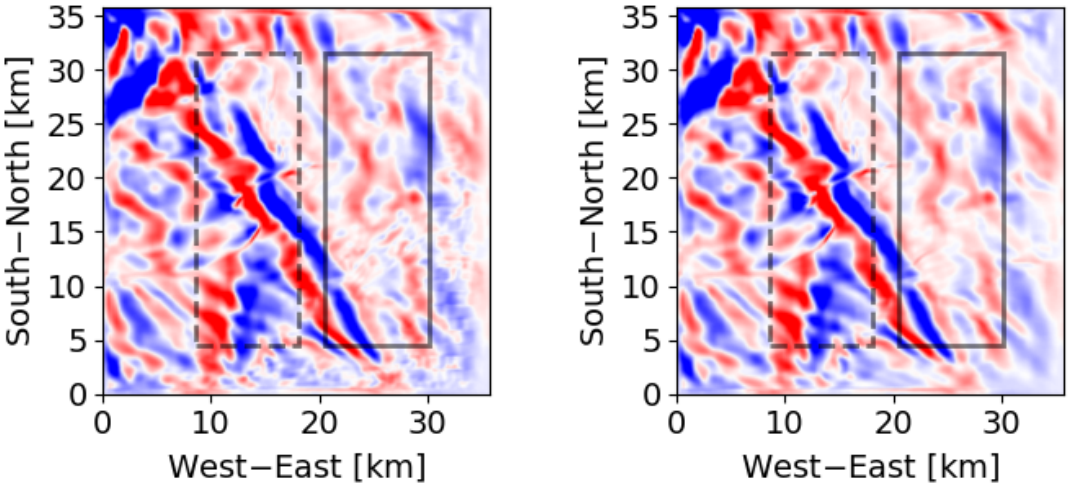

(b) d03_30s_cpm

(c) d03_30s

Figure 3.16: As in Figure 3.9 but at 2315 UTC 21 May 2017.

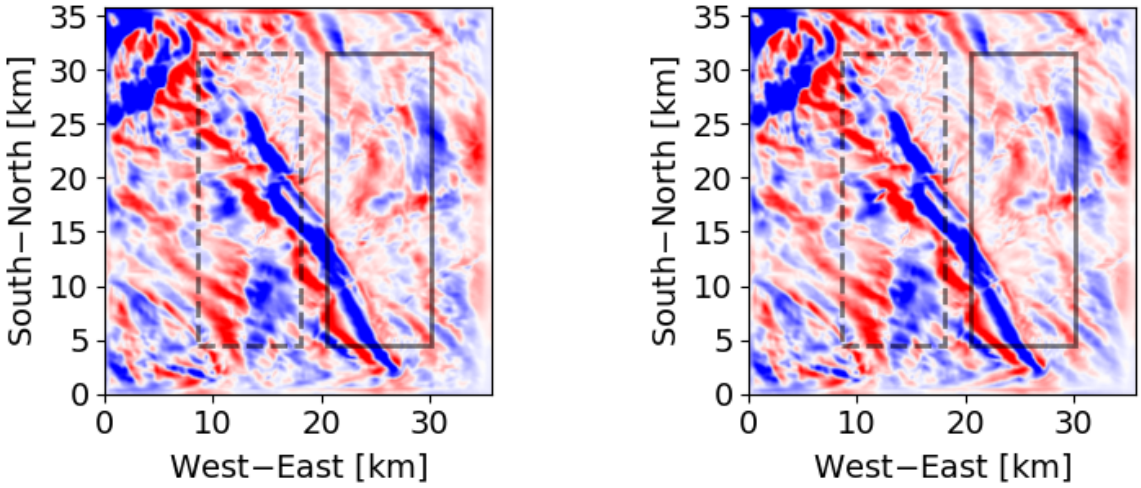

(a) d03_3s_cpm (b) d03_3s

Figure 3.17: As in Figure 3.16b and Figure 3.16c but for simulations with 3 arcsec topography input.

are examined for real case simulations with highly complex terrain conditions. The results indicate that CPM is particularly helpful during certain time periods and has an overall positive impact on the solution. The use of higher resolution topography is also explored as a way to develop more realistic turbulence in the nested simulations, in addition to improvements made from applying the CPM.

Nested simulations with and without CPM are performed over the site of the Perdigão field campaign and are compared to a reference simulation with a larger domain. Even with complex terrain, all simulations during convective conditions show spurious streaky structures near the inflow boundaries which persist over a large fraction of the domain. In the simulations without CPM, these spurious structures break down into finer scale turbulence after ≈10–20 km of fetch. This distance is less than the typical distances reported (as much as 54 km of fetch) for flat terrain cases (Mirocha et al. 2013, 2014; Muñoz-Esparza et al. 2014, 2015; Muñoz-Esparza and Kosović 2018), but is nonetheless a significant portion of the domain which is lost to spurious flow features. Using CPM shortens the fetch required for turbulence to fully develop. As an example, the fetch required to develop turbulence at 1715 UTC (Figure 3.9) was reduced from 16 km to 6 km using CPM. This recovery of over 27% of the entire domain size is achieved through CPM with negligible computational cost. If a larger reference simulation were used instead to generate the same level of turbulence, as illustrated with d03_30s_ref, it could require ∼5 times more CPU-hours than a smaller domain using CPM.

Unlike CPM, the use of more finely resolved model topography does not generally accelerate the generation of the fine-scale turbulence desired on the inner domain. Refining the topography can increase energy in the spectral densities of velocity, but this effect is

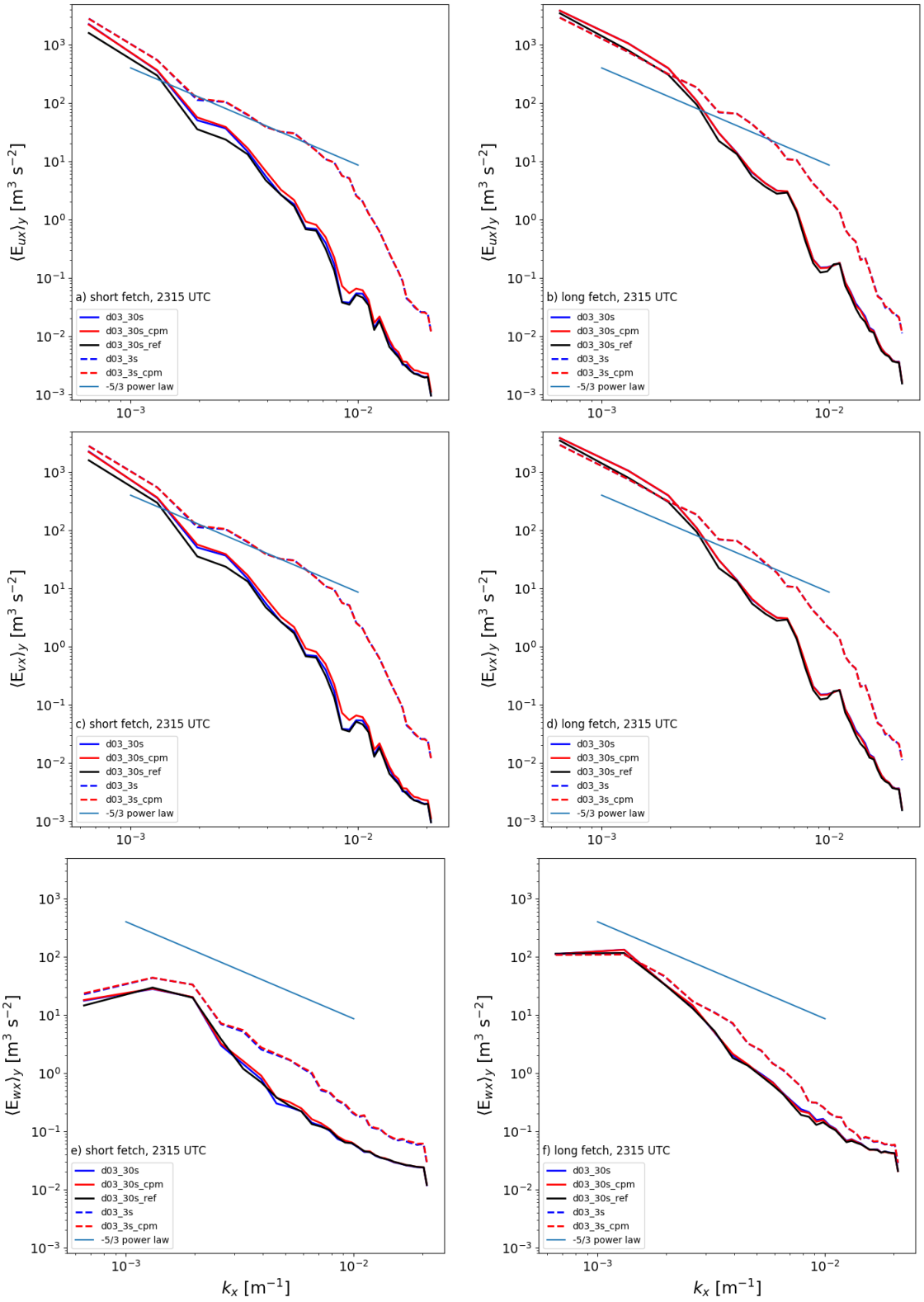

Figure 3.18: As in Figure 3.12 but for the nominal time, 2315 UTC, roughly concurrent with the 2313 radiosonde release on 20 May 2017.

most notable under the weakly stable stratification and is not apparent during sufficiently strong convective conditions. For the weakly convective conditions, for example, increasing the topography resolution is not sufficient for fully developing turbulence on the inner domain after 40 points, or 6 km, of fetch. Application of CPM at this time, regardless of topography resolution, leads to agreement with the reference simulation at the same location. The longest fetches required to fully develop the energy spectra occur during this weakly convective time period and therefore set a minimum domain size for simulations that might include a full diurnal cycle. CPM has more impact than high-resolution topography on turbulent structures during this weakly convective time, making CPM much more cost effective. Furthermore, while there are of course important reasons to implement more finely resolved topography whenever possible, e.g. to resolve a narrow valley such as the Vale do Cabrão, greater benefits are found from implementing the CPM at the same time.

The influence of the CPM is found to depend on the time of day, which reflects a dependence on atmospheric stability. For the convective cases, this dependence is characterized by a ratio of a characteristic wind speed and a convective velocity scale, U_{ci}/w_* (Muñoz-Esparza and Kosović 2018). The benefits of CPM are made most clear under weakly convective conditions, such as at 1715 UTC, when U_{ci}/w_*=7 as discussed above. At this time, the simulations using CPM have greater turbulent energy than simulations without CPM which are missing energy compared to the reference simulation. During more strongly convective conditions, at 1115 UTC, the effect of CPM is less pronounced when $U_{ci}/w_* \lesssim 3$, which closely agrees with previous reports by Muñoz-Esparza and Kosović (2018). At this time, all simulations develop turbulence and spectra resembling those from the reference simulation soon after the inflow boundary. The combined effects of convection and heterogeneous topography may render CPM unnecessary during these strongly convective conditions (as noted by Rai et al. 2017). With weak stability, such as at 2315 UTC, the use of finer topography resolution seems to be more significant than CPM in generating finer scale structures as seen in the model energy spectra. The stable simulation period would possibly benefit from transition to the Richardson's number based CPM approach (Muñoz-Esparza and Kosović 2018), and more likely from even finer model resolution. Extending the current multiscale approach, additional nests with finer resolved grid meshes should be used for even weakly stable conditions. As finer resolved models would be nested within simulations resembling the coarse LES presented here, there is a practical interest in reducing spurious information on these intermediate coarse domains. We have shown that use of higher resolution topography is a means to increase energy found in velocity spectra in the current complex terrain case, though finer nests are likely to benefit from the application of CPM, as in Arthur et al. (2020). Since the current work does not pursue these finer nests, the role of CPM under stable conditions with complex terrain needs further investigation.

In conclusion, using CPM during the entire simulation period can lead to improvement during certain conditions (e.g. weakly convective) and does not have any detrimental effects during other times of day. Looking forward, applications like wind energy that rely on weather forecasting will continue to increase in resolution in response to increasing computational power. Eventually, simulations that can resolve narrow valleys and even turbine

wakes, like those of interest to the Perdigão project, will be nested in simulations such as those presented in the current work. As shown here, the CPM is a cost-effective method to generate realistic turbulence without requiring very large domains to provide excessively large fetches from inflow boundaries. Under the appropriate conditions, the benefits of CPM are substantial even over complex, heterogeneous terrain. With essentially no drawbacks in computational cost or the quality of the developed flow, CPM is a promising method for maintaining low fetches and improving the representation of turbulence in future nested simulations.

Chapter 4

Analytical and Semi-ideal Numerical Models of Drainage Flow

4.1 Introduction

In the previous chapter, we investigated a novel method for turbulence generation which mitigates the burden of the high computational cost of large-eddy simulation. This is a welcome development after errors in the first chapter could not be addressed without incurring prohibitively large computational costs. In part this was explained by a novel stability limit for simulations using terrain-following coordinate systems over steep terrain. Recall, the investigation into the stability limit was motivated by a warm bias in a cold-air pool which we attributed to unresolved drainage flows at the Granite Peak site.

In this chapter, we begin with the fundamentals of these drainage flows and their analytical solutions, first presented by Prandtl (1942). While the Prandtl solution is helpful to build intuition on drainage flow dynamics at steady state, it does not address the development of drainage flows. In the classic Prandtl solution, a negative temperature perturbation is prescribed as a Dirichlet boundary condition. In reality, the temperature of the surface is determined by an energy budget that is externally forced by the sun's radiation. As such, we may expect the transient solution of drainage flows to depend on the pattern of the sun's radiation.

Studies of these dynamics have been performed in the Weather Research and Forecasting (WRF) model for a real weather case at Granite Peak (Arthur et al. 2018), but fundamental relationships are difficult to discern from such simulations. In real terrain simulations, even simple parameters required for comparison to analytical solutions, e.g. the slope angle, are not entirely unambiguous. To avoid this ambiguity, semi-ideal simulations are performed with a simple terrain geometry here. This semi-ideal model allows for transient solutions to be obtained with large-eddy simulation (LES). Differences between the numerical and previous analytical models are found to be associated with the surface boundary condition. A new analytical solution is also derived which explains the dependence of the wind velocity maximum on the slope angle observed in the LES and retains the same simplicity of the classic Prandtl solution to drainage flow.

4.2 Background

Governing equations of drainage flows

When heated or cooled over sloped terrain, near-ground parcels of air will travel upslope or downslope, respectively. In the case of expansion from heating, the resulting uphill flow is called anabatic, Greek for going upslope. Similarly, when cooled air sinks, we call the flow katabatic from the Greek for going downslope. Over real topography, a diurnal cycle of anabatic and katabatic slope flow follows the solar cycle of insolation (Zardi and Whiteman 2013). Generally, katabatic winds are more difficult to model because they are accompanied by stable background stratification, confining the flow closer to the surface than in the anabatic case (Smith and Porté-Agel 2014). Also due to stability, katabatic flows are more

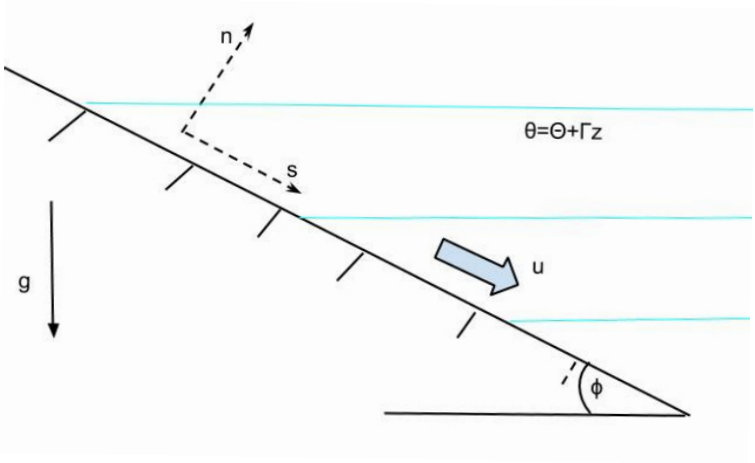

Figure 4.1: Illustration of rotated coordinates and variables used for Prandtl's analytic solution to drainage flow

often important in air quality applications, e.g. a cold-air pool persisting in a basin (Lareau et al. 2013). The study of glacial weather is also more concerned with katabatic than with anabatic winds. Indeed, recently increased attention to glacial wind systems have shifted the connotations of the term 'katabatic' to refer exclusively to these flows over glaciers. To avoid this confusion, we will use 'drainage flow' as a general term for buoyancy driven, downslope flow.

Ludwig Prandtl (1942) presented and solved the equations governing a drainage flow in the simplest possible geometry, shown in Figure 4.1. For convenience, axes are rotated normal to the slope, n, and pointing downslope, s, parallel to the land's surface which is inclined at an angle, ϕ. With these coordinates, elevation is

$$z = n\cos\phi - s\sin\phi. \tag{4.1}$$

The incline is considered infinite, so all variations into and out of the page may be ignored. Further, the temperature perturbation, $\theta^{'}(n)$, varies only with n assuming fully developed flow in s for long slopes. Given a stable background profile with positive lapse rate, Γ, the potential temperature field is

$$\theta = \theta_0 + \Gamma z + \theta^{'}(n) \tag{4.2}$$

$$\theta = \theta_0 + \Gamma(n\cos\phi - s\sin\phi) + \theta^{'}(n). \tag{4.3}$$

The time evolution of temperature is governed by a transport equation in these rotated coordinates. Neglecting less significant physical terms such as radiative divergence, we are left with only turbulent fluxes, J_i:

$$\frac{D\theta}{Dt} = -\frac{\partial J_i}{\partial x_i}. \tag{4.4}$$

$$\frac{\partial \theta}{\partial t} + u\frac{\partial \theta}{\partial s} + w\frac{\partial \theta}{\partial n} = -\frac{\partial J_i}{\partial x_i} \tag{4.5}$$

From intuition or more rigorous scaling, we argue that $w << u$ and neglect vertical advection. Further simplifications are made by assuming steady state, so only downslope advection is present in the material derivative,

$$u\frac{\partial \theta}{\partial s} = -\frac{\partial J_i}{\partial x_i}. \tag{4.6}$$

Prandtl models the turbulent fluxes using a constant eddy diffusivity, $J_i = -K_H \frac{\partial \theta}{\partial x_i}$, for

$$u\frac{\partial \theta}{\partial s} = K_H \left(\frac{\partial^2 \theta}{\partial n^2} + \frac{\partial^2 \theta}{\partial s^2} \right). \tag{4.7}$$

$$u\frac{\partial \theta}{\partial s} = K_H \left(\frac{\partial^2 [\theta_0 + \Gamma z + \theta^{'}(n)]}{\partial n^2} + \frac{\partial^2 [\theta_0 + \Gamma z + \theta^{'}(n)]}{\partial s^2} \right) \tag{4.8}$$

$$u\frac{\partial \theta}{\partial s} = K_H \frac{\partial^2 \theta^{'}}{\partial n^2}. \tag{4.9}$$

Note, all non-linear variations of θ given by equation 4.3 are contained in the $\theta^{'}(n)$ term such that the RHS is now in terms of temperature perturbation rather than temperature itself. Finally, the LHS above can be evaluated by taking the s derivative of (4.3), $\frac{\partial \theta}{\partial s} = -\Gamma \sin\phi$. Thus, the final form of the internal energy equation is

$$-u\Gamma \sin\phi = K_H \frac{\partial^2 \theta^{'}}{\partial n^2}\ . \tag{4.10}$$

Turning attention to the momentum equation, we retain the assumptions of steady flow, fully developed in the downslope. Further assuming no external pressure gradient and neglecting the hydrostatic contribution in s, fine for angles less than 10 degrees (Grisogono and Axelsen 2012), the momentum equations are reduced to a balance between turbulent diffusion of momentum and buoyancy forcing. Turbulent diffusion is modeled by a constant eddy viscosity model similar to that used above in the internal energy equation. Briefly,

$$\frac{Du}{Dt} = \frac{-1}{\rho}\frac{\partial p}{\partial s} + K_M \frac{\partial^2 u}{\partial x_j x_j} + f_b \tag{4.11}$$

$$0 = \quad 0 + K_M \frac{\partial^2 u}{\partial n^2} + f_b \tag{4.12}$$

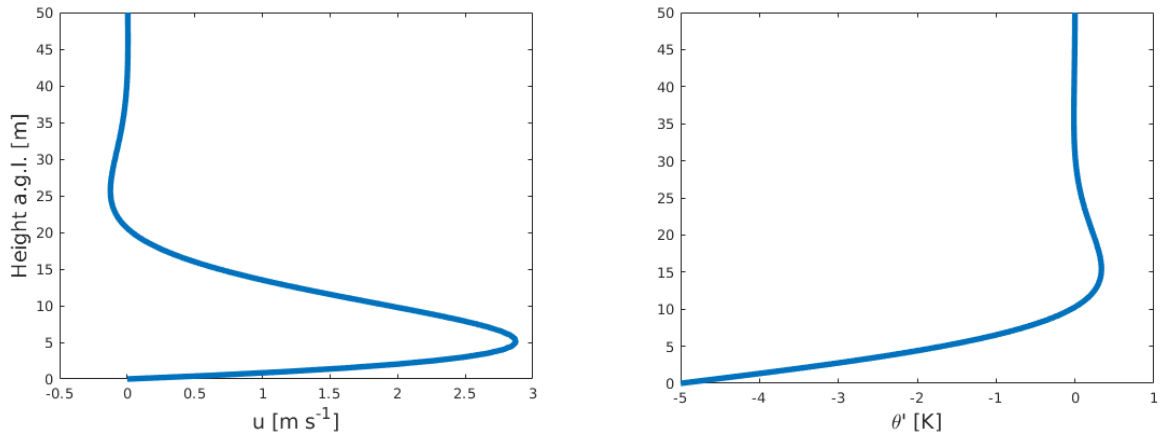

Figure 4.2: Prandtl's analytical solution to drainage flows taking $\theta_0^{'}$ =-5 K, ϕ =3°, θ_0 =308 K, Γ =0.02 K m^{-1}, K_M =0.02 m^2 s^{-1}, K_H =0.04 m^2 s^{-1}, and g =9.8 m s^2 to approximate values found in a semi-ideal WRF simulation.

The upward acceleration due to buoyancy is given by Archimedes' Principle. We make the additional assumption that the variability associated with $\theta^{'}$ is greater than that of the environmental lapse rate. That is, $\theta_{env} \approx \theta_0$ when centering the analysis at $s = 0$, an arbitrary location on the hill which determines the value of θ_0. Then, buoyant acceleration is only a function of temperature perturbation

$$f_{b,z} \approx g \frac{\theta^{'}}{\theta_0}. \tag{4.13}$$

Taking the s-direction component of this buoyant acceleration, multiplying by $-\sin\phi$, the force balance is

$$0 = K_M \frac{\partial^2 u}{\partial n^2} - \frac{g \sin\phi}{\theta_0}\theta' \tag{4.14}$$

Finally, we have a system of governing equations

$$\begin{cases} K_H \dfrac{\partial^2 \theta^{'}}{\partial n^2} + u\Gamma \sin\phi = 0 & (4.15) \\ K_M \dfrac{\partial^2 u}{\partial n^2} - \dfrac{g \sin\phi}{\theta_0}\theta' = 0 & (4.16) \end{cases}$$

The Prandtl Solution

In the classic Prandtl solution, Dirichlet boundary conditions are enforced. The temperature of air at the surface is expected to be in thermal equilibrium with the land surface. Then, for katabatic flow, a negative temperature perturbation is assigned at the bottom boundary. No

slip is enforced at the surface. In the far field, both velocity and temperature perturbation go to zero. Mathematically,

$$\begin{cases} u(n=0) = 0 & (4.17) \\ \theta^{'}(n=0) = \theta_{\text{surface}} - \theta_0 = \theta_0^{'} & (4.18) \\ u(n \to \infty) = 0 & (4.19) \\ \theta^{'}(n \to \infty) = 0 & (4.20) \end{cases}$$

define the solutions to the governing differential equations uniquely.

The system of equations may be solved by differentiating either (4.15) or (4.16) twice with respect to n to substitute into the other equation and obtain a fourth-order, linear ordinary differential equation. Such equations can be solved with standard techniques and always have the form of a linear combination of complex exponentials. The solutions below satisfy (4.15)-(4.20) while example profiles are shown in Figure 4.2.

$$u = -\theta_0^{'} \left(\frac{gK_H}{\theta_0 \Gamma K_M} \right)^{\frac{1}{2}} \exp\left[-\left(\frac{g\Gamma \sin^2\phi}{4\theta_0 K_M K_H} \right)^{\frac{1}{4}} n \right] \sin\left[\left(\frac{g\Gamma \sin^2\phi}{4\theta_0 K_M K_H} \right)^{\frac{1}{4}} n \right] \tag{4.21}$$

$$\theta^{'} = \theta_0^{'} \exp\left[-\left(\frac{g\Gamma \sin^2\phi}{4\theta_0 K_M K_H} \right)^{\frac{1}{4}} n \right] \cos\left[\left(\frac{g\Gamma \sin^2\phi}{4\theta_0 K_M K_H} \right)^{\frac{1}{4}} n \right] \tag{4.22}$$

We note the effect of the cold ground is confined to a relatively shallow layer. We take the location of the first maximum above the surface, n_{JH}, as a characteristic height for this shallow flow such that $u\left(n_{JH}\right) = u_{max}$. From 4.21, we obtain

$$n_{JH} = \frac{\pi}{4} \left(\frac{g\Gamma \sin^2\phi}{4\theta_0 K_M K_H} \right)^{\frac{-1}{4}} \tag{4.23}$$

$$u_{max} = -\theta_0^{'} \left(\frac{gK_H}{\theta_0 \Gamma K_M} \right)^{\frac{1}{2}} e^{-\frac{\pi}{4}} \frac{\sqrt{2}}{2}. \tag{4.24}$$

When these results are compared to field observation, we find the values of n_{JH} and u_{max} predicted by Prandtl are often too large (Axelsen and Dop 2009a). Physical effects neglected by the Prandtl model lead to yet shallower and weaker katabatic flow. One possibility is the variability of eddy diffusivity, which is assumed to be constant in the Prandtl solution. Before attempting the variable diffusivity case, with much more involved mathematics, it is convenient to note an abbreviated form of the Prandtl solution:

$$F = exp[-(1+i)\sigma\, n] \tag{4.25}$$

$$u = \theta_0^{'}\, \mu\, Im(F) \tag{4.26}$$

$$\theta^{'} = \theta_0^{'}\, Re(F) \tag{4.27}$$

where

$$\sigma = \left(\frac{g\Gamma \sin^2 \phi}{4\theta_0 K_M K_H} \right)^{\frac{1}{4}} \tag{4.28}$$

$$\mu = \left(\frac{g K_H}{\theta_0 \Gamma K_M} \right)^{\frac{1}{2}} \tag{4.29}$$

The Grisogono & Oerlemans Solution

Grisogono and Oerlemans (2001) consider katabatic flow modeled with variable eddy diffusivities and employ the Wentzel–Kramers–Brillouin (WKB) method for approximate solutions to linear partial differential equations. The WKB method is limited to cases where diffusivities change only gradually and are prescribed functions of n, distance from the surface. We also require the diffusivities for velocity and temperature to have the same functional form for a constant Prandtl number. With these restrictions, the governing equations are

$$\begin{cases} 0 = \dfrac{\partial}{\partial n} \left[K_H(n) \dfrac{\partial \theta'}{\partial n} \right] + u\Gamma \sin \phi & (4.30) \\ 0 = \dfrac{\partial}{\partial n} \left[K_M(n) \dfrac{\partial u}{\partial n} \right] - \dfrac{g \sin \phi}{\theta_0} \theta' & (4.31) \end{cases}$$

which resemble the governing equations in the Prandtl model, 4.15 and 4.16, but with more sophisticated diffusion terms. Further, the WKB solution below resembles the Prandtl solution in complex form (Eqns. 4.25–4.29),

$$F = exp \left[-(1+i) \left(\sigma_0 / 2 \right)^{-1/2} \int_0^n K_H^{-\frac{1}{2}}(n')\, dn' \right] \tag{4.32}$$

$$u = \theta_0' \, \mu \, Im(F) \tag{4.33}$$

$$\theta' = \theta_0' \, Re(F) \tag{4.34}$$

$$\tag{4.35}$$

where

$$\sigma_0^2 = \frac{g\Gamma \sin^2 \phi}{\theta_0 Pr} \; ; \; Pr = \frac{K_M}{K_H} \tag{4.36}$$

$$\mu = \left(\frac{g K_H}{\theta_0 \Gamma K_M} \right)^{\frac{1}{2}} \tag{4.37}$$

$$\tag{4.38}$$

This solution is valid only near the surface, though Grisogono and Oerlemans (2001) also give an outer solution which is omitted here. Here, we take

$$K_H = C \, n \, exp \left[\frac{-n^2}{2h^2} \right] \tag{4.39}$$

$$\tag{4.40}$$

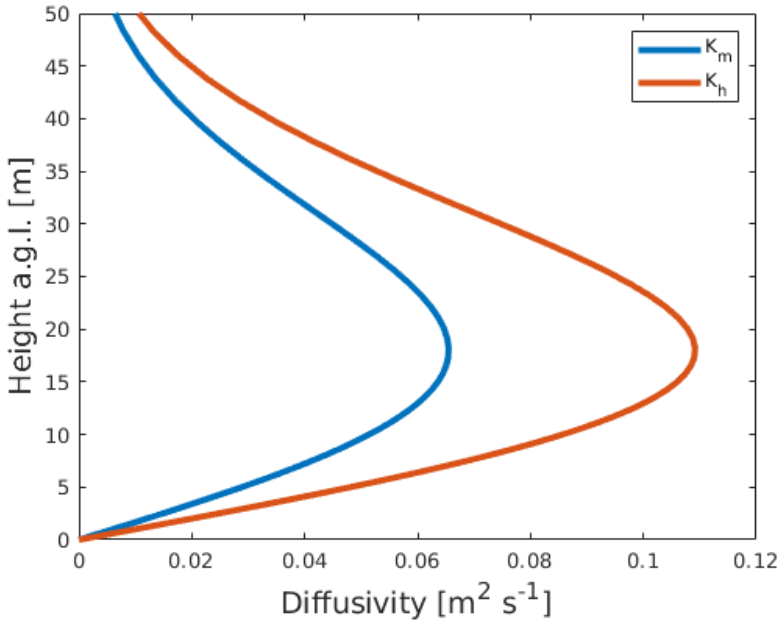

Figure 4.3: Diffusivity profiles for K_H using the functional form in the text with $C = 0.01$ m s^{-2} and $h = 18$ m alongside K_M calculated assuming $Pr = 0.6$ to approximate values found in a semi-ideal WRF simulation.

with $C = 0.01$ m s^{-2} and $h = 18$ m. A thermal diffusivity profile with this functional form is plotted in 4.3 along with the eddy diffusivity using $Pr = 0.6$, and the resulting WKB inner solution is shown in Figure 4.4.

In comparison to the Prandtl solution (Figure 4.2), gradients near the ground are much sharper in the variable diffusivity case (Figure 4.4). Though maximum velocities are roughly equal to those in the Prandtl solution, the jet height is considerably shallower. In this sense, the Grisogono and Oerlemans solutions compare better to certain observations (Axelsen and Dop 2009a) than the Prandtl solutions at the cost of added complexity to the model in using variable eddy diffusivities, which of course more closely mirrors reality.

Representation of turbulent diffusion is not the only way complexity can be added to the original Prandtl model. The form of the surface boundary condition is also arguably oversimplified in the Prandtl solution. In the most advanced contemporary weather models, the boundary condition is usually formulated in terms of fluxes. Details on this form of these boundary conditions are presented in Appendix A. In the following section, we describe a state-of-the-art numerical weather prediction model which employs these sophisticated forms of surface boundary conditions. Later, further analytical work is presented in which simpler forms of flux boundary conditions are used. As we will see, certain behavior related to the flow's dependence on slope can be explained with this simple analytical model.

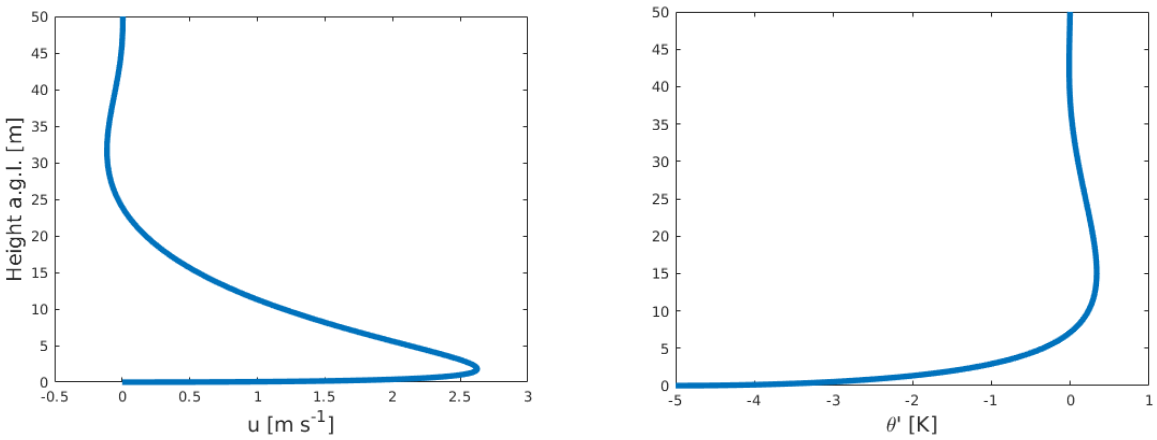

Figure 4.4: Grisogono and Oerlemans solution of katabatic flow obtained by the WKB method with $\theta_0^{'}$ =-5 K, ϕ =3°, θ_0 =308 K, Γ =0.02 K m^{-1}, g =9.8 m s^2, Pr=0.6, and K_H taking the functional form given in the body text to approximate values found in a semi-ideal WRF simulation.

Table 4.1: Information on WRF simulations. All simulations have the same horizontal grid spacing, $\Delta x = \Delta y = 50$ m, and domain size with 400 points in the x-direction and 150 points in the y-direction. The staggered grid leads to the mountain peak at $x_{\text{mid}} = 9975$ m. Slopes and lengths vary together so that $h(x_{\text{mid}}) = 245$ m in all simulations. Though the heights of the pressure coordinates evolve in time, every simulation uses roughly the same vertical grid spacing, ranging from 3 m near the bottom surface, where the first velocity points are calculated at 1.5 m a.g.l. due to grid staggering, to 530 m at the 12 km model top, over 69 vertical levels. All simulations use $\Delta t = 0.2$ s.

Simulation	ϕ_1[°]	L_1 [m]	ϕ_2[°]	L_2 [km]	Soil Mois. m^3 m^{-3}
LES2	2	4.502	5	1	0.0868
LES3	3	3	5	1	0.0868
LES4	4	2.248	5	1	0.0868
DRY3	3	3	5	1	0.0434

4.3 Numerical model setup

Weather Research and Forecasting Model

Simulations described in this section use the Weather Research and Forecasting (WRF) model version 3.9.1.1 (Skamarock et al. 2008) developed by the National Center for Atmospheric Research (NCAR). The dynamic core of the model provides a numerical solution of the compressible flow equations with a third-order Runge–Kutta time advancement scheme, with split time stepping to handle acoustic modes, as well as fifth-order horizontal advection

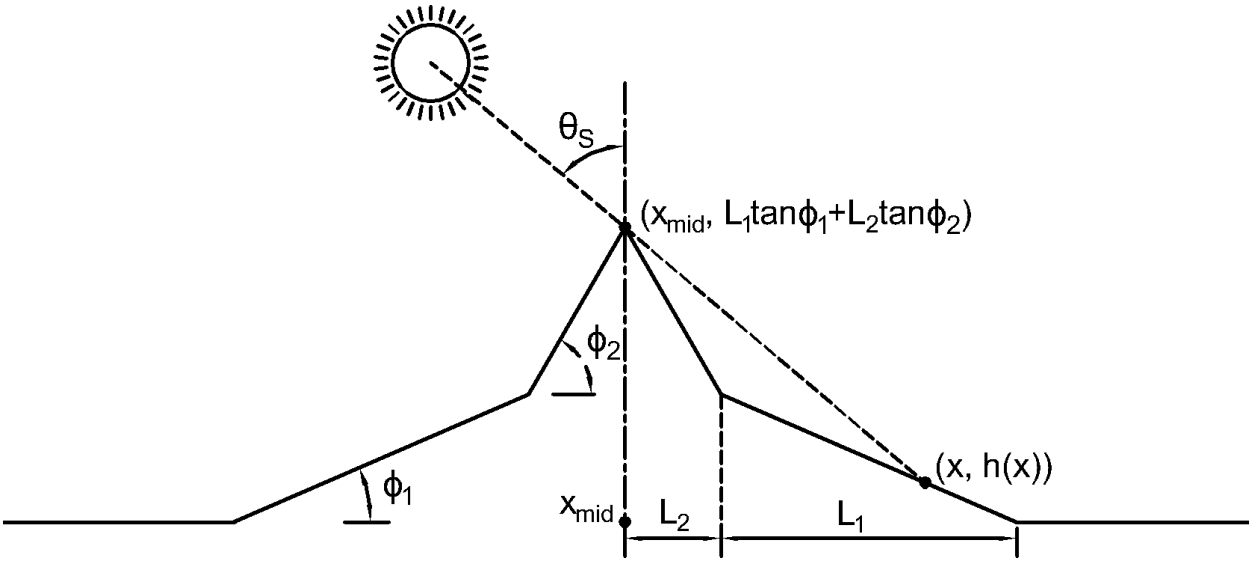

Figure 4.5: Illustration of the simple two-slope mountain.

and third-order vertical advection. Various configurations are run with different idealized model topography. Further details for each simulation are given in Table 4.1. All simulations use a Turbulent Kinetic Energy (TKE) 1.5 LES turbulence closure (Deardorff 1980) coupled with a surface-layer parameterization based on Monin–Obukhov similarity theory, the MM5 (option 1 in WRF namelist) scheme (Chen et al. 1997). Grid spacing is uniform in the horizontal directions with $\Delta x = \Delta y = 50$ m, while the terrain-following vertical grid spacing is variable and stretches from 3 m near the surface to 530 m near the model top at 12 km above sea level.

Physical parameterizations employed in the current simulations include the Noah land surface model (Chen and Dudhia 2001), the Rapid Radiative Transfer Model for longwave radiation (Mlawer et al. 1997), the Dudhia shortwave radiation model (Dudhia 1989), and a topographic shading routine (Zängl 2005). The land cover in the model is savannah, corresponding to index 10 from the United States Geological Survey (USGS) classification. The albedo and emissivity are set to 0.2 and 0.92, respectively. A constant roughness length, $z_0 = 15$ cm, corresponds to the savannah land cover type. The soil type is everywhere sandy loam initialized with a volumetric water content of 0.0868 m m^{-1} in simulations, LES2, LES3, and LES4. Another simulation, DRY3, is run with soil moisture initialized to 0.0434 m m^{-1}, half that of the other simulations, to test the sensitivity of the model.

The shape of the ideal terrain is defined by each side having a long shallow slope followed by a shorter, steeper slope at the mountain peak. With this shape, shadows from the steeper slope will be cast onto the lower slope, which is long enough for flow to fully develop. When

defining these lengths and slopes as labeled in Figure 4.5, the terrain height is defined as

$$h\left(x;\phi_1,L_1,\phi_2,L_2\right)=\begin{cases}0 & |x-x_{\text{mid}}|\geq L_1+L_2\\ \tan\phi_1\left(L_1+L_2-|x-x_{\text{mid}}|\right) & L_2<|x-x_{\text{mid}}|<L_1+L_2\\ \tan\phi_1 L_1+\tan\phi_2\left(L_2-|x-x_{\text{mid}}|\right) & |x-x_{\text{mid}}|\leq L_2\end{cases} \tag{4.41}$$

where x_{mid} is the midpoint of the domain. The terrain function is continuous, but not everywhere differentiable.

The ridge is aligned South–North, so the shadow of the upper slope may be cast onto the lower slope at sunrise and sunset. The incident shortwave radiation flux is nearly constant in the South–North direction by locating the mountain on a fictitious landmass at 0° N, 0° W and by simulating insolation on the vernal equinox, 20 March 2014.

On this date, the LES are initialized at 12:00 LT (UTC+0) and analyzed from that time until the morning of the following day. Initial conditions are quiescent winds and a stable lapse rate of 3 K km^{-1} starting at 305 K at 25 m until a height of 12 km above sea level. The initial surface skin temperature is set to 310 K and initial humidity is set to 10 g kg^{-1} everywhere. Periodic boundary conditions are used along each boundary. Velocity and potential temperature are often averaged in the South–North direction such that variations due to resolved turbulence are averaged out so the solutions can be compared to the analytical models of the preceding sections.

4.4 Results and Discussion

Diurnal Cycle

The semi-ideal model recreates the general pattern of the diurnal cycle that is predicted by fundamental theory: anabatic flows during the day and katabatic flows during the night. Figure 4.6 shows the time evolution of x-direction velocity from the lowest model half-level averaged in the y-direction. At the beginning of the simulation period, on the east slope, $x - x_{\text{mid}} > 0$, this velocity is more often negative, representing upslope flow. Upslope flow is also present during these times on the western side, with opposite sign. For the first few hours of simulation, the presence of strong convection is evidenced by periods of low or reversed velocity due to turbulent fluctuations that occasionally counter this buoyant forcing. Later, these upslope flows transition to downslope flow on both sides of the mountain around 18:30 LT. At this time there are no sporadic periods of reversed flow, because the levels of turbulence are suppressed during the nocturnal period. This is apparent in the time series of wind direction as well, where the variability decreases significantly after the transition to downslope flow around 18:30 (Figure 4.7). There are however times of reversed flow (visible as thin red or blue streaks in the Hovmöller diagram) but these are due to the downslope flows from the opposite side of the mountain passing through the periodic boundary, an arguable shortcoming of the current model setup which is discussed in more detail below.

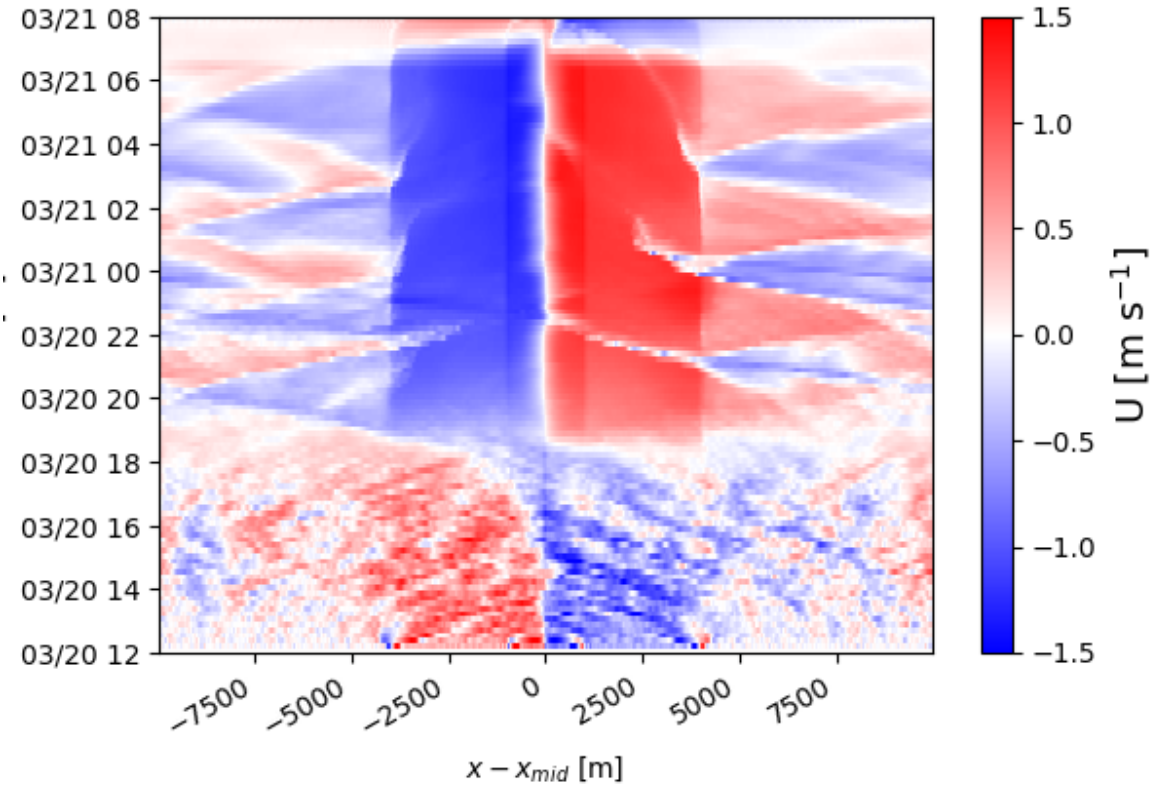

Figure 4.6: Hovmöller diagram of x-direction velocity at the first model half-level averaged in the South–North direction from LES3 for the entire simulation period.

After sunrise near the end of the simulation period, around 07:00, the signs of the slope flow are again reversed.

Onset of drainage flow

During the evening transition, a shadow is cast from the mountain peak onto the lower, eastern slope. A line can be drawn from the sun to the peak of the mountain and extended to another point on this section of the eastern slope, as drawn in Figure 4.5, which can be expressed in point-slope form as

$$[h(x) - h(x_{\text{mid}})] = -\cot\theta_s \, [x - x_{\text{mid}}] \, . \tag{4.42}$$

The intersection of this line and the line that defines the terrain represents the location of the shadow-front as it moves down the slope. Solving the linear system for this point results

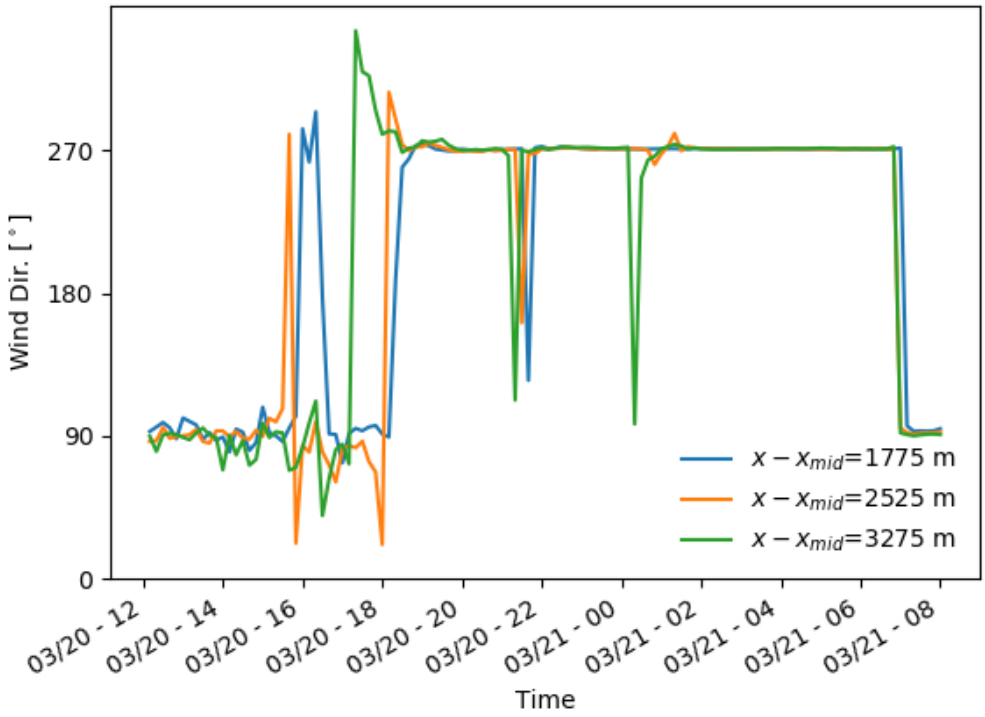

Figure 4.7: Time-series of wind direction at the first model half-level averaged in the South–North direction from LES3 over the entire simulation period for various distances along the lower slope of the eastern side of the mountain.

in a function of the solar angle,

$$\cot\theta_s = \tan\phi_1 + \frac{L_2}{x - x_{\text{mid}}}\left(\tan\phi_2 - \tan\phi_1\right). \tag{4.43}$$

In general,

$$\cos\theta_s = \sin\Phi\sin\delta + \cos\Phi\cos\delta\cos\eta \tag{4.44}$$

where Φ is the latitude, δ is the solar declination, and η is the hour angle. Considering the current choice to simulate the equator on the equinox, it follows that the solar angle is equivalent to the hour angle,

$$\theta_s = \eta = \frac{t - 12}{24} 2\pi \tag{4.45}$$

where t is in hours. With this substitution and application of a trigonometric identity for the inverse cotangent, we arrive at

$$t = 18 - \frac{12}{\pi}\arctan\left[\tan\phi_1 + \frac{L_2}{x - x_{\text{mid}}}\left(\tan\phi_2 - \tan\phi_1\right)\right]. \tag{4.46}$$

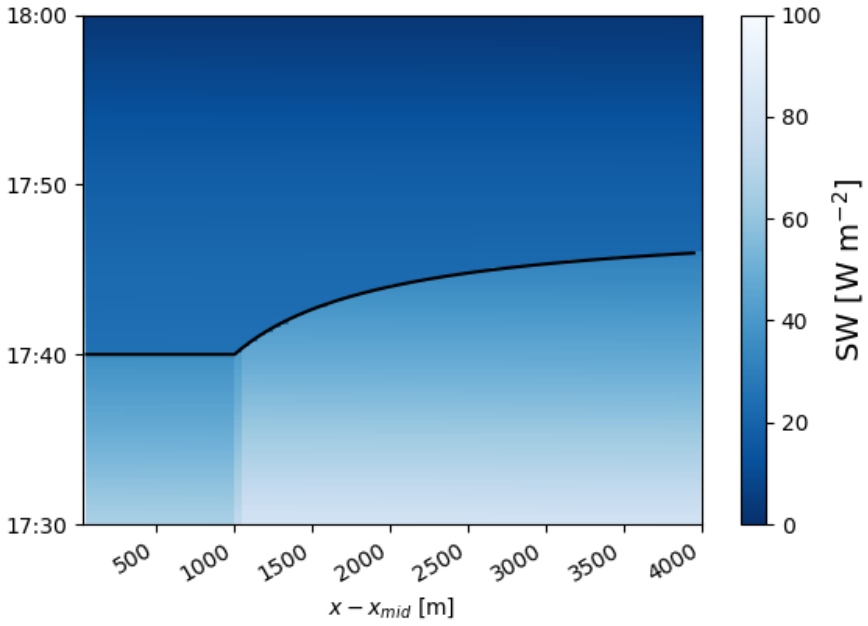

Figure 4.8: Hovmöller diagram of shortwave radiation incident on the terrain averaged in the South–North direction from LES3 for the half hour including local sunset on the eastern slope. Black line is the analytical result in Eqns. 4.46 and 4.47 for local sunset time as a function of distance.

This form expresses the time of local sunset as the equinox sunset time, 18, and an offset due to the terrain. A special case of note, taking $x - x_{\text{mid}} = L_2$, is also equal to the local sunset on the entire upper portion of the eastern slope, because the terrain line and the line traced back to the sun through the mountain peak are coincident for this case. With the slope angle expressed in radians,

$$t_{\text{upper slope}} = 18 - \frac{12}{\pi}\phi_2. \tag{4.47}$$

The analytical solution for the shadow front given by Eqns. 4.46 and 4.47 agrees quite well with model output, mainfested by a quick decrease in shortwave radiation incident on the terrain (Figure 4.8). The clear signal in radiation does not, however, translate to a clear signal in x-direction velocity for this setup during the same sunset time period (Fig 4.9). This differs from the experience of Arthur et al. (2018) in 3D simulations of the onset of drainage flows with the real terrain of Granite Peak, Utah. In those simulation, the onset of drainage flow was concurrent with or, at some locations on the slope, even preceded the shadow front. While downslope flows eventually develop after sunset in the current simulations (Fig 4.6), the transition is roughly an hour after the shadow completely encompasses the slope.

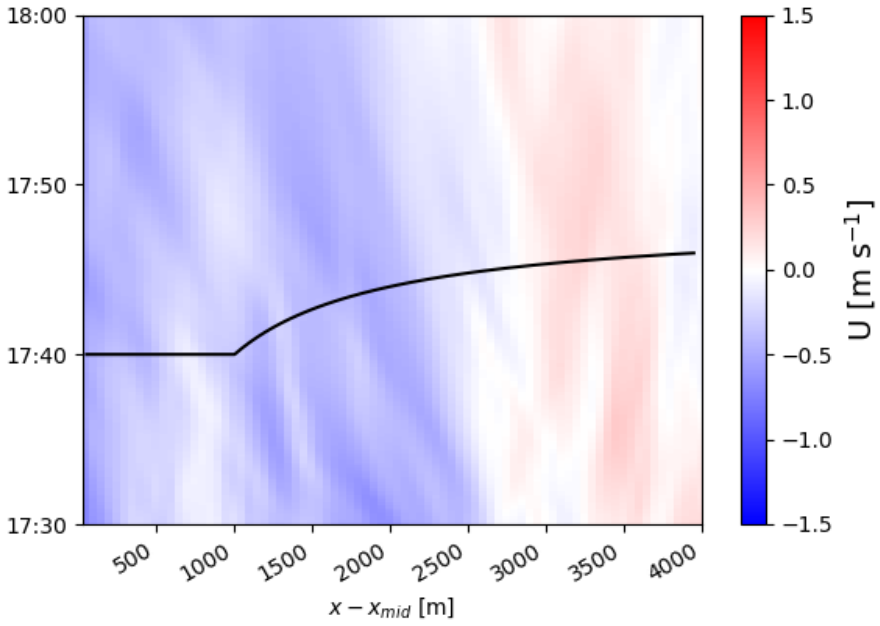

Figure 4.9: Hovmöller diagram of x-direction velocity averaged in the South–North direction from LES3 for the half hour including local sunset on the eastern slope. Black line is the analytical result in Eqns. 4.46 and 4.47 for local sunset time as a function of distance.

An important difference between the current ideal geometry and the real terrain used by Arthur et al. (2018) is the increased difference between slopes at the top of Granite Peak and at the foothills. A consequence of this difference in slopes is the duration of the sunset along the slopes. We can devise a metric for the duration of sunset as a function of the dimensionless group, $\frac{x-x_{\text{mid}}}{L_2}$, using Eqn. 4.46 and taking the difference in time for the shadow to reach $x - x_{\text{mid}} = L_2$ and $x - x_{\text{mid}} = 4L_2$. This metric is plotted in the ϕ_2–ϕ_1 parameter space in Figure 4.10 where the simulations presented here occupy the lower corner of this diagram, $\phi_2 = 5°$ and $\phi_1 \in \{2°, 3°, 4°\}$. Though the upper and lower slope is ambiguously defined for real terrain, we can take approximate values to estimate the duration of sunset on the shadow-cast slope. For Granite Peak, with $\phi_2 \approx 30°$ and $\phi_1 \approx 15°$, the theoretical values given in Figure 4.10 are roughly equal to the one-hour duration shown in Arthur et al. (2018) which coincides with the onset of drainage flows.

The quickness of the sunset in the current simulations, with similar angles for the upper and lower slopes, does not allow time for the convective systems that develop during the day time to sufficiently weaken for the drainage flows to develop concurrently with the shadow front propagation. This hypothesis is corroborated by vertical cross-sections of vertical velocity taken shortly before and after the shadow font is propagated along the eastern slope

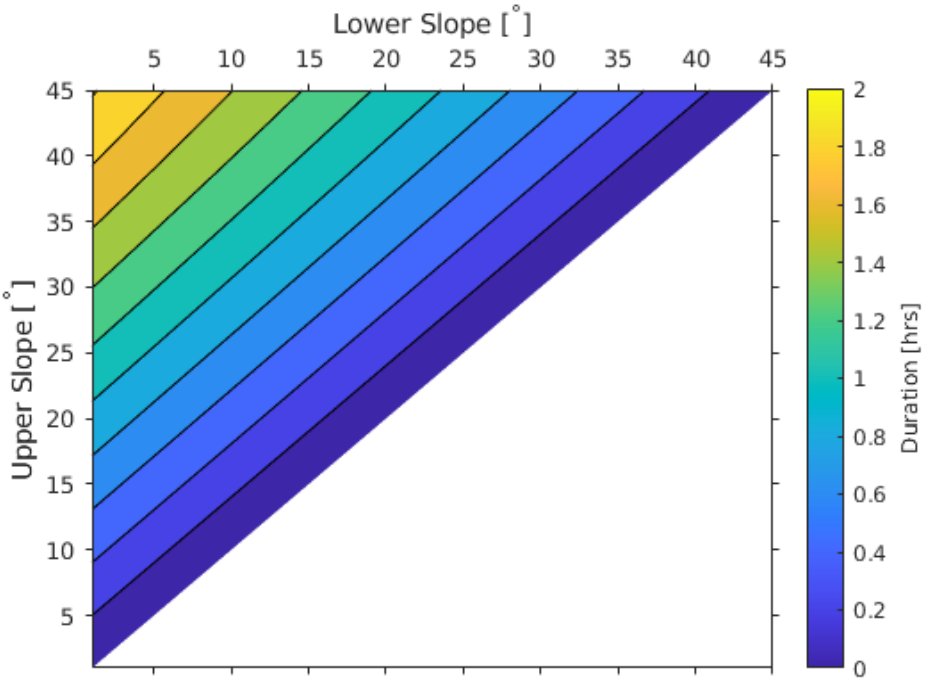

Figure 4.10: Duration of the shadow front propagation defined by the difference, $t(\frac{x-x_{\text{mid}}}{L_2} = 1) - t(\frac{x-x_{\text{mid}}}{L_2} = 4)$, using the function in Eqn. 4.46 and plotted as a function of upper slope and lower slope.

(Figure 4.12). We see that, though weakened after sunset, the same convective structures are present in similar locations as they were before sunset. The timescales related to the persistence of these convective structures is likely to be only weakly dependent on the slopes of the terrain. As such, future studies, even of real terrain cases similar to those of Arthur et al. (2018), can benefit from the theoretical results in Figure 4.10. The mapping of the slope parameter space to the sunset duration allows for insight on the relation between the shadow front and onset of drainage flows before any observed or modeled radiation data are analyzed. Specifically, for topography that results in sunset durations that are $\mathcal{O}$(1–10 min), one may expect the shadow front to precede the onset of downslope flow. Cases with longer durations, $\gtrsim$ 1 hr, are likely to see concurrent shadow front propagation and drainage flow onset, because the longer durations apparently allow time for the convective flow features to sufficiently weaken relative to the buoyancy forcing that drives drainage flow. The physics that determine the persistence of convective features are not known to be particularly sensitive to the slopes of the underlying terrain, though we have shown the duration of the shadow front propagation is primarily determined by the terrain shape. Of course, the effect of shadows directly influences only the radiation in the surface energy budget that determines the strength of the buoyancy forcing. Other important controls

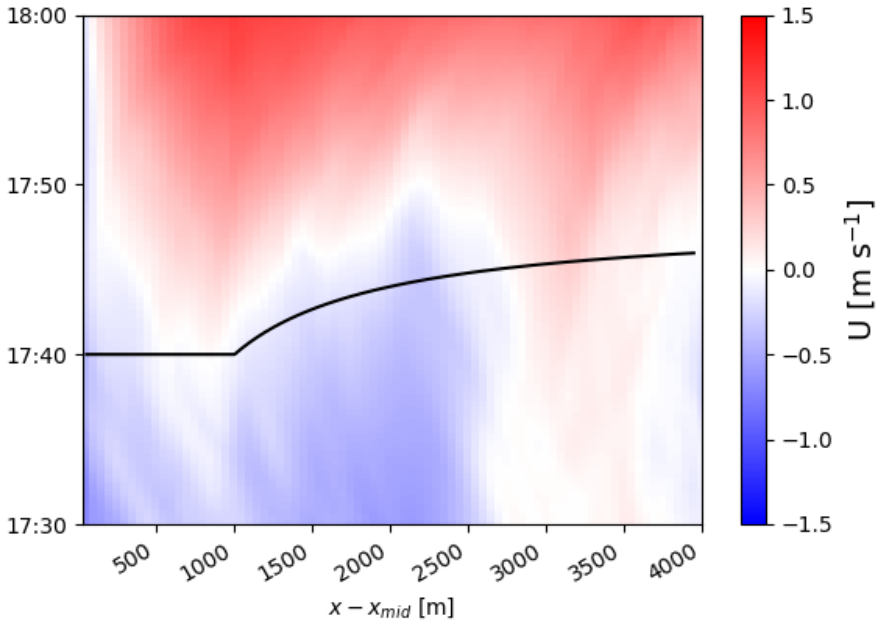

Figure 4.11: As in 4.9 but for the DRY3 simulation.

on the buoyancy forcing are the land and soil characteristic, as demonstrated by the more rapid onset seen in the DRY3 simulation, where the transition to downslope flow occurs less than 10 min after the shadow front passes (Figure 4.11). However, even the base case soil moisture used in the other simulations is already relatively low. We do not expect the soil moisture used in the drier simulation to be realistic enough to warrant further investigation in the current work. Further, even with these dry soils, the onset of downslope flow generally occurs after the shadow front reaches a given location on the slope. As such, the difference between LES3 and DRY3, which use the same terrain shape, are quantitative and do not rise to the qualitative difference as when comparing the current simulations to those of Arthur et al. (2018) that saw simultaneous shadow front propagation and drainage flow onset. Effects of the three-dimensional terrain considered by Arthur et al. (2018) may be one reason that onset is earlier in the case they consider at Granite Peak, where drainage flow can collect quickly in the narrow side valleys. Additionally, the lag between drainage flow onset and the rapid shadow front propagation in the DRY3 simulations is further evidence that the duration of the sunset is of primary importance. Still, future work is needed to more systematically investigate these timescales and the resulting force balance between the inertia of convective structures and buoyancy near the surface boundary with varied land cover and soil characteristics.

The presence of convective structures post-sunset has additional effects on the initial

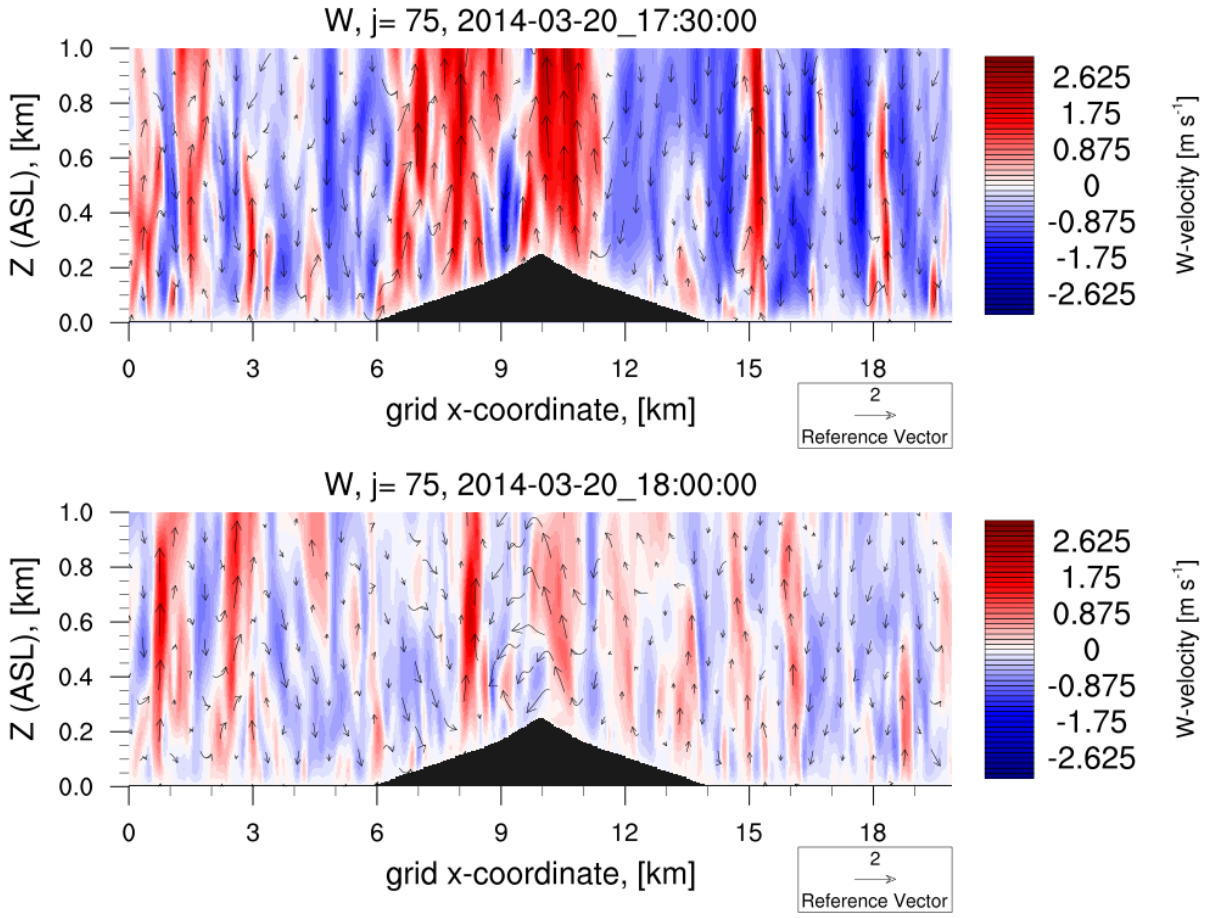

Figure 4.12: Vertical cross sections of vertical velocity along the centerline of the LES3, shortly before and after sunset on the western slope.

development of downslope flow. The results show that downslope flow initiates earlier on the sunnier western side than on the eastern slope. Because cooling by the surface boundary forces drainage flow, this result may be counterintuitive. Contours of the x-direction velocity suggest the earlier onset on the sunnier side of the mountain is also related to the presence of convective structures. In Figure 4.13, we see horizontal convergence on the western slope at 18:00 associated with the strong updraft near $x = 8.5$ km, also evident in the contours of vertical velocity from the same time (Figure 4.12). It is reasonable to expect this convective updraft to persist on the western side of the mountain because it receives insolation for longer than the shadowy eastern side does. Over the next hour, the easterly flow near the mountain peak enforces the downslope flow on the western slope while there is no similar forcing on the eastern slope. Thus, earlier and stronger downslope flow can occur on the side that receives insolation later in the evening. At 19:30 (Figure 4.14), both slopes show stronger, deeper downslope flows than are expected from buoyancy forcing alone. These

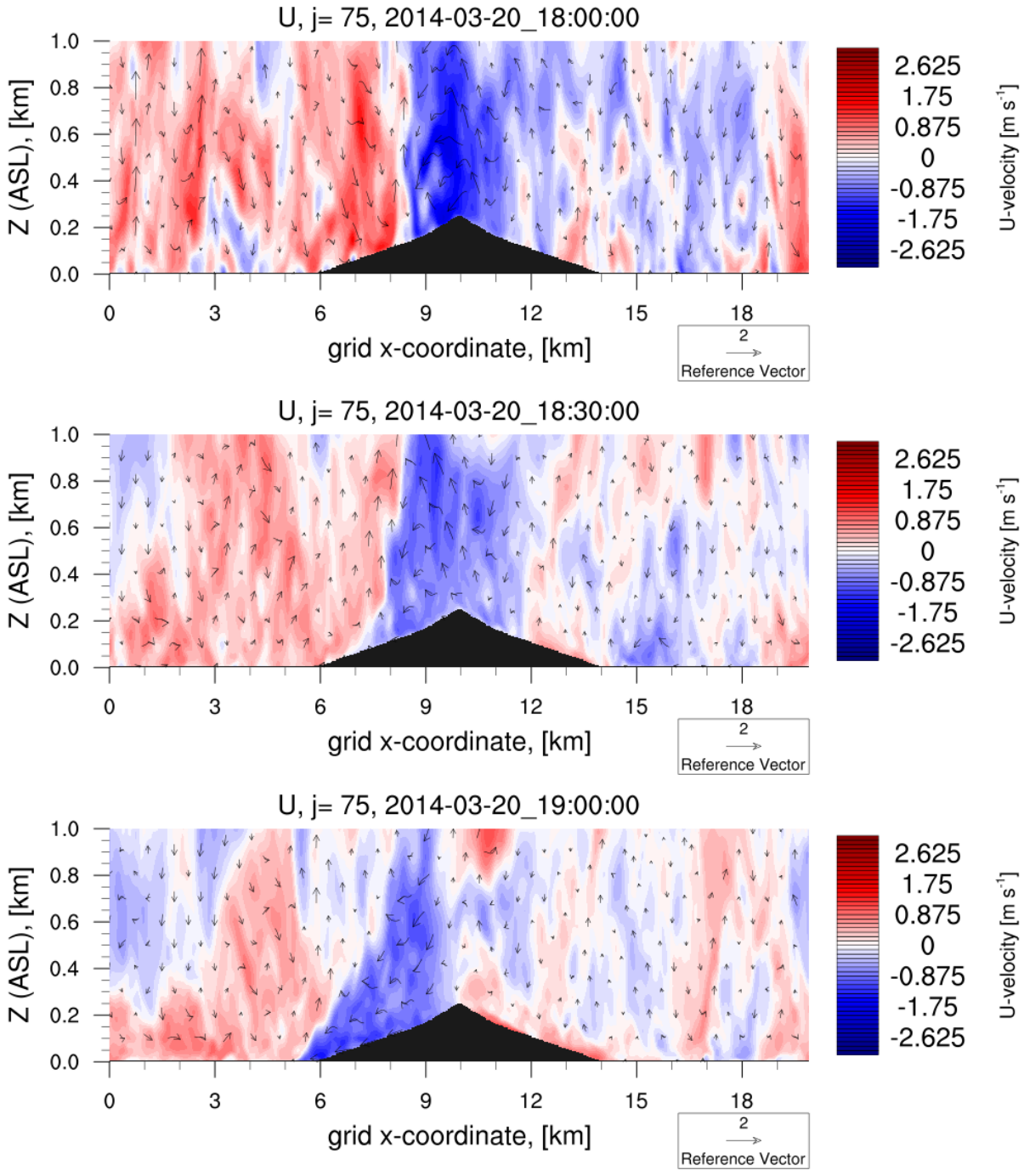

Figure 4.13: Vertical cross sections of horizontal velocity during the onset of downslope flow in LES3

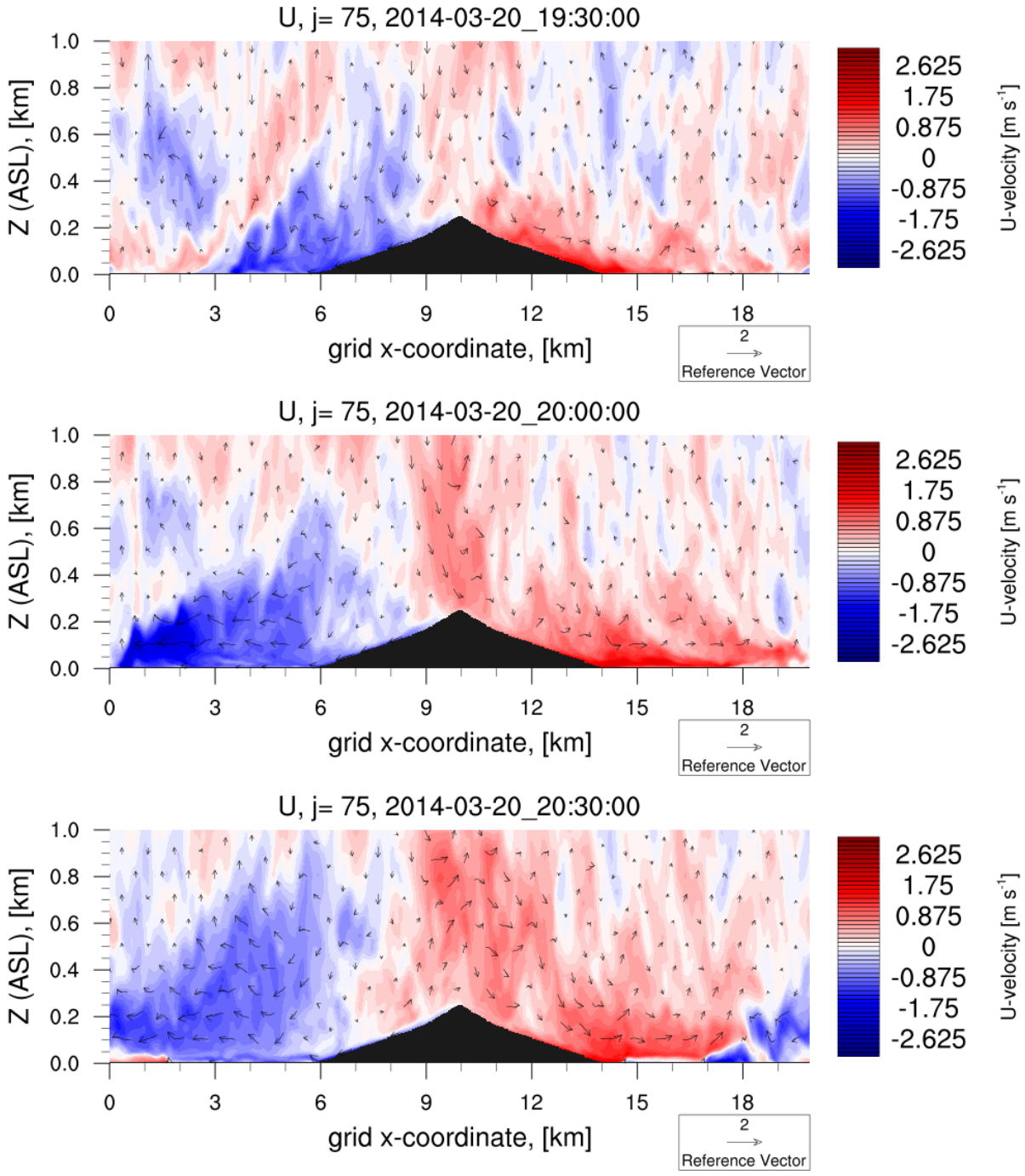

Figure 4.14: Vertical cross sections of horizontal velocity showing the continued development of downslope flow in LES3

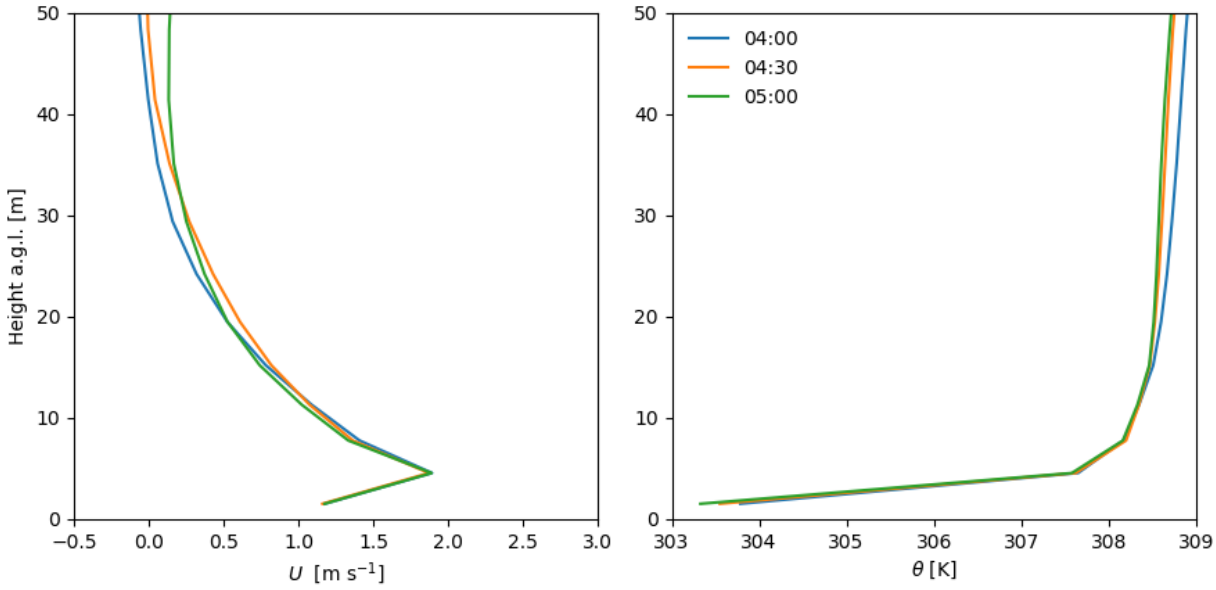

Figure 4.15: Velocity and potential temperature profiles from various times, centered about 04:30, on the middle of the lower slope, $x - x_{\text{mid}} = 2525$ m, on the eastern side of the mountain in the LES3 simulations.

initial downslope flows may be distinguished as 'plunging' flows rather than 'drainage' flows. Classically understood drainage flows can be distinguished at 20:00, in the wake of the plunging flow over the western slope. By 20:30, the two air masses collide near the periodic boundary. The inertia of the easterly flow pushes up the eastern slope to the peak of the mountain at 22:30 (Figure 4.6), influencing the further development of drainage flows due to a shortcoming of the semi-ideal model setup. Similar intrusion repeat throughout the night, at ≈01:00 and ≈03:30. It is not until much later that this artificial feature of the model becomes weak enough to study the steady state structure of the drainage flow, which is explored further in the following section.

Mature drainage flow

Though the initial stages of downslope flow development are complicated by both persistent convective structures and periodic boundary conditions, drainage flow in the later stages of the nocturnal period are quite comparable to the analytical solutions presented in the background (Section 4.2). Critically, we must establish that these flows are fully developed and reach steady state. For at least an hour, from 04:00 until 05:00, velocity and potential temperature profiles show steady state at the middle of the shallower western slope as shown in Figure 4.15. During the middle of this hour, at 04:30, the profiles of velocity vary only slightly for the ten points, a sixth of the total slope length, centered at the middle of the slope

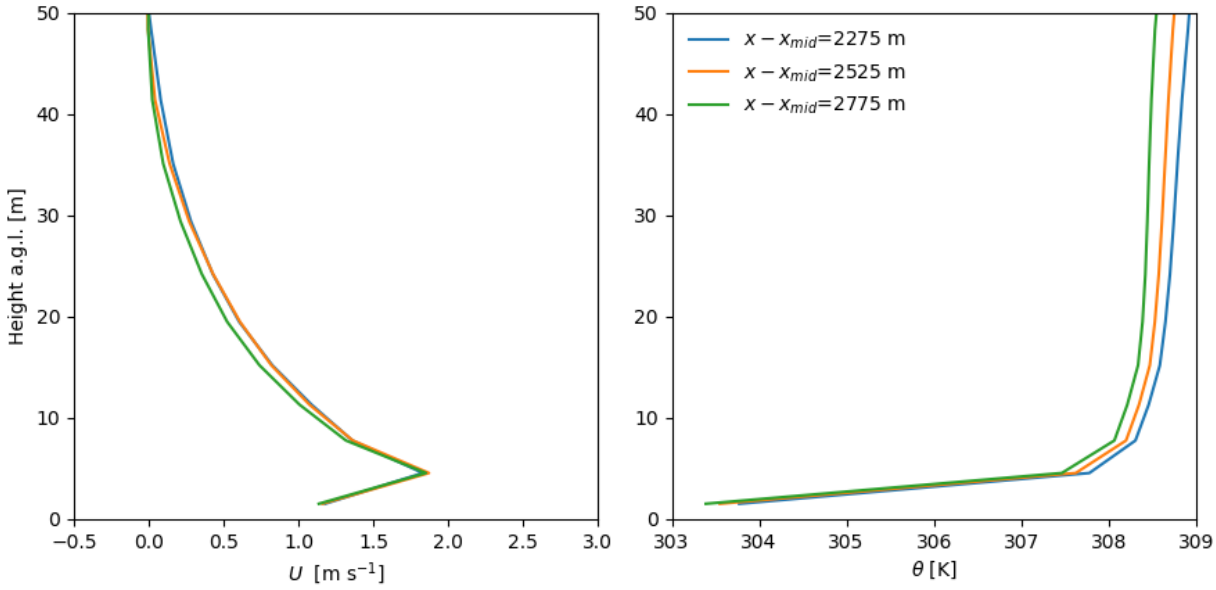

Figure 4.16: Velocity and potential temperature profiles for various distances, centered about $x - x_{\text{mid}} = 2525$ m, along the lower slope of the eastern side of the mountain at 04:30 in the LES3 simulation.

(Figure 4.16). Recall, the steady state, fully developed profiles predicted by the analytical solutions are for the potential temperature *perturbation* and the profiles from the semi-ideal WRF model are of potential temperature itself. Though none of the profiles are coincident, the perturbation is still fully developed and steady state when potential temperatures are shifted by a constant value, which is approximately true during the times shown. Indeed, we expect the the full potential temperature to cool over the nocturnal period, including the hour in which the perturbation is in steady state. Further, the difference between temperature profiles is consistent with stable background conditions, air further up the slope is warmer than lower on the slope, albeit only slightly given the shallow slopes considered here. This time, 04:30, and location, middle of the shadow slope are selected for the following comparisons to analytical solutions and for the investigation into dependence on the terrain slope.

Additional parameters required for comparison to the analytical solutions of drainage flows are background lapse rate, boundary temperature perturbation, momentum (or heat) diffusivity, and a Prandtl number. Though a single value for the temperature perturbation at the surface, θ_0', is obtainable from profiles, the other parameters are more variable. For instance, the lapse rate, Γ, is not constant, and has a more physically realistic profile in which stronger stability is observed nearer the surface of the plains than it is farther aloft (Figure 4.17). This feature is in part due to the drainage flows themselves, and exemplifies one way that the WRF model is more sophisticated than any of the analytical solutions. Other

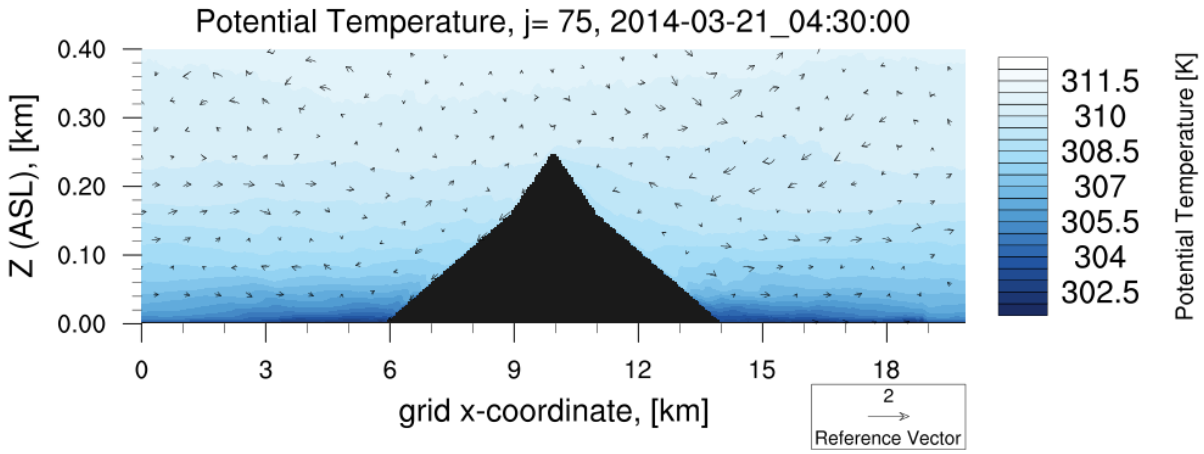

Figure 4.17: Potential temperature contours for a vertical cross section of the simple two-slope mountain in the semi-ideal WRF model, which evidence a stable background stratification comparable to that assumed by the Prandtl analytical model.

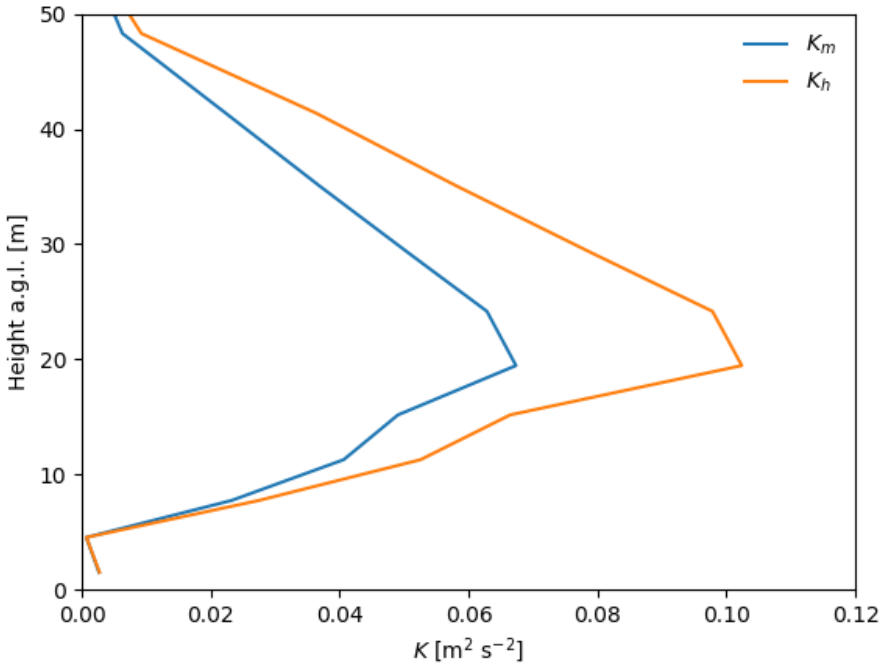

Figure 4.18: Profiles of vertical diffusion coefficients for velocity and heat from the middle of the shallow slope at 04:30 on the east side of the peak in the LES3 simulation.

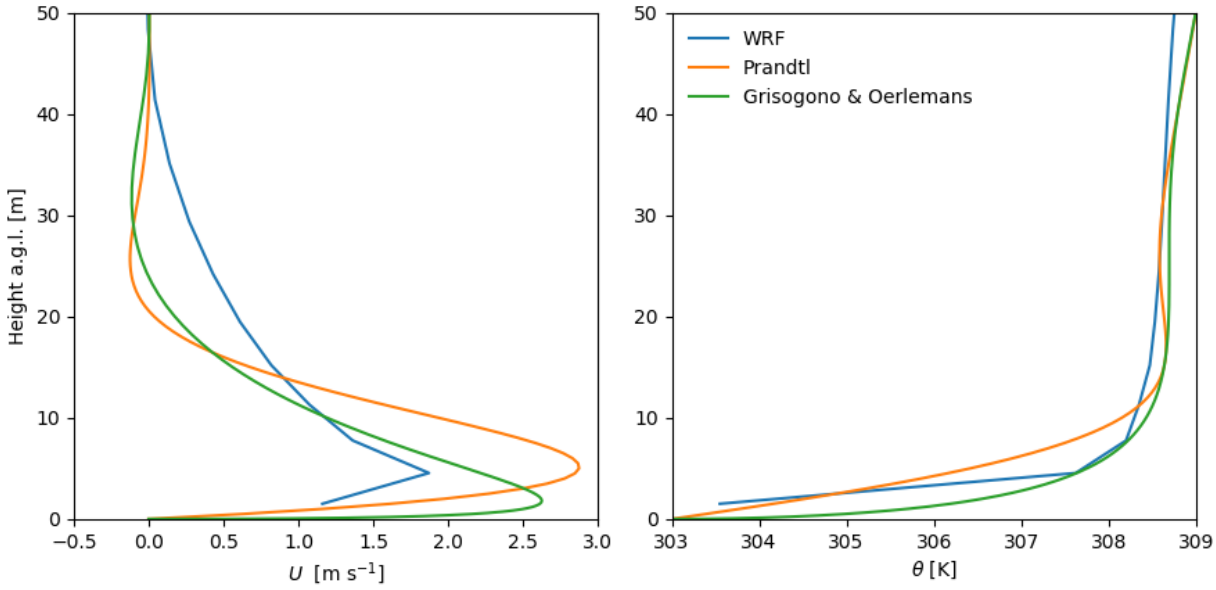

Figure 4.19: Velocity profiles at the middle of the lower slope, $x - x_{\text{mid}} = 2525$ m, at 04:30 on the east side of the peak from LES3 compared to the analytical solutions due to Prandtl (Figure 4.2) and to Grisogono and Oerlemans (Figure 4.4)

parameters, K_M and K_H, are computed by the TKE 1.5 order turbulence closure (Deardorff 1980) and vary in height (Figure 4.18). From the Grisogono and Oerlemans solution with this feature, we can expect a lower jet height than that predicted by the Prandtl solution. An important source of discrepancy between WRF and even these more advanced analytical solutions is that the Prandtl number is not constant in height for WRF. Despite differences between the WRF model and the analytical solutions, approximate values can be obtained for all the parameters that appear in the closed forms. To compare to the Prandtl solution, we estimate parameters used in the analytical solution from the full WRF model solutions:

$$\theta_0' = -5 \text{ K} \tag{4.48}$$
$$\theta_0 = 308 \text{ K} \tag{4.49}$$
$$\Gamma = 0.02 \text{ K m}^{-1} \tag{4.50}$$
$$K_M = 0.02 \text{ m}^2 \text{ s}^{-2} \tag{4.51}$$
$$K_H = 0.04 \text{ m}^2 \text{ s}^{-2} \tag{4.52}$$
$$g = 9.8 \text{ m s}^{-2} \tag{4.53}$$
$$\phi = 3^\circ \tag{4.54}$$

to plot the analytical solutions given by Equations 4.21 and 4.22, the classic Prandtl solution, in Figure 4.2 as the potential temperature perturbation and in Figure 4.19 as the full field. This simple analytic model compares well to the WRF simulations, particularly

with regard to the height of the velocity maximum, which occurs around $n \approx 5$ m a.g.l. in both models. When it comes to real weather simulation, where parameters can be obtained beforehand through observation data, the simple model would be useful in determining resolution requirements of the simulation. The value of the velocity maximum is slightly higher in the Prandtl model, but the region of downslope flow is shallower, resulting in similar total momentum flux. The deeper flow in the WRF model may be a consequence of having larger diffusivities above the jet height. This feature can be accounted for with the sophisticated, WKB analytical solution due to Grisogono and Axelsen (2012). For the sake of comparison to the WKB solution we take parameters

$$\theta_0^{'} = -5 \text{ K} \tag{4.55}$$
$$\theta_0 = 308 \text{ K} \tag{4.56}$$
$$\Gamma = 0.02 \text{ K m}^{-1} \tag{4.57}$$
$$K_H = Cn \exp\left(\frac{-n^2}{2h^2}\right) \tag{4.58}$$
$$C = 0.01 \text{ m s}^{-2} \tag{4.59}$$
$$h = 18 \text{ m} \tag{4.60}$$
$$K_M = PrK_H \tag{4.61}$$
$$Pr = 0.6 \tag{4.62}$$
$$g = 9.8 \text{ m s}^{-2} \tag{4.63}$$
$$\phi = 3^\circ \tag{4.64}$$

to plot the WKB solution in Figure 4.4 and Figure 4.19. Surprisingly, though the diffusivities used in the WKB solution are quite similar to those prognosticated by the WRF model (comparing Figure 4.3 to Figure 4.18), it is not clear to which analytical solution the WRF simulations compare better. This is particularly true with regard to the height of the velocity maximum, which is approximately 5 m in the WRF and Prandtl models, but only about 2.5 m in the WKB solution. Some of this discrepancy, however, is due model resolution in the WRF simulations. Recall, a limit on model vertical resolution, first given in the general case by Mahrer (1984) but applied specifically to the WRF model by Connolly et al. (2020) reproduced in Chapter 2, is

$$\Delta z \gtrsim \tan\phi \frac{\Delta x}{b} = \tan 5^\circ \frac{50 \text{ m}}{3} \approx 1.5 \,, \tag{4.65}$$

which is precisely the height of the first model half-level. As such, vertical resolution cannot be further refined without refining horizontal resolution and time step, which can quickly become prohibitively expensive. Future work may benefit from expending such computational cost, but it is not done here.

We may be tempted to conclude that the Prandtl model is therefore more valuable than the WKB solution, given equal agreement with advanced simulation and its simple

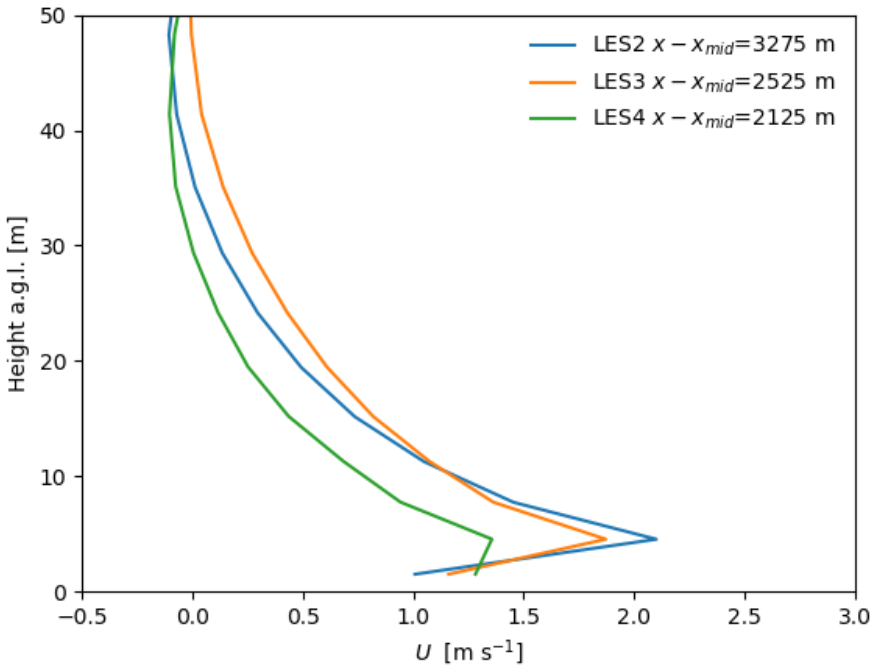

Figure 4.20: Velocity profiles at the middle of the lower slope on the east side of the peak from LES2, LES3, and LES4 simulations. Different x values control the strength of stratification between runs by taking the profiles from the same height above the plains, $h(x - x_{\text{mid}}) = 78.6$ m, in each case.

formulation. One counterpoint to this line of reasoning is the body of observational evidence on extremely shallow wind jets occurring on slopes during nocturnal conditions. We may grant that the WRF model is significantly more advanced than the analytic models, but may still be lacking. Indeed, there are important simplifications assumed by WRF, specifically for the surface layer model, that may render it inept for even the simple sloping geometry of the current simulations. We examine these simplifications in more detail in Appendix A. For now, suffice it to say, the prediction of the height of velocity maximum in drainage flow is no simple task. Despite this, the generally favorable comparison between all three models is promising for the future parameterization of drainage flow in coarser models that may find either of the tractable analytical solutions presented here useful towards that endeavor.

Dependence on Slope

Results from the classic Prandtl model of drainage flow show that the magnitude of the velocity maximum is independent of slope while the height of this maximum does vary with

slope. Precisely,

$$n_{JH} \propto 1/\sqrt{\sin\phi} \tag{4.66}$$

$$u_{max} \propto (\sin\phi)^0 . \tag{4.67}$$

Contrary to this result, field data show that on valley and glacier walls, maximum wind velocity does decrease with greater slope angles (Axelsen and Dop 2009a). This is often cited as a major shortcoming of the Prandtl model (Grisogono and Axelsen 2012; Axelsen and Dop 2009b). However, if instead of a constant temperature deficiency we assigned a constant temperature flux, $\overline{w'\theta'}$, as a Neumann boundary condition,

$$\frac{\partial\theta'}{\partial n}|(n=0) = \frac{-\overline{w'\theta'}}{K_H} \tag{4.68}$$

we get

$$\theta_0^{'} = \frac{-\overline{w'\theta'}}{\sigma K_H} = -\overline{w'\theta'}\left(\frac{4\theta_0 K_M}{g\Gamma K_H^3 \sin^2\phi}\right)^{\frac{1}{4}} \tag{4.69}$$

and, upon substitution into 4.24,

$$u_{max} = -\overline{w'\theta'}\left(\frac{g}{\theta_0 K_M K_H \Gamma^3 \sin^2\phi}\right)^{\frac{1}{4}} e^{\frac{-\pi}{4}}. \tag{4.70}$$

In this case, u_{max} does decrease over steeper slopes. More precisely, replacing the Dirichlet boundary conditions with Neumann boundary conditions in the Prandtl model gives

$$n_{JH} \propto 1/\sqrt{\sin\phi} \tag{4.71}$$

$$u_{max} \propto 1/\sqrt{\sin\phi} \tag{4.72}$$

These trends agree with previous LES studies which did find $n_{JH} \propto 1/\sqrt{\sin\phi}$ and either $u_{max} \propto 1/\sqrt{\sin\phi}$ based on one study (Grisogono and Axelsen 2012), or $u_{max} \propto 1/\sin\phi$ based on another (Axelsen and Dop 2009a,b). Both results have the feature of decreasing velocity maximum with increasing incline angle, so are qualitatively similar to the current analytical result. While the previously cited LES used fuller sets of equations than those of the Prandtl model, none were coupled with advanced surface or soil parameterizations such as those available in WRF. Importantly, even when momentum fluxes were evaluated from MOST, either constant surface cooling or constant buoyancy fluxes (analogous to heat flux) were prescribed. The WRF model physics are more sophisticated, using fully coupled Noah land surface model and a MOST surface-layer scheme that evaluates the fluxes of both momentum and heat, so it is worthwhile to investigate the dependence on slope in the current simulations. Velocity profiles from LES2, LES3, and LES4 which represent slope angles of 2, 3, and 4°, respectively, are shown in Figure 4.20. While the relatively coarse resolution precludes a statistical power law fit to the $\sin\phi$, the qualitative features agree quite well with the previous literature. That is, the velocity maximum decreases with increasing slope angle in WRF simulations with full physics.

4.5 Conclusion

Though advanced LES are routinely carried out by WRF, we have shown some benefit to simple analytical models. A novel analytical solution uses Neumann boundary conditions for the temperature perturbation and recreates the dependence of the velocity maximum on slope angle which is found in observation data but not as a result of the original Prandtl solution. The observed agreement between the WRF model and the analytical models bodes well for the parameterization of drainage flows in coarser, mesoscale NWP models. Despite these successes, the utility of the analytical models has only been established for mature drainage flows.

The onset of drainage flows does not resemble these analytical and numerical models of fully developed, steady state drainage flow. Rather, persistent convective structures in the atmospheric boundary layer can complicate the analysis of the transient solutions to drainage flows. Importantly, horizontal convergence due to convective updrafts, which persist on the sunnier side of slopes, can lead to more rapid development of strong drainage flows on the side of the mountain which receives less surface cooling than the side of the mountain onto which a shadow is cast earlier in the evening transition. This feature is perhaps counterintuitive, and may not be present in cases that differ substantially from those presented here. In part, this may depend on the surface and soil characteristics, which would be good topics for future systematic investigation, as well as the timing of the shadow propagation itself. Here, we use a simple analytical result to determine the timing of the shadow front based on the slopes and lengths of the compound-slope mountain geometry. In concert with site specific information, such as the soil and surface characteristics that determine the force balance between buoyancy and the inertia of persistent convective structures, this result can be useful to determine whether the onset of drainage flows will follow or be concurrent with the shadow front.

The WRF model has robust physical parameterizations, despite arguable shortcomings in the surface layer model for complex terrain cases (Appendix A). The current work has been successful in advancing drainage flow simulations from the use of engineering codes to NWP codes, such as WRF, with full physics. This allows investigation into not only questions considered by the classic analytical approach, such as the dependence of drainage flows on the slope of underlying terrain, but also questions that are not addressed by previous analytical work, such as the onset of drainage flow relative to the passing of the mountain shadow front. Though this brings new challenges, like revelations of the importance of preceding convective systems, the work done here is an important step towards incorporating drainage flow physics into mesoscale models, with the ultimate goal of improving weather prediction.

Chapter 5

Conclusion

Advanced numerical simulations have been employed for study of the atmospheric boundary layer throughout this dissertation. In the course of using the large-eddy simulation (LES) technique to study fundamental physics questions, understanding of the technique itself has also been improved. As with all such work, improving the capabilities of numerical weather prediction (NWP) to the benefit of those who live in the atmospheric boundary layer, is an ultimate goal. The benefits of LES in this regard include improved characterization of the local stability of the atmosphere and the details of the underlying terrain. Especially for stable flow, the interaction of stratification and topography lead to a multitude of phenomena for which past NWP efforts, which do not employ the LES technique, have been less successful. Whether to prepare for a world with computers powerful enough to run predictive LES, or to improve future parameterizations for use in the current generation of NWP models, LES is proven an extremely valuable tool for researchers interested in atmospheric boundary layer flow.

Three projects, related by their use of LES and their interest in the effects of stratification, are the primary focus of this dissertation. The first project, conducted as part of the Mountain Terrain Atmospheric Modeling and Observations (MATERHORN) program, focuses on a nominally isolated desert mountain, Granite Peak, in Utah and the surrounding basin (Fernando et al. 2015). A driving goal of the program is improving the parameterizations in mesoscale models of topographically induced flow. The second study is part of the Perdigão project, whose field site is a narrow valley between nearly parallel ridges in Portugal. Interest of the greater project include improved understanding of stable flows in the valley and ridge slopes, with particular regard to the fate of a turbine wake installed on one of the ridges. The part of the project considered in this dissertation deals with the preliminary concern of mitigating the computational expense of the LES used in pursuit of these ultimate goals of the project. The third work, independently undertaken, investigates fundamental controls on drainage flow by developing and using a semi-ideal numerical model. The ubiquity of these drainage flow in the stable atmospheric boundary layer for complex terrain relates the final study to both the previous projects and exemplifies the benefits of LES for similar future projects.

Working on the MATERHORN project, in Chapter 2, large-eddy simulations explored several phenomena due to topography's influence on flow in the stable boundary layer. For one, lee vortices in the orographic wake of Granite Peak, Utah were modeled at, to the author's knowledge, the highest resolutions for any real weather case study. This chapter established the utility of the non-dimensional parameters, extensively used to characterize stable flows in idealized models, for real weather simulations. The non-dimensional mountain height,

$$\eta = \frac{NH}{U}, \tag{5.1}$$

where N is the buoyancy frequency, H is the mountain height, and U is the free-stream velocity, was shown to be predictive of the occurrence of lee vortices in real weather LES. This is critical to future parameterization of the stable atmospheric boundary layer, because such non-dimensional numbers can be obtained even by models too coarse to resolve the

lee vortices themselves. Part of the success of the LES discussed in this chapter relies on adherence to a novel limit on the model time step, as well as previously known numerical stability limits on vertical grid spacing (Mahrer 1984), which together can be abbreviated as a double inequality. With model time step, Δt; the Courant-Friedrichs-Levy (CFL) stability limit constant, C; the Mahrer limit constant, b; horizontal grid spacing, Δx; vertical grid spacing, Δz; and maximum slope, α, these stability limits,

$$\Delta t \lesssim \frac{C}{b}\Delta x \lesssim C\frac{\Delta z}{\tan\alpha}, \tag{5.2}$$

must be used in place of the original CFL condition for cases of steep terrain. The novel limit on time step, the first inequality, describes how the time step must be further reduced, ensuring numerical stability but incurring greater computational cost. Another stable boundary layer feature, a cold-air pool, also develops in the basin to the east of Granite Peak, though it exhibits a warm bias in the LES. The bias is attributed to unresolved drainage flows by tuning the model for maximal *in situ* cooling during a test of the model sensitivity to soil moisture. The shortcoming of the model is explained by the second inequality which limits vertical resolution given horizontal grid spacing set by practical considerations of computational cost. First dubbed "large temperature fluctuations" by collaborators working on the MATERHORN, another stable flow phenomenon resolved by the LES is due to the interaction of the lee vortices and the cold air pool. Though the large temperature fluctuations had been modeled previously, the quality of the current large-eddy simulations allows for further insights. For example, the effects on the large temperature fluctuations due to the occurrence of yet another common feature of the stable boundary layer, gap flow. By interfering with the lee vortices, the strengthening of a flow through a gap south of Granite Peak is associated with the recovery of temperature during one of the resolved large temperature fluctuations. The lee vortices do not appear after the gap flow is strengthened, despite sufficiently large non-dimensional mountain height. In this case, comparison to ideal models is imperfect because of the multiplicity of phenomena in the stable boundary layer. This indicates that there is, unsurprisingly, more work to be done in pursuit of improved modeling of the interaction between stable flow and topography. To that end, LES has proven to be exceedingly valuable, but only when minding the novel numerical stability limit, which unfortunately implies higher computational cost must be borne.

Chapter 3 investigates whether the high computational cost of the LES technique can be mitigated through an artificial turbulence generation technique, the cell perturbation method (CPM), using the Perdigão site as a test-bed. For the LES of real weather, synoptic forcing is often dynamically downscaled by nesting finer resolution numerical domains within coarser ones. Though this multiscale modeling approach is suitable for passing information resolved by parent mesoscale models to child LES domains, it is unable to pass information on three-dimensional atmospheric boundary layer turbulence because these are subgrid scale in mesoscale models. Instead, nested LES must develop this turbulence as the resolved flow progresses some distance from the inflow boundary, called fetch. To ensure sufficient fetch is present for turbulence to develop, nested LES are often made significantly larger

than the actual region of interest. This additional domain size represents a great deal of computations which provide a solution no more detailed than the parent model could provide itself. Artificial perturbations applied near the inflow boundary of an LES hope to accelerate the development of turbulence, allowing for reduced fetch and computational cost. The CPM does this by perturbing the potential temperature field. Pseudorandom perturbations, $\tilde{\theta}_\mathrm{p}$, are drawn from a distribution, $\tilde{\theta}_\mathrm{p} \in [-\tilde{\theta}_\mathrm{pm}, \tilde{\theta}_\mathrm{pm}]$ informed by information that can be passed from the mesoscale parent, such as mean velocities and the boundary layer height, z_i. Specifically, the maximum perturbation magnitudes are given by a perturbation Eckert number,

$$Ec = \frac{U_g^2}{c_p \tilde{\theta}_\mathrm{pm}} = 0.2 \tag{5.3}$$

where U_g is the mean wind velocity evaluated at $1.1 z_i$ along the inflow boundaries, and c_p =1004.6 J kg^{-1} K^{-1} is the specific heat capacity of air. While the CPM has been successful in accelerating the generation of turbulence for flat terrain cases, some have hypothesized that the CPM will not be useful for complex terrain cases. For instance, Rai et al. (2017) argue that the presence of convective forcing and injection scale eddies resulting from the terrain itself are sufficient to generate boundary layer turbulence. To test such a hypothesis, a numerical experiment is devised and presented. One set of simulations, with and without CPM applied, uses topography significantly coarser than the LES grid mesh to ensure relatively smooth terrain. Another set makes use of topography finer than the grid mesh, ensuring the topography is as complex as could possibly be represented on the grid. Both sets of simulations are compared to a reference simulation, which takes the traditional approach of simply using a much larger domain size, during different times of the day. While it is true that the benefits of the CPM do not manifest during the periods of strongest convection, during the evening transition significant acceleration of turbulence generation was observed in simulations with CPM applied, even for the complex topography set of simulations. As such, the hypothesis of Rai et al. (2017) is not without merit under strongly convective conditions, but the current study establishes the usefulness of the CPM under weakly convective conditions even for a complex terrain case. Given that the reference simulation, with increased fetch, requires 5 times as many CPU-hours while the cost of CPM is entirely negligible, the CPM is an attractive alternative.

A final study, in Chapter 4, revisits the problem of drainage flow, buoyancy driven downslope flows. Drainage flows contribute to dynamic cooling of cold-air pools, and can have a detrimental effect on agricultural activities on sloped terrain. Recall, the absence of drainage flow resulted in a model warm bias in the cold-air pool at the MATERHORN site. Further, drainage flow is likely to affect the transport of the wind turbine wake at the Perdigão site, which is a primary concern of the project. Rather than using either of the MATERHORN or the Perdigão field sites, a semi-ideal geometry is used to make more direct comparisons to analytical solutions. These analytical models are best suited to ultimately formulate subgrid parameterizations of drainage flow, which could alleviate the biases experienced during the MATERHORN. Similar to the previous simulations, the

Weather Research and Forecast (WRF) model is used for the current idealized simulations. Benefits of using such an advanced NWP code are the inclusion of radiation physics, including shadow effects, and prognosticating surface heat flux through fully coupled land surface model and MOST-type surface layer parameterization. This allows the investigation not only of the nocturnal period, which has previously been studied by simple prescribed cooling (Axelsen and Dop 2009a,b), but the evening transition period. Though these physics are state-of-the-art, a simple model topography consists of piecewise linear slopes,

$$h\left(x;\phi_1,L_1,\phi_2,L_2\right)=\begin{cases}0 & |x-x_{\text{mid}}|\geq L_1+L_2\\ \tan\phi_1\left(L_1+L_2-|x-x_{\text{mid}}|\right) & L_2<|x-x_{\text{mid}}|<L_1+L_2\\ \tan\phi_1 L_1+\tan\phi_2\left(L_2-|x-x_{\text{mid}}|\right) & |x-x_{\text{mid}}|\leq L_2\end{cases} \tag{5.4}$$

where ϕ_1 and L_1 are the shallower slope and length of the mountain base while ϕ_2 and L_2 are the steeper slope and length of the mountain peak whose highest point is at x_{mid}, the middle of the domain. In addition to clearly defining the slope of the terrain, the linear functions allow us to solve analytically for the timing of the shadow front, cast from the mountain peak, as it propagates down the eastern mountain base during sunset. As a parametric equation in hours,

$$t=18-\frac{12}{\pi}\arctan\left[\tan\phi_1+\frac{L_2}{x-x_{\text{mid}}}\left(\tan\phi_2-\tan\phi_1\right)\right], \tag{5.5}$$

the function has the simple interpretation of the true sunset, 18 hrs, minus an offset due to presence of terrain. Unlike previous real case simulations (Arthur et al. 2018), however, the passage of the shadow front in the current simulations does not immediately coincide with a transition from upslope to downslope flow. The expected transition to downslope flow occurs some time after sunset, but the transition occurs on the western slope sooner than on the shadow-cast eastern slope. This perhaps counterintuitive result can be explained by the presence of convective structures that persist after sunset and lead to horizontal convergence on the sunny side of the mountain which reinforces the downslope flow on that side. Such a result is resolved by the current model, but not by previous idealized studies. Later in the nocturnal period, the drainage flow does approximate the fully developed, steady state as assumed by the analytical models. At these times, the results corroborate observation data that suggest maximum wind velocity decreases with increasing slope angle, a feature missing in the classic Prandtl (1942) solution to drainage flow. A new analytical solution to the same governing equations is proposed, which recovers this observed dependence of slope by replacing the traditional Dirichlet boundary condition for potential temperature, $\theta^{'}(n=0)=\theta_0^{'}$, with a Neumann boundary condition,

$$\frac{\partial\theta^{'}}{\partial n}|(n=0)=\frac{-\overline{w'\theta'}}{K_H}, \tag{5.6}$$

with surface heat flux, $-\overline{w'\theta'}$, and constant thermal diffusivity K_H. Though the assumption of a constant thermal diffusivity is undoubtedly nonphysical, another analytical solution,

which prescribes diffusivity as function of distance from the surface, actually compares less favorably to the LES results. Whether this is related to shortcomings of the variable diffusivity analytical model, or to vertical resolution of the LES, is worth further investigation. Whichever analytical model ultimately proves most capable, the general agreement between the LES and analytical solutions bodes well for parameterization of drainage flow to improve future numerical models.

High computational costs are required to resolve the atmospheric boundary layer, especially for topographically induced stable flow features, such as the drainage flows whose absence inhibits accurate forecasting. In part, this is explained by the new stability limit presented in Chapter 2, which requires model time steps be further decreased in cases of steeply sloped terrain. The costs are exacerbated by the need for fine meshes in large-eddy simulation. Sufficient fetch to develop turbulence, resulting in relatively large horizontal extents in large-eddy simulation, is typically a further requirement. A potential recourse for the modeler is to spur the generation of turbulence through some artificial technique. One such technique is tested in Chapter 3, motivated by the extreme computational costs required to resolve drainage flows, which were unresolved in the simulations of Chapter 2, as well as a wider class of boundary layer flows. Another recourse is to develop subgrid parameterizations. The extremely shallow nature of drainage flows, for instance, suggest parameterization is the best option for the foreseeable future. Steps towards both goals, reducing computational cost of LES and parameterizing microscale flow, are made in this dissertation. Hopefully, many will find these advances useful for future study of the atmospheric boundary layer.

Bibliography

Arthur, R. S., K. A. Lundquist, J. D. Mirocha, and F. K. Chow, 2018: Topographic effects on radiation in the WRF model with the immersed boundary method: Implementation, validation, and application to complex terrain. *Monthly Weather Review*, **146 (10)**, 3277–3292.

Arthur, R. S., J. D. Mirocha, N. Marjanovic, B. D. Hirth, J. L. Schroeder, S. Wharton, and F. K. Chow, 2020: Multi-scale simulation of wind farm performance during a frontal passage. *Atmosphere*, **11 (3)**, 245.

Axelsen, S., and H. Dop, 2009a: Large-eddy simulation of katabatic winds. Part 1: Comparison with observations. *Acta Geophysica*, **57 (4)**, 803–836.

Axelsen, S., and H. Dop, 2009b: Large-eddy simulation of katabatic winds. Part 2: Sensitivity study and comparison with analytical models. *Acta Geophysica*, **57 (4)**, 837–856.

Ayotte, K. W., 2008: Computational modelling for wind energy assessment. *Journal of Wind Engineering and Industrial Aerodynamics*, **96 (10-11)**, 1571–1590.

Babić, N., and S. F. De Wekker, 2019: Characteristics of roll and cellular convection in a deep and wide semiarid valley: A large-eddy simulation study. *Atmospheric Research*, **223**, 74–87.

Baines, P., 1979: Observations of stratified flow past three-dimensional barriers. *Journal of Geophysical Research: Oceans*, **84 (C12)**, 7834–7838.

Baines, P. G., 1998: *Topographic effects in stratified flows*. Cambridge University Press.

Bao, J., F. K. Chow, and K. A. Lundquist, 2018: Large-eddy simulation over complex terrain using an improved immersed boundary method in the weather research and forecasting model. *Monthly Weather Review*, **146 (9)**, 2781–2797, doi: 10.1175/MWR-D-18-0067.1.

Basu, S., A. A. Holtslag, B. J. Van De Wiel, A. F. Moene, and G.-J. Steeneveld, 2008: An inconvenient "truth" about using sensible heat flux as a surface boundary condition in models under stably stratified regimes. *Acta Geophysica*, **56 (1)**, 88–99.

Benoit, R., 1977: On the integral of the surface layer profile-gradient functions. *Journal of Applied Meteorology*, **16 (8)**, 859–860.

Bossard, M., J. Feranec, J. Otahel, and Coauthors, 2000: CORINE land cover technical guide: Addendum 2000. Tech. rep.

Burns, P., and C. Chemel, 2014: Evolution of cold-air-pooling processes in complex terrain. *Boundary-Layer Meteorology*, **150 (3)**, 423–447, doi: 10.1007/s10546-013-9885-z, URL https://doi.org/10.1007/s10546-013-9885-z.

Businger, J. A., J. C. Wyngaard, Y. Izumi, and E. F. Bradley, 1971: Flux-profile relationships in the atmospheric surface layer. *Journal of the Atmospheric Sciences*, **28 (2)**, 181–189.

Chen, F., and J. Dudhia, 2001: Coupling an advanced land surface-hydrology model with the Penn State-NCAR MM5 modeling system. Part I: Model implementation and sensitivity. *Monthly Weather Review*, **129 (4)**, 569–585.

Chen, F., Z. Janjić, and K. Mitchell, 1997: Impact of atmospheric surface-layer parameterizations in the new land-surface scheme of the NCEP mesoscale eta model. *Boundary-Layer Meteorology*, **85 (3)**, 391–421.

Ching, J., R. Rotunno, M. LeMone, A. Martilli, B. Kosovic, P. A. Jimenez, and J. Dudhia, 2014: Convectively Induced Secondary Circulations in Fine-Grid Mesoscale Numerical Weather Prediction Models. *Monthly Weather Review*, **142 (9)**, 3284–3302, doi: 10.1175/MWR-D-13-00318.1, URL https://doi.org/10.1175/MWR-D-13-00318.1, https://journals.ametsoc.org/mwr/article-pdf/142/9/3284/4304156/mwr-d-13-00318_1.pdf.

Chow, F. K., S. F. De Wekker, and B. J. Snyder, Eds., 2013: *Mountain weather research and forecasting: recent progress and current challenges*. Springer, New York.

Chow, F. K., A. P. Weigel, R. L. Street, M. W. Rotach, and M. Xue, 2006: High-resolution large-eddy simulations of flow in a steep alpine valley. part i: Methodology, verification, and sensitivity experiments. *Journal of Applied Meteorology and Climatology*, **45 (1)**, 63–86.

Chow, T. K., L. van Veen, J. Neher, A. Anderson-Connolly, J. Mirocha, and B. Geurts, 2018: Generation of turbulent structures in nested simulations for the perdigao campaign. *18th Conference of Mountain Meteorology*, 9.4A, https://ams.confex.com/ams/18Mountain/meetingapp.cgi/Home/0.

Connolly, A., F. K. Chow, and S. W. Hoch, 2020: Nested large-eddy simulations of the displacement of a cold-air pool by lee vortices. *Boundary-Layer Meteorology*, 1–28.

Connolly, A., L. van Veen, J. Neher, B. Geurts, J. Mirocha, and F. K. Chow, submitted: Efficacy of the cell perturbation method in large-eddy simulations of boundary layer flow over complex terrain. *Atmosphere*, –.

De Wekker, S. F., and M. Kossmann, 2015: Convective boundary layer heights over mountainous terrain—a review of concepts. *Frontiers in Earth Science*, **3**, 77.

Deardorff, J. W., 1980: Stratocumulus-capped mixed layers derived from a three-dimensional model. *Boundary-Layer Meteorology*, **18 (4)**, 495–527.

Defant, F., 1949: Zur theorie der hangwinde, nebst bemerkungen zur theorie der berg-und talwinde. *Archiv für Meteorologie, Geophysik und Bioklimatologie, Serie A*, **1 (3-4)**, 421–450.

Duda, M., 2011: The wrf preprocessing system: Description of general functions. *Joint NCAR-NCAS WRF Tutorial, Edinburgh, Scotland. URL http://www. mmm. ucar. edu/wrf/users/tutorial/201001/WPS-general. pdf.*

Dudhia, J., 1989: Numerical study of convection observed during the winter monsoon experiment using a mesoscale two-dimensional model. *Journal of the Atmospheric Sciences*, **46 (20)**, 3077–3107.

Durran, D., J. A. Weyn, and M. Q. Menchaca, 2017: Practical considerations for computing dimensional spectra from gridded data. *Monthly Weather Review*, **145 (9)**, 3901–3910.

Egger, J., 1990: Thermally forced flows: Theory. *Atmospheric processes over complex terrain*, Springer, 43–58.

Epifanio, C., and D. Durran, 2002a: Lee-vortex formation in free-slip stratified flow over ridges. Part I: Comparison of weakly nonlinear inviscid theory and fully nonlinear viscous simulations. *Journal of the Atmospheric Sciences*, **59 (7)**, 1153–1165.

Epifanio, C., and D. Durran, 2002b: Lee-vortex formation in free-slip stratified flow over ridges. Part II: Mechanisms of vorticity and PV production in nonlinear viscous wakes. *Journal of the Atmospheric Sciences*, **59 (7)**, 1166–1181.

Epifanio, C. C., 2003: Lee vortices. *Encyclopedia of Atmospheric Sciences*, J. Holton, J. Pyle, and J. Curry, Eds., Elsevier, Amsterdam, 1150–1160.

Epifanio, C. C., and R. Rotunno, 2005: The dynamics of orographic wake formation in flows with upstream blocking. *Journal of the Atmospheric Sciences*, **62 (9)**, 3127–3150.

Farr, T. G., and Coauthors, 2007: The shuttle radar topography mission. *Reviews of Geophysics*, **45 (2)**.

Fernando, H., and Coauthors, 2015: The MATERHORN: Unraveling the intricacies of mountain weather. *Bulletin of the American Meteorological Society*, **96 (11)**, 1945–1967.

Fernando, H., and Coauthors, 2019: The Perdigao: Peering into microscale details of mountain winds. *Bulletin of the American Meteorological Society*, **100 (5)**, 799–819.

Garratt, J. R., 1994: The atmospheric boundary layer. *Earth-Science Reviews*, **37 (1-2)**, 89–134.

Gesch, D., M. Oimoen, S. Greenlee, C. Nelson, M. Steuck, and D. Tyler, 2002: The national elevation dataset. *Photogrammetric Engineering and Remote Sensing*, **68 (1)**, 5–32.

Geurts, B. J., 2001: Mixing efficiency in turbulent shear layers. *Journal of Turbulence*, **2 (17)**, 1–23.

Geurts, B. J., and F. van der Bos, 2005: Numerically induced high-pass dynamics in large-eddy simulation. *Physics of Fluids*, **17 (12)**, 125 013.

Goodfriend, L., F. Chow, M. Vanella, and E. Balaras, 2014: Improving large-eddy simulation on adaptive mesh refinement grids using the turbulence closure. *Bulletin of the American Physical Society*, **59**.

Grisogono, B., and S. L. Axelsen, 2012: A note on the pure katabatic wind maximum over gentle slopes. *Boundary-Layer Meteorology*, **145 (3)**, 527–538.

Grisogono, B., and J. Oerlemans, 2001: Katabatic flow: Analytic solution for gradually varying eddy diffusivities. *Journal of the Atmospheric Sciences*, **58 (21)**, 3349–3354.

Holden, Z. A., and W. M. Jolly, 2011: Modeling topographic influences on fuel moisture and fire danger in complex terrain to improve wildland fire management decision support. *Forest Ecology and Management*, **262 (12)**, 2133–2141.

Holtslag, A. A. M., and Coauthors, 2013: Stable atmospheric boundary layers and diurnal cycles: Challenges for weather and climate models. *Bulletin of the American Meteorological Society*, **94 (11)**, 1691–1706, doi: 10.1175/BAMS-D-11-00187.1.

Hong, S.-Y., J. Dudhia, and S.-H. Chen, 2004: A revised approach to ice microphysical processes for the bulk parameterization of clouds and precipitation. *Monthly weather review*, **132 (1)**, 103–120.

Horst, T., and J. Doran, 1986: Nocturnal drainage flow on simple slopes. *Boundary-Layer Meteorology*, **34 (3)**, 263–286.

Janjić, Z. I., 1994: The step-mountain eta coordinate model: Further developments of the convection, viscous sublayer, and turbulence closure schemes. *Monthly Weather Review*, **122 (5)**, 927–945.

Jeglum, M., S. Hoch, D. Jensen, R. Dimitrova, and Z. Silver, 2017: Large temperature fluctuations due to cold air pool displacement along the lee slope of a desert mountain. *Journal of Applied Meteorology and Climatology*, **56 (4)**, 1083–1098.

Johansen, O., 1975: Thermal conductivity of soils. Ph.D. thesis, University of Trondheim, Norway, an optional note.

Keating, A., U. Piomelli, E. Balaras, and H.-J. Kaltenbach, 2004: A priori and a posteriori tests of inflow conditions for large-eddy simulation. *Physics of Fluids*, **16 (12)**, 4696–4712.

Kleinhans, D., R. Friedrich, A. Schaffarczyk, and J. Peinke, 2009: Synthetic turbulence models for wind turbine applications. *Progress in Turbulence III*, Springer, 111–114.

Lareau, N. P., E. Crosman, C. D. Whiteman, J. D. Horel, S. W. Hoch, W. O. Brown, and T. W. Horst, 2013: The persistent cold-air pool study. *Bulletin of the American Meteorological Society*, **94 (1)**, 51–63.

Lehner, M., C. D. Whiteman, S. W. Hoch, D. Jensen, E. R. Pardyjak, L. S. Leo, S. Di Sabatino, and H. J. Fernando, 2015: A case study of the nocturnal boundary layer evolution on a slope at the foot of a desert mountain. *Journal of Applied Meteorology and Climatology*, **54 (4)**, 732–751.

Leo, L. S., M. Y. Thompson, S. Di Sabatino, and H. J. Fernando, 2016: Stratified flow past a hill: dividing streamline concept revisited. *Boundary-Layer Meteorology*, **159 (3)**, 611–634.

Lilly, D. K., 1962: On the numerical simulation of buoyant convection. *Tellus*, **14 (2)**, 148–172.

Liu, Y., and Coauthors, 2008: The operational mesogamma-scale analysis and forecast system of the US Army Test and Evaluation Command. Part I: Overview of the modeling system, the forecast products, and how the products are used. *Journal of Applied Meteorology and Climatology*, **47 (4)**, 1077–1092.

Lund, T. S., X. Wu, and K. D. Squires, 1998: Generation of turbulent inflow data for spatially-developing boundary layer simulations. *Journal of computational physics*, **140 (2)**, 233–258.

Lundquist, K. A., F. K. Chow, and J. K. Lundquist, 2012: An immersed boundary method enabling large-eddy simulations of flow over complex terrain in the WRF model. *Monthly Weather Review*, **140 (12)**, 3936–3955.

Mahrer, Y., 1984: An improved numerical approximation of the horizontal gradients in a terrain-following coordinate system. *Monthly Weather Review*, **112 (5)**, 918–922.

Mahrt, L., 1982: Momentum balance of gravity flows. *Journal of the Atmospheric Sciences*, **39 (12)**, 2701–2711.

Manins, P., and B. Sawford, 1979: A model of katabatic winds. *Journal of the Atmospheric Sciences*, **36 (4)**, 619–630.

Marjanovic, N., J. D. Mirocha, B. Kosović, J. K. Lundquist, and F. K. Chow, 2017: Implementation of a generalized actuator line model for wind turbine parameterization in the weather research and forecasting model. *Journal of Renewable and Sustainable Energy*, **9 (6)**, 063 308.

Marjanovic, N., S. Wharton, and F. K. Chow, 2014: Investigation of model parameters for high-resolution wind energy forecasting: Case studies over simple and complex terrain. *Journal of Wind Engineering and Industrial Aerodynamics*, **134**, 10–24.

Massey, J. D., W. J. Steenburgh, S. W. Hoch, and J. C. Knievel, 2014: Sensitivity of near-surface temperature forecasts to soil properties over a sparsely vegetated dryland region. *Journal of Applied Meteorology and Climatology*, **53 (8)**, 1976–1995.

Massey, J. D., W. J. Steenburgh, J. C. Knievel, and W. Y. Cheng, 2016: Regional soil moisture biases and their influence on WRF model temperature forecasts over the intermountain west. *Weather and Forecasting*, **31 (1)**, 197–216.

McCumber, M. C., and R. A. Pielke, 1981: Simulation of the effects of surface fluxes of heat and moisture in a mesoscale numerical model: 1. soil layer. *Journal of Geophysical Research: Oceans*, **86 (C10)**, 9929–9938.

Mirocha, J., G. Kirkil, E. Bou-Zeid, F. K. Chow, and B. Kosović, 2013: Transition and equilibration of neutral atmospheric boundary layer flow in one-way nested large-eddy simulations using the weather research and forecasting model. *Monthly Weather Review*, **141 (3)**, 918–940.

Mirocha, J., B. Kosović, and G. Kirkil, 2014: Resolved turbulence characteristics in large-eddy simulations nested within mesoscale simulations using the Weather Research and Forecasting model. *Monthly Weather Review*, **142 (2)**, 806–831.

Mlawer, E. J., S. J. Taubman, P. D. Brown, M. J. Iacono, and S. A. Clough, 1997: Radiative transfer for inhomogeneous atmospheres: RRTM, a validated correlated-k model for the longwave. *Journal of Geophysical Research: Atmospheres*, **102 (D14)**, 16 663–16 682.

Moeng, C., J. Dudhia, J. Klemp, and P. Sullivan, 2007: Examining two-way grid nesting for large eddy simulation of the PBL using the WRF model. *Monthly weather review*, **135 (6)**, 2295–2311.

Moeng, C.-H., 1984: A large-eddy-simulation model for the study of planetary boundary-layer turbulence. *Journal of the Atmospheric Sciences*, **41 (13)**, 2052–2062.

Monin, A. S., and A. M. Obukhov, 1954: Basic laws of turbulent mixing in the surface layer of the atmosphere. *Contrib. Geophys. Inst. Acad. Sci. USSR*, **151 (163)**, e187.

Muñoz-Esparza, D., and B. Kosović, 2018: Generation of inflow turbulence in large-eddy simulations of nonneutral atmospheric boundary layers with the cell perturbation method. *Monthly Weather Review*, **146 (6)**, 1889–1909.

Muñoz-Esparza, D., B. Kosović, J. Mirocha, and J. van Beeck, 2014: Bridging the transition from mesoscale to microscale turbulence in numerical weather prediction models. *Boundary-Layer Meteorology*, **153 (3)**, 409–440.

Muñoz-Esparza, D., B. Kosović, J. Van Beeck, and J. Mirocha, 2015: A stochastic perturbation method to generate inflow turbulence in large-eddy simulation models: Application to neutrally stratified atmospheric boundary layers. *Physics of Fluids*, **27 (3)**, 035 102.

Muñoz-Esparza, D., J. K. Lundquist, J. A. Sauer, B. Kosović, and R. R. Linn, 2017: Coupled mesoscale-les modeling of a diurnal cycle during the cwex-13 field campaign: From weather to boundary-layer eddies. *Journal of Advances in Modeling Earth Systems*, **9 (3)**, 1572–1594.

Nakanishi, M., and H. Niino, 2006: An improved Mellor–Yamada level-3 model: Its numerical stability and application to a regional prediction of advection fog. *Boundary-Layer Meteorology*, **119 (2)**, 397–407.

Owens, R., and T. Hewson, 2018: Ecmwf forecast user guide. *Reading: ECMWF*, **10**, –.

Pineda, N., O. Jorba, J. Jorge, and J. Baldasano, 2004: Using NOAA AVHRR and SPOT VGT data to estimate surface parameters: application to a mesoscale meteorological model. *International Journal of Remote Sensing*, **25 (1)**, 129–143.

Pope, S. B., 2000: *Turbulent flows*. Cambridge University Press.

Poulos, G. S., 1996: The interaction of katabatic winds and mountain waves. Ph.D. thesis, Colorado State University, an optional note.

Prandtl, L., 1942: Führer durch die strömungslehre (essentials of fluid mechanics). *Vieweg und Sohn*.

Rai, R. K., L. K. Berg, B. Kosović, J. D. Mirocha, M. S. Pekour, and W. J. Shaw, 2017: Comparison of measured and numerically simulated turbulence statistics in a convective boundary layer over complex terrain. *Boundary-Layer Meteorology*, **163 (1)**, 69–89.

Schär, C., and D. R. Durran, 1997: Vortex formation and vortex shedding in continuously stratified flows past isolated topography. *Journal of the Atmospheric Sciences*, **54 (4)**, 534–554.

Schär, C., and R. B. Smith, 1993: Shallow-water flow past isolated topography. Part I: Vorticity production and wake formation. *Journal of the Atmospheric Sciences*, **50 (10)**, 1373–1400.

Schmidli, J., and Coauthors, 2011: Intercomparison of mesoscale model simulations of the daytime valley wind system. *Monthly Weather Review*, **139 (5)**, 1389–1409.

Scorer, R., 1949: Theory of waves in the lee of mountains. *Quarterly Journal of the Royal Meteorological Society*, **75 (323)**, 41–56.

Skamarock, W. C., J. B. Klemp, J. Dudhia, D. O. Gill, D. M. Barker, W. Wang, and J. G. Powers, 2008: A description of the advanced research wrf version 3. Tech. rep., NCAR.

Smith, C. M., and F. Porté-Agel, 2014: An intercomparison of subgrid models for large-eddy simulation of katabatic flows. *Quarterly Journal of the Royal Meteorological Society*, **140 (681)**, 1294–1303.

Smith, C. M., and E. D. Skyllingstad, 2005: Numerical simulation of katabatic flow with changing slope angle. *Monthly Weather Review*, **133 (11)**, 3065–3080.

Smolarkiewicz, P., and R. Rotunno, 1989: Low froude-number flow part 3-dimensional obstacles part 1: baroclinically generated lee vortices. *Journal of the Atmospheric Sciences*, **46 (8)**, 1154–1164, doi: 10.1175/1520-0469(1989)046<1154:LFNFPT>2.0.CO;2.

Stull, R. B., 1988: *An introduction to boundary layer meteorology*. Springer Science & Business Media.

Tabor, G. R., and M. Baba-Ahmadi, 2010: Inlet conditions for large eddy simulation: A review. *Computers & Fluids*, **39 (4)**, 553–567.

Taylor, D. M., F. K. Chow, M. Delkash, and P. T. Imhoff, 2018: Atmospheric modeling to assess wind dependence in tracer dilution method measurements of landfill methane emissions. *Waste Management*, **73**, 197–209.

Wagner, J., T. Gerz, N. Wildmann, and K. Gramitzky, 2019: Long-term simulation of the boundary layer flow over the double-ridge site during the perdigão 2017 field campaign. *Atmos. Chem. Phys.*, **19**, 1129–1146.

Warner, T. T., R. A. Peterson, and R. E. Treadon, 1997: A tutorial on lateral boundary conditions as a basic and potentially serious limitation to regional numerical weather prediction. *Bulletin of the American Meteorological Society*, **78 (11)**, 2599–2618.

Weckwerth, T. M., J. W. Wilson, and R. M. Wakimoto, 1996: Thermodynamic variability within the convective boundary layer due to horizontal convective rolls. *Monthly Weather Review*, **124 (5)**, 769–784.

Whiteman, C. D., S. W. Hoch, and G. S. Poulos, 2009: Evening temperature rises on valley floors and slopes: Their causes and their relationship to the thermally driven wind system. *Journal of Applied Meteorology and Climatology*, **48 (4)**, 776–788.

Wiersema, D., K. Lundquist, and F. Chow, 2018: Development of a multiscale modeling framework for urban simulations in the Weather Research and Forecasting model. Tech. rep., Lawrence Livermore National Lab.(LLNL), Livermore, CA (United States).

Wiersema, D. J., K. A. Lundquist, and F. K. Chow, 2020: Mesoscale to microscale simulations over complex terrain with the immersed boundary method in the weather research and forecasting model. *Monthly Weather Review*, **148 (2)**, 577–595.

Wise, A. S., J. M. T. Neher, R. S. Arthur, and F. K. Chow, 2020: Multi-scale modeling of a wind turbine wake over complex terrain in different atmospheric stability regimes. *19th Conference of Mountain Meteorology*, 8.2, https://ams.confex.com/ams/19Mountain/meetingapp.cgi/Session/54552.

Wood, N., 2000: Wind flow over complex terrain: a historical perspective and the prospect for large-eddy modelling. *Boundary-Layer Meteorology*, **96 (1-2)**, 11–32.

Wyngaard, J. C., 2004: Toward numerical modeling in the "Terra Incognita". *Journal of the Atmospheric Sciences*, **61 (14)**, 1816–1826.

Xie, B., J. C. Fung, A. Chan, and A. Lau, 2012: Evaluation of nonlocal and local planetary boundary layer schemes in the WRF model. *Journal of Geophysical Research: Atmospheres*, **117 (D12)**.

Zängl, G., 2005: Formation of extreme cold-air pools in elevated sinkholes: An idealized numerical process study. *Monthly Weather Review*, **133 (4)**, 925–941.

Zardi, D., and C. D. Whiteman, 2013: Diurnal mountain wind systems. *Mountain Weather Research and Forecasting: Recent Progress and Current Challenges*, F. K. Chow, S. F. De Wekker, and B. J. Snyder, Eds., Springer Netherlands, Dordrecht, 35–119, doi: 10.1007\/978\-94\-007\-4098\-3_2, URL https://doi.org/10.1007/978-94-007-4098-3_2.

Zhang, H., Z. Pu, and X. Zhang, 2013: Examination of errors in near-surface temperature and wind from WRF numerical simulations in regions of complex terrain. *Weather and Forecasting*, **28 (3)**, 893–914.

Zhong, S., and F. K. Chow, 2013: Meso- and fine-scale modeling over complex terrain: Parameterizations and applications. *Mountain Weather Research and Forecasting: Recent Progress and Current Challenges*, F. K. Chow, S. F. De Wekker, and B. J. Snyder, Eds., Springer Netherlands, Dordrecht, 591–653.

Zhou, B., J. S. Simon, and F. K. Chow, 2014: The convective boundary layer in the terra incognita. *Journal of the Atmospheric Sciences*, **71 (7)**, 2545–2563.

Appendix A

Surface Flux Boundary Conditions

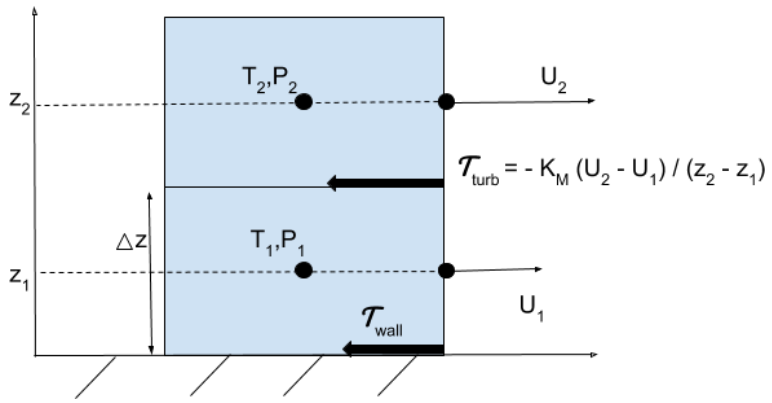

Figure A.1: The lowest two grid cells of an atmospheric model on a staggered grid. Labelled quantities are relevant to derivations in the text.

A.1 Drag Parameterizations

Surface boundary conditions in weather models

Typical numerical weather prediction (NWP) codes, including the Weather Reasearch and Forecasting (WRF) model, use some form of flux boundary condition at the Earth surface for nearly all prognostic variables: momentum, moisture, sensible heat, trace gases, and so on. The formulation of the evolution equations for these variable is strikingly similar regardless of whether a Reynold's averaging or a grid filtering, as in large-eddy simulation, approach is considered. In the following we will use nomenclature of the more familiar Reynold's averaging approach and provide the analogous verbage for LES in parenthetical remarks. Taking mean (filtered) zonal velocity, U, as our variable of interest, we turn to the Reynolds-averaged (spatially filtered) x-momentum equation:

$$\frac{\partial U}{\partial t} = -U_j \frac{\partial U}{\partial x_j} - \frac{1}{\rho}\frac{\partial P}{\partial x_1} - \frac{\partial \tau_{1j}}{\partial x_j} + fV + ... \tag{A.1}$$

The usual suspects appear in the above, from left to right: unsteadiness, mean (resolved) advection, mean (resolved) pressure forcing, Reynold's (subfilter) stresses normalized by density, Coriolis, and we could add more if other forces are present, e.g. electromagnetic forces in the ionosphere. In any case, we will ignore the other tendencies terms in (A.1) to focus on the surface boundary effects. The surface layer parameterizations will directly enter only one of the terms on the right hand side above. We segregate this term,

$$\frac{\partial U}{\partial t} = -\frac{\partial \tau_{13}}{\partial x_3} + \text{other tendency terms.} \tag{A.2}$$

For a computer to aid our solution of this equation, we must discretize the equation so that it can be approximately solved on a grid. The state-of-the-art NWP codes will use a staggered grid similar to that illustrated in figure A.1, above. As such, a discretized equation for the first U point is given by

$$\frac{U_1^{n+1} - U_1^n}{\Delta t} = -\frac{\tau_{turb} - \tau_{wall}}{\Delta z} + \text{other tendency terms} \tag{A.3}$$

$$U_1^{n+1} = U_1^n + \Delta t \left(\frac{\tau_{wall}}{\Delta z} + \text{all other tendency terms} \right), \tag{A.4}$$

where U_1^n is shorthand for mean (filtered) zonal velocity at the first grid cell above the ground at time step n. The 'all other tendency terms' are computed in the same way as in the bulk of the fluid, including the turbulent stress, τ_{turb}, acting between the first cell and the second. The term which represents the sink of fluid momentum due to the presence of the solid boundary, τ_{wall}, is yet to be specified. After closing all these term, we may use (A.4) to advance our solution to U forward in time.

The Bulk Drag Coefficient

To approximately solve the evolution of the state of the atmosphere via equations given in the previous section, the present problem has been narrowed to specifying τ_{wall}, stress at the model bottom. In other disciplines of fluid mechanics, it is common to specify the contribution to total drag from viscous forces known as skin drag, from dynamic pressure forces known as form drag, and from buoyant forces known as wave drag. Closures for wave drag can be important over complex terrain at coarse resolution. In NWP models, wave drag is handled by an orographic drag parameterization separate from the surface layer models which are the focus of this paper. In these formulations, skin drag and form drag are most often combined into a single quantity, bulk drag, which acts at the model bottom.

The simplest drag law parametrization was suggested by G.I. Taylor in 1916 (Stull 1988). Below, we give this formulation for total drag, $|\tau|_{wall}$, in terms of mean wind speed, $|U|$, and for the mean zonal wind and drag, U and τ_{wall}, as in the previous section:

$$|\tau|_{wall} = u_*^2 = C_D |U|_1^2 \tag{A.5}$$

$$\tau_{wall} = -C_D |U|_1 U_1 \tag{A.6}$$

In this way, the problem has been reframed; now we must define C_D to carry out the time advancement. While a constant drag coefficient can be fit to data for simple and/or idealized models, state-of-the-art codes mostly abandon this approach.

Instead, wall stress is diagnosed by assuming the first grid point either (i) exists in the log-layer for neutral stratification, or (ii) lies in a surface layer for which the deviations from a log-profile can be completely characterized by the Obukhov length scale. A drag coefficient

is then defined dynamically via (A.5), then applied to each component of velocity via (A.6) and an analogous expression for the mean (filtered) meridional velocity.

The assumptions (i) and (ii) form the basis of Monin–Obukhov similarity theory. As we will see in later sections, it is unlikely that these similarity relationships are sufficient over complex terrain where horizontal homogeneity is an inappropriate assumption. But first, let us review the current practice.

Log-law for the neutrally stratified boundary layer

Pursuing the unstratified case, assume the log-law and substitute our bulk drag parameterization from (A.5),

$$|U| = \frac{u_*}{\kappa} \ln\left(\frac{z}{z_0}\right) \tag{A.7}$$

$$= \frac{\sqrt{C_D}\,|U|}{\kappa} \ln\left(\frac{z}{z_0}\right) \tag{A.8}$$

where z_0 is a roughness length scale and $\kappa \approx 0.4$ is the Von Karman constant. In this case, we can solve for C_D algebraically as,

$$C_D = \left[\frac{1}{\kappa} \ln\left(\frac{z}{z_0}\right)\right]^{-2}. \tag{A.9}$$

Assuming the first grid point lies in the log-layer, from (A.6) we have

$$\tau_{wall} = -\left[\frac{1}{\kappa} \ln\left(\frac{z_1}{z_0}\right)\right]^{-2} |U|_1 U_1, \tag{A.10}$$

and, from (A.4),

$$U_1^{n+1} = U_1^n + \Delta t \left(\frac{-\left[\frac{1}{\kappa} \ln\left(\frac{z_1}{z_0}\right)\right]^{-2} |U|_1^n U_1^n}{\Delta z} + \text{all other tendency terms} \right). \tag{A.11}$$

In this way, we advance in time by assuming unstratified flows obey the log-law at the first grid cell above the ground.

Monin-Obukohv similarity theory for the stratified boundary layer

It is easiest to introduce Monin–Obukhov similarity theory (MOST) as a generalization of the log-law bulk drag parameterization presented in the previous section. To make clear this connection, compare the drag coefficient given by (A.9) to the expression below which comes from a Monin–Obukhov drag parameterization:

$$C_D = \left[\frac{1}{\kappa}\ln\left(\frac{z_1}{z_0}\right) + \Psi\left(\frac{z_1}{L}\right)\right]^{-2}, \tag{A.12}$$

where, (A.13)

$$\frac{z}{L} = -\frac{\kappa z g(\overline{w'\theta_v'})}{\overline{\theta_v}u_*^3} = -\frac{\kappa z g(\overline{w'\theta_v'})}{\overline{\theta_v}|\tau|_{wall}^{3/2}} \tag{A.14}$$

The parameter, L, is called the Obukhov length and Ψ is a so-called universal function or similarity function (Monin and Obukhov 1954). The universal function, Ψ, is fit empirically and subject only to the constraint that $\Psi\left(\frac{z_1}{L}\right) \to 0$ as $\frac{z_1}{L} \to 0$, i.e., under neutral stratification, MOST reduces to the log-law.

Note, the drag coefficient is defined in terms of τ_{wall}, the stress at the wall or, equivalently, by u_* from (A.5). In equation (A.12), however, our drag coefficient is given in terms of this stress, since L is a function of τ_{wall} or u_* as shown in (A.14). Iteration can provide solutions to equations like these which are defined implicitly.

Since iteration will be required at some level, these algorithms are rarely formulated in terms of a drag coefficient. Instead, we iterate for wall stress directly, in terms of u_*. Further, models often simultaneously iterate for $\overline{w'\theta_v'}$ which is found in the definition of Obukhov length and thus encounters an analogous implicit definition for the sensible heat flux at the surface.

To see how this works in practice, we turn to a more fundamental form for surface layer similarity. Indeed, (A.12) is merely algebraic manipulation of the following equation which is analogous to the log-law, (A.7), from the neutral case. That is,

$$|U|_1 = \frac{u_*}{\kappa}\left[\ln\left(\frac{z_1}{z_0}\right) + \Psi\left(\frac{z_1}{L}\right)\right], \tag{A.15}$$

is a generalization of the log-law for application in stratified flows. The justification for this functional form will be elaborated, and critiqued, in the following. For now, we examine a pseudo-algorithm, adapted from Basu et al. (2008), to solve for u_* and $\overline{w'\theta_v'}$ simultaneously:

Given: $|U|_1$, z_1, $\overline{\theta_1}$, $\Delta\Theta$, z_{0M}, z_{0H}
Initial Values for Ψ_M and Ψ_H are zero (neutral) or from previous time step

While not(convergence criteria) do,

$$u_* = \frac{\kappa |U|_1}{\ln\left(\frac{z_1}{z_{0M}}\right) + \Psi_M\left(\frac{z_1}{L}\right)}$$

$$\overline{w'\theta'_v} = \frac{-\kappa \Delta\Theta u_*}{\ln\left(\frac{z_1}{z_{0H}}\right) + \Psi_H\left(\frac{z_1}{L}\right)}$$

$$L = -\frac{\overline{\theta_v} u_*^3}{\kappa g(\overline{w'\theta'_v})} \tag{A.16}$$

$$\Psi_M = f\left(\frac{z_1}{L}\right)$$

$$\Psi_H = g\left(\Psi_M\right) = g \circ f\left(\frac{z_1}{L}\right) \tag{A.17}$$

$$\text{(convergence criteria).evaluate} \tag{A.18}$$

end.

The functions that relate sensible heat and momentum fluxes, are not defined in this text. We simply note the connection between scalar, e.g. heat, and momentum flux is a rich problem that could be the subject of numerous additional dissertations.

We do make explicit some common forms of the universal function, Ψ_M, from Stull's abbreviation of work by Businger et al. (1971) for the stable and neutral case and adapted from Benoit (1977) for the unstable case.

$$\Psi_M = \begin{cases} 4.7\frac{z}{L} & \frac{z}{L} > 0, \text{ stable} \\ 0 & \frac{z}{L} = 0, \text{ neutral} \\ \ln\left[\frac{\left(1+x_0^2\right)(1+x_0)^2}{(1+x^2)(1+x)^2}\right] + 2\left[\tan^{-1}(x) - \tan^{-1}(x_0)\right] & \frac{z}{L} < 0, \text{ unstable} \\ \qquad \text{with } x = \left(1 - 15\frac{z}{L}\right)^{1/4},\ x_0 = \left(1 - 15\frac{z_0}{L}\right)^{1/4} & \end{cases} \tag{A.19}$$

There is a wider class of Monin–Obukhov surface layer formulations that reduce to the log-law for neutral stratification, but are not easily represented by the Ψ functional forms above. These come from integrating non-dimensional shear, $\frac{\kappa z}{u_*}\frac{\partial |U|}{\partial z}$, which is assumed to be another universal function of the Obukhov length:

$$\frac{\kappa z}{u_*}\frac{\partial |U|}{\partial z} = \Phi\left(\frac{z}{L}\right) \tag{A.20}$$

Indeed, the results of (A.19) are obtained from direct integration of empirically fit functional forms of non-dimensional shear. Below, we provide the Φ functions corresponding to the Ψ

functions above, all of which come from Businger et al. (1971):

$$\Phi = \begin{cases} 1 + 4.7\frac{z}{L} & \frac{z}{L} > 0, \text{ stable} \\ 1 & \frac{z}{L} = 0, \text{ neutral} \\ \left(1 - 15\frac{z}{L}\right)^{-1/4} & \frac{z}{L} < 0, \text{ unstable.} \end{cases} \tag{A.21}$$

While the specific forms for non-dimensional shear provided here can be directly integrated, we can include a much larger class of functions which can only be integrated numerically. The pseudo-algorithm in this case is:

Given: $|U|_1$, z_1, $\overline{\theta_1}$, $\Delta\Theta$, z_{0M}, z_{0H}
Initial Values for Φ_M and Φ_H are one (neutral) or from previous time step

While not(convergence criteria) do,

$$\begin{aligned} u_* &= \frac{\kappa|U|_1}{\int_{z_{0M}}^{z_1} \frac{\Phi_M\left(\frac{z^*}{L}\right)}{z^*} dz^*} \\ \overline{w'\theta'_v} &= \frac{-\kappa\Delta\Theta u_*}{\int_{z_{0H}}^{z_1} \frac{\Phi_H\left(\frac{z^*}{L}\right)}{z^*} dz^*} \\ L &= -\frac{\overline{\theta_v} u_*^3}{\kappa g(\overline{w'\theta'_v})} \\ &\text{(convergence criteria).evaluate} \end{aligned} \tag{A.22}$$

end.

Finally, with a methodology for evaluating surface stress in stratified conditions and with explicit forms of the similarity functions, Ψ and Φ, the reader is finally equipped to implement state-of-the-art drag parameterizations in their own model. However, recalling modeling challenges faced in the body text chapters, it would be wise to more carefully examine the theoretical justification for the relevance of the Obukhov length, the subject of the next section.

A.2 New Forms for Complex Terrain

Buckingham Pi

A thorough presentation of the Buckingham Pi theorem can be found in numerous texts (Stull 1988). Here, we summarize the basic result:

Given k relevant physical variables in r dimensions, the phenomenon of interest is characterized by $k - r$ dimensionless groups formed from the physical variables.

In the context of surface momentum fluxes over flat, homogeneous terrain we have 7 relevant parameters:

$$U, u_*, z, z_0,$$
$$g, \overline{w'\theta'_v}, \overline{\theta_v}.$$

The last three parameters are related to buoyancy and only relevant in the presence of stratification. Taking all 7 of these parameters, we have 3 dimensions: length, time, and temperature. Thus, by Buckingham Pi, we require 4 dimensionless groups. Buckingham Pi theorem does not tell the researcher which dimensionless groups, of the many that could be formed, are the relevant groups. One must guess and experiment, iterating that process as needed. Luckily, much of this experimentation has been done.

We know now the 4 relevant dimensionless groups, or Pi-groups, are

$$\frac{U}{u_*}, \frac{z}{z_0}$$

$$\frac{\overline{w'\theta'_v}}{u_*\overline{\theta_v}}, \frac{zg}{u_*^2}$$

The last two Pi-groups are only relevant with stratification. Further the final term, non-dimensional gravity $= \frac{zg}{u_*^2}$, has not been varied independently of the other terms. This would require experimentation on another planet or some other way of changing the value of gravity. For the record, the author would very much like to go to space and test this theory if anybody from NASA ever reads this dissertation. In lieu of independent experimentation on non-dimensional gravity, it is reasonable to combine the stratification Pi-groups into a single, dimensionless quantity by multiplication:

$$\frac{\overline{w'\theta'_v}}{u_*\overline{\theta_v}} \times \frac{zg}{u_*^2} = \frac{z}{L}. \tag{A.23}$$

Using these terms, we can express the non-dimensional equation as

$$\frac{U}{u_*} = f\left(\frac{z}{z_0}, \frac{z}{L}\right) \tag{A.24}$$

Note, that the log-law, equation (A.7), and its generalization under stratification, equation (A.15), both fit this form.

Now, let us consider the implications of Buckingham Pi theorem for the case of shear by complex terrain. We will likely need more than the 7 parameters presented in the last section, because none of those parameters address horizontal heterogeneity. Scaling the governing equation for turbulent kinetic energy, TKE or k, provides one possible method for uncovering new scales relevant to wall stress.

Scaling TKE

An appropriate scaling of the TKE equation leads to the definitions of both the Obukhov length and non-dimensional shear. As the log-law is retained as a special case of M-O similarity theory, any surface layer model applicable over complex terrain should reduce to MOST over homogeneous terrain. Therefore, it is wise to retain the same dissipative scaling that leads to the log-law and MOST.

Begin with the TKE equation,

$$\frac{\partial k}{\partial t} = -U_j \frac{\partial k}{\partial x_j} + \delta_{ij} \frac{g_j}{\bar{\theta}_v} \overline{u_i' \theta_v'} - \overline{u_i' u_j'} \frac{\partial U_i}{\partial x_j} - \frac{\partial \overline{u_j' k}}{\partial x_j} - \frac{1}{\bar{\rho}} \frac{\partial \overline{u_j' p'}}{\partial x_j} - \epsilon, \tag{A.25}$$

where the terms, from left to right, are known as unsteadiness, mean (resolved) advection, buoyancy production/consumption, shear generation, turbulent transport, pressure correlation, and dissipation. We scale this equation with a dissipative scaling, $\frac{\kappa z}{u_*^3}$, for a dimensionless equation:

$$\frac{\kappa z}{u_*^3} \left[\frac{\partial k}{\partial t} = -U_j \frac{\partial k}{\partial x_j} + \delta_{ij} \frac{g_j}{\bar{\theta}_v} \overline{u_i' \theta_v'} - \overline{u_i' u_j'} \frac{\partial U_i}{\partial x_j} - \frac{\partial \overline{u_j' k}}{\partial x_j} - \frac{1}{\bar{\rho}} \frac{\partial \overline{u_j' p'}}{\partial x_j} - \epsilon \right]. \tag{A.26}$$

This scaling is chosen because, with a host of other assumptions, the TKE equation reduces to the log-law. These assumptions are:

$$\begin{aligned}
&\overline{W} = 0, \text{ neglect subsidence, thermals} \\
&\epsilon = \frac{u_*^3}{\kappa z}, \text{ dissipative scaling with distance to wall} \\
&\overline{u_j' k} \approx 0, \text{ triple moments assumed small} \\
&\frac{\partial [\,]}{\partial t} = 0, \text{ steady turbulence} \\
&\frac{\partial [\,]}{\partial x} = \frac{\partial [\,]}{\partial y} = 0, \text{ fully developed turbulence} \\
&\qquad\qquad \text{over homogeneous terrain} \\
&\overline{u_i' \theta_v'} = 0 \implies \frac{z}{L} = 0, \text{ neutral stratification}
\end{aligned} \tag{A.27}$$

Aligning our x_1 coordinates with mean wind, the above assumptions leads to

$$0 = 0 + 0 + \frac{\kappa z}{u_*} \frac{\partial U}{\partial z} + 0 - 1 \tag{A.28}$$

such that the log-law can be obtained from directly integrating the above.

The Monin–Obukhov assumptions are slightly less strict:

$$\begin{aligned}
&\overline{W} = 0, \text{ neglect subsidence, thermals} \\
&\epsilon = \frac{u_*^3}{\kappa z} f\left(\frac{z}{L}\right), \text{ dissipative scaling with z, stratification} \\
&\overline{u_j' k} \approx 0, \text{ triple moments assumed small} \\
&\frac{\partial [\,]}{\partial t} = 0, \text{ steady turbulence} \\
&\frac{\partial [\,]}{\partial x} = \frac{\partial [\,]}{\partial y} = 0, \text{ fully developed turbulence} \\
&\qquad\qquad \text{over homogeneous terrain}
\end{aligned} \tag{A.29}$$

Aligning $x_3 = z$ antiparallel to gravity, these assumptions simplify the TKE equation to

$$0 = 0 + \frac{z}{L} + \frac{\kappa z}{u_*}\frac{\partial U}{\partial z} + 0 - f\left(\frac{z}{L}\right). \tag{A.30}$$

Or, rearranging by gathering terms that include $\frac{z}{L}$ into a single function,

$$\frac{\kappa z}{u_*}\frac{\partial U}{\partial z} = \Phi\left(\frac{z}{L}\right) \tag{A.31}$$

which is the same form as presented in (A.20). By making less restrictive assumptions and following the procedure outlined above, one may formulate a more general approach.

As we would expect, many of the terms in the TKE equation (A.25) involve k itself. Though Monin–Obukhov similarity does not claim k=0, all these terms are neglected in the non-dimensional shear formulation of MOST because of other assumptions. Specifically, the steady turbulence assumption and neglect of both mean and turbulent transport allow for a k-less function of dimensionless shear. Over complex terrain, some of these terms ought not to be neglected. Instead, this works suggests a canopy TKE model could be employed to allow for the use of a new Pi-group, non-dimensional canopy TKE.

Returning to the motivating example of drainage flows, the slope of terrain is also missing. Taken in radians, incline is already dimensionless and does not need to be normalized to form a Pi-group. Additional Pi-groups could also be added, a length scale related to the heterogeneity of land cover, $\mathrm{L_{LU}}$, can be defined in terms of average correlation distances of land type. That is, $\mathrm{L_{LU}}$ is equal to the average distance that a point on the ground is surrounded by land use of the same type. Another length scale comes from taking the frontal area of the vegetation relative to the volume of your grid cell, $\mathrm{L_{veg}}$, an idea adopted from turbulence modeling in aquatic vegetation. The suggested functional form becomes:

$$\frac{\kappa z}{u_*}\frac{\partial U}{\partial z} = \mathcal{X}\left(\frac{z}{L}, \frac{k_{\mathrm{canopy}}}{L}, \phi, \frac{z}{L_{\mathrm{LU}}}, \frac{z}{L_{\mathrm{veg}}}\right) \tag{A.32}$$

As with Ψ and Φ, the function $\mathcal{X}$ will be empirically fit and, without further experimentation, theoretical work must leave it at that.

The basic problem for diagnosing surface flux of momentum has been reviewed with special attention to the assumptions that limit current implementations to cases of homogeneous terrain. Two complimentary techniques for approaching the problem of complex terrain have also been reviewed, Buckingham Pi theorem and scaling the TKE equation. While we can do little to bring the issue to a close without experimentation, theoretical groundwork has been laid in the hopes of aiding future work.